SISSA
Scuola
Internazionale
Superiore di
Studi Avanzati

Physics Area - PhD course in
Statistical Physics

CONFINEMENT, INTEGRABILITY, AND ENTANGLEMENT IN QUENCH DYNAMICS

Candidate:
GIANLUCA
LAGNESE

Advisor:
PASQUALE CALABRESE

Academic Year 2021-22

Contents

Chapter 1

List of Publications

This thesis is based on the following publications:

[1] G. Lagnese, F. M. Surace, M. Kormos and P. Calabrese, *Confinement in the spectrum of a Heisenberg–Ising spin ladder* J. Stat. Mech. 093106 (2020),
Chapter 4.

[3] G. Lagnese, F. M. Surace, M. Kormos and P. Calabrese, *Quenches and confinement in a Heisenberg–Ising spin ladder* J. Stat. Mech. 093106 (2022),
Chapter 4.

[2] G. Lagnese, F. M. Surace, M. Kormos and P. Calabrese, *False vacuum decay in quantum spin chains*, Phys. Rev. B **104**, L201106 (2021),
Chapter 5.

[4] G. Lagnese, P. Calabrese and L. Piroli, *Entanglement dynamics of thermofield double states in integrable models*, J. Phys. A: Math. Theor *to appear* (2022) ,
Chapter 7.

[5] B. Bertini, K. Klobas, V. Alba, G. Lagnese, P. Calabrese, *Growth of Rényi Entropies in Interacting Integrable Models and the Breakdown of the Quasiparticle Picture*, arXiv:2203.17264,
Chapter 8.

Chapter 2

Introduction

Collective phenomena and many-body dynamics are ubiquitous in nature: they are observed and studied in many fields of research such as economics, social sciences, biology, as well as several branches of physics. In this perspective, universality is a key concept and a milestone of modern physics: in real systems close to criticality, many microscopic details become irrelevant, while only a few crucial relevant features such as symmetries, dimensionality, and the range of interactions govern the macroscopic (collective) behavior, as prescribed by renormalization group theory. In light of the aforementioned considerations, much of the effort in the framework of statistical physics has been made in the direction of describing continuous phase transitions of condensed matter systems at equilibrium. Thanks to the idea of universality, it is possible to interpret experimental observations and describe the low-energy/long-range behaviour of those real systems in terms of effective models with few parameters, both in quantum and classical settings. Equilibrium Statistical Physics has now been a successful and mathematically well-developed theory for long time. However, much less is known away from equilibrium.

The physics of strongly correlated one-dimensional quantum systems has been attracting a lot of attention for diverse reasons. On the one hand, due to the emphasised effect of strong correlation and interactions, low-dimensional systems are of particular interest because fluctuation effects are relevant, therefore the mean field description fails. On the other hand, a rich toolbox of analytical methods has been developed and exact solutions exist for a subset of microscopic models, including both systems in the continuum such as the Gaudin-Yang model and the Lieb-Liniger gas and lattice models such as the spin 1/2 XXZ and the Fermi-Hubbard chain. In addition, a revolution of ultra-cold atoms based experimental setups [6] allowed for fine tuning of the interaction strength through the Feshbach resonances as well as for the possibility of changing the dimensionality with optical potentials. Such experimental breakthrough changed completely the interplay between theory and experiments as it opened the possibility to experimentally realize and simulate the physics of such models. Furthermore, the fact that such cold atom systems are sufficiently weakly coupled to their environments allows for the observation of essentially unitary non-equilibrium time evolution on long time

scales. Given all the aforementioned motivations and the availability of experimental controllable systems whose properties can be accurately described by simple models, one-dimensional quantum systems became an extraordinary playground where to investigate quantum many-body physics, as they provide an unprecedented opportunity to explore several new frontiers of condensed matter physics including the non-equilibrium dynamics in closed interacting quantum systems. The importance of such developments is two-fold. On the one hand, there are fundamental problems to be addressed and direct simulations of simple models may help to solve them; they are related to the following questions: Does the system reach a stationary state? Under which conditions? Can we provide quantitative predictions for the time scales associated to relaxation? What is the nature of the emerging stationary states? Is there an emerging universality in the out-of-equilibrium time evolution? Many progresses have been made toward an answer to such questions. The interested reader may consult the some of the existing reviews on the subject [7, 8, 9, 10, 11]. On the other hand, establishing a general framewrok to understand and predict non-equilibrium physics is crucial for the developing of future quantum technologies: in order to perform quantum computation, real time manipulations of interacting quantum systems is going to be required.

The research field of the non-equilibrium dynamics of one-dimensional many-body quantum systems now covers a large portion of the statistical physics literature of the last twenty years. Through the course of the present chapter a minimal set of tools required to properly contextualize the material collected in the manuscript will be briefly summarized. Sec. 2.1 introduces the quantum quench, the protocol used in this work to bring the systems of interest away from equilibrium. In Sec. 2.2 we discuss about the entanglement entropy, a key quantity when assessing non-equilibrium evolution of isolated quantum systems, and we sketch the main features of its quench dynamics. Sec. 2.3 reports a theoretical setting thanks to which, under proper assumptions, many aspect of the entanglement dynamics are understood. Finally in Sec. 2.4 the organization of the thesis is presented.

2.1 Quantum quenches

There are many suitable ways that could be employed in order to drive a system out of equilibrium: it is possible to force energy or particles through an external reservoir or apply a driving field. Another one is represented by the so called ramps [12, 13, 14], related to the Kibble-Zurek mechanism. Others are inhomogeneous settings [15]. Through the present thesis we are going to adopt a simple but fundamental approach, which is now considered the archetypal protocol to drive a system out of equilibrium: the *quantum quench* [16, 17]. The protocol is usually configured as follows: at time $t = 0$ an isolated system is prepared in a pure state $|\psi_0\rangle$. Usually, it is the ground state of a many-body Hamiltonian H_0. A Hamiltonian parameter (i.e. magnetic field or interaction strength) is then suddenly changed and the system is evolved for $t > 0$ as $|\psi\rangle = e^{-iHt}|\psi_0\rangle$ with a Hamiltonian H that does not commute with H_0. In the following we are going to be focused on the case where the pre-quench and post-

quench Hamiltonians are translationally invariant, which is called *global quench*. The Hamiltonians are required to be short range. Due to the experimental feasibility of the protocol, it turns out to be of fundamental relevance. Since H and H_0 do not commute the pre-quench state $|\psi_0\rangle$ acquires a non-vanishing overlap with an exponentially large number of eigenstates of the post-quench Hamiltonian and a spatially uniform finite energy density. In generic systems, during the subsequent time evolution the expectation values of observables $\mathcal{O}$ relaxes to stationary values described by thermal ensembles as

$$\langle \mathcal{O} \rangle = Tr \left[\mathcal{O} e^{-\beta H} \right],$$

where the parameter β is fixed through the expectation value of the energy on the initial state. Eventually, other parameter are introduced if there are more conserved quantities such as particle number. The occurrence of such statistical ensembles in isolated quantum systems is fundamentally different from the one found in Statistical Physics textbooks. By definition of unitary evolution, a pure state stays pure. Conversely, the emergence of thermal ensembles is usually understood in terms of a coupling between the system and an external reservoir. To solve the apparent paradox the role of locality is crucial: if we focus on a local, sufficiently small, portion of an isolated extended system the latter can serve as its own thermal bath, and local relaxation should be possible. The information about the initial state spreads along the system and it is not anymore accessible through local measurements. The reader may find a comprehensive discussion on *quantum thermalization* in [11]. Classes of non-thermalizing systems, deviating from the aforementioned behavior, exist. These are *many body localized* systems [18] , *quantum scarred* systems [19] and systems exhibiting confinement [20, 21, 22]. However, only the last class is of interest for the present manuscript. In the following we focus on yet another scenario: the one represented by *integrable theories*. It should here be stressed that even if we will be concerned by models where integrability has been broken, still we will consider originally integrable models where a "perturbative" field has been introduced driving them away from integrability. Thus, the integrable settings represent the "null model" we assume in order to address our investigations. In integrable models the dynamics is constrained by an infinite set of quasi-local conserved quantities and observables do not relax to thermal ensembles. Nonetheless, local proprieties still exhibit relaxation to stationary values predicted through the Generalized Gibbs Ensemble [23]. In this case the quench dynamics may be understood in term of stable quasiparticle excitations [16]: the initial state $|\psi_0\rangle$, which is higher in energy for the post-quench Hamiltonian H, acts as a source of quasiparticles that travel ballistically at a certain speed. Those emitted within a certain correlation length typical of the initial state (the ground state of H_0) are responsible of spreading quantum correlation throughout the system. A typical *light cone* effect is detectable in the two-point correlation functions: if v is a maximal speed of propagation, all connected correlators at time t vanish at a distance greater than $2vt$. Moreover, coherent quasiparticles arriving at the same point from different sources cause exponential relaxation of local quantities such as the local order parameter toward the ground state expectation value. Finally, the light cone effects are detected through the linear growth of the entanglement: Another quantity that

is sensitive to quantum correlations and proved to encode distinctive nonequilibrium features.

2.2 Quantum entanglement

The true nature of quantum entanglement, or the exhibition of nonclassical correlations between separate systems, is elusive and susceptible to intense debate. Due to its nonlocal connotations, it has been considered among the trademarks of quantum mechanics from the early stages of the theory. Studying and characterizing the entanglement became soon an interdisciplinary problem and brought together subjects such as quantum mechanics, communication and information theory. It stimulated the emergence of new research fields like quantum information, quantum computation and cryptography.

The attempt to quantify the degree of entanglement in systems with many degrees of freedom has been at the center of quantum information science and statistical physics. We previously mentioned how relaxation in the out-of-equilibrium dynamics is deeply intertwined with the problem of the scrambling of local information. Entanglement measures, quantifying such information, possibly clarify how statistical ensembles emerge from the unitary time evolution of pure states in isolated systems: it is widely accepted that the stationary value of the entanglement of a large subsystem embedded in an infinite system may be interpreted as its thermodynamic entropy [24]. Among all the proposed possible good measures of entanglement [25, 26, 27] a popular one is the *entanglement entropy*. It is defined as follows. We assume our system is prepared in a pure state $|\psi\rangle$ and we define the reduced density matrix of a subsystem A tracing away the degrees of freedom of its complementary $\bar{A}$ as $\rho_A = Tr_{\bar{A}}\ \rho$ (where ρ is the density matrix of the whole system $|\psi\rangle\langle\psi|$). The entanglement entropy of the subsystem A is then the Von Neumann entropy of its reduced density matrix ρ_A

$$S(\rho_A) = -Tr_A\ \rho_A \log \rho_A\ . \tag{2.1}$$

The characterization of its time evolution after a quench evoked an intense research activity. Because of the functional form of Eq. 2.1 a straightforward connection with the information theory is established as it of the same form as the Shannon entropy developed for quantifying the information loss in transmitting a given message in a communication channel [28]. Other conceptually valuable and experimentally relevant measures of entanglement are the so called Rényi entropies, defined as

$$S_\alpha(\rho_A) = \frac{1}{1-\alpha} \log Tr_A\, [\rho_A^\alpha]\, . \tag{2.2}$$

These are a family of seemingly minor variations of the entanglement entropy, which have been shown to provide highly nontrivial universal information about the system [29], for instance on its topological properties [30]. Arguably the most significant point of interest of Rényi entropies, of integer order $\alpha \geq 2$, is that they are accessible in present-day experiments [31, 32, 33, 34, 36, 37, 38, 39, 40]. The entanglement entropy in Eq. 2.1 is recovered once the limit $\alpha \to 1$ has been taken. As it was briefly introduced in Sec. 2.1

after a quantum quench in a clean quantum many-body system they generically display a universal linear growth in time followed by saturation. In particular, the slope of the growth carries crucial information on the nature of the system's dynamics, and its characterisation is a key objective of current research.

2.2.1 Entanglement quench dynamics

The linear growth of entanglement is arguably the most distinctive and pervasive phenomenon observed in the context of quantum many-body dynamics: whenever a clean, locally interacting many-body system is prepared in a low-entangled state and then let to evolve, the entanglement between a compact region and its complement grows linearly in time. The ubiquity of this phenomenon suggests that a universal underlying mechanism is hidden behind the scenes. An astonishing outcome of recent research, however, suggests that this is not the case. Two distinct mechanisms for entanglement growth have been identified depending on the nature of the dynamics. The first account of linear growth of entanglement has been given in the context of (1+1)-dimensional conformal field theory (CFT) [41], where it was explained assuming that the entanglement is "spread" throughout the system by pairs of correlated quasiparticles produced by the quench [41]. It was later realized that the quasiparticle picture holds beyond quenches in CFT, and correctly describes the entanglement dynamics in one-dimensional (1D) systems with stable quasiparticle excitations [42]. This was first shown for non-interacting spin-chains through a rigorous microscopic derivation [43]. More recently, it has been extended to *interacting* integrable models [44, 45] (see also [46, 47, 48, 49, 50, 51, 52] for generalizations), inhomogeneous settings [53, 54, 55, 56] and open quantum systems [57, 58, 59, 60].

Contrary to the non-interacting case, the general validity of the quasiparticle picture has not yet been rigorously proven. Still, a significant amount of numerical evidence corroborating it has been collected in prototypical examples, including XXZ Heisenberg models [44, 45] and $SU(3)$-invariant spin chains displaying multiple quasiparticle species [61]. In addition, it has been established analytically in certain quantum cellular automata mimicking interacting quasiparticle dynamics [62, 63, 64]. For the sake of completeness, it must be mentioned how a second account for the linear growth of the entanglement was later developed. Indeed, an unexpected ballistic growth has been observed in systems with no quasiparticles, for instance holographic conformal field theories [65, 66], generic interacting systems [67, 68], and chaotic quantum circuits [69, 70, 71, 72]. The explanation was finally found through a "minimal membrane" picture [73, 74]. In essence, the idea is that in chaotic systems the entanglement between two complementary regions is measured by the tension of the minimal space-time surface that separates the two. Even though both quasiparticle and minimal-membrane pictures explain the linear growth of entanglement, they predict qualitatively different phenomenology when considering more complicated partitions of the system [66, 73, 46] or for finite sizes [73, 70].Given the difficulty to compute the real-time dynamics in interacting many-body systems, both the pictures represent remarkable results. However, in the course of the present manuscript we will be concerned on the first one (the reader

may find a thoroughly description of the minimal membrane picture in [74]).

2.3 The quasiparticle picture

We remind the reader the quench setting introduced in Sec. 2.1: the system is initialized in a pure state $|\Psi\rangle$, for instance the ground-state of a local Hamiltonian H_0, and left to evolve under a post-quench local Hamiltonian H (which is assumed to be translation-invariant). The quasiparticle picture provides a very simple interpretation (and quantitative description) of the post-quench entanglement dynamics, as we briefly explain now (see the reviews [75, 76] for a comprehensive treatment).

As a starting point, one postulates that the homogeneous quench produces everywhere an extensive number of uncorrelated pairs of entangled quasiparticles with opposite momenta. After the quench, the quasiparticles spread through the system, and cause distant regions to be entangled. At a given time t, the entanglement between two regions, A and B, is proportional to the number of pairs with one quasiparticle in A and the other in B. In CFT, the quasiparticles all propagate with the same velocity v, leading to the very simple equation

$$S_\ell(t) = 4vts\Theta(\ell - 2vt) + \ell s\Theta(2vt - \ell)\,, \tag{2.3}$$

where Θ is the Heaviside theta function and ℓ the subsystem size. Here s is the entanglement-entropy density carried by each pair of quasiparticles. Eq. (2.3) has been derived assuming that the infinite-system size limit $N \to \infty$ is taken first.

Recently, this picture has been generalized to the case of interacting integrable systems [44, 45]. As a defining feature, integrable models are characterized by the fact that the entire spectrum of their Hamiltonian can be described in terms of *stable* quasiparticles. In analogy with the non-interacting case, they can be parametrized by quasi-momenta, or *rapidities* $\{\lambda_j\}_j$, and display a non-trivial dispersion relation. The latter has to be taken into account within the quasiparticle picture, implying that distinct quasiparticles propagate with different velocities. This leads to a simple modification of Eq. (2.3), where one sums over the contributions coming from quasiparticles with different rapidities λ, namely [44]

$$S_\ell(t) = \sum_n \left[2t \int_{2|v_n|t<\ell} \mathrm{d}\lambda |v_n(\lambda)| s_n(\lambda) + \ell \int_{2|v_n|t>\ell} \mathrm{d}\lambda s_n(\lambda) \right] . \tag{2.4}$$

Here, $v(\lambda)$ and $s(\lambda)$ denote the velocity and density of entanglement entropy of the quasiparticles with rapidity λ, respectively. We also introduced an additional index n, which distinguishes between possible different types of quasiparticles or bound states thereof.

It was argued in Ref. [44] that $v_n(\lambda)$ and $s_n(\lambda)$ can be related to the thermodynamic properties of the stationary state emerging at large times after the quench, as described by the Generalized Gibbs Ensemble (GGE) [77, 23]. In particular, $v_n(\lambda)$ was identified with the velocity of the elementary excitations, and $s_n(\lambda)$ with the corresponding

thermodynamic, or Yang-Yang, entropy [78]. As a consequence, $v_n(\lambda)$ and $s_n(\lambda)$ can be computed exactly (at least for simple initial states), and (2.4) gives us a fully quantitative prediction with no free parameter to be fixed [44].

It should be stressed how an important assumption underlying Eq. (2.4) is that the quench only produces pairs of quasiparticles. At the microscopic level, this can be justified for a class of low-entangled *integrable* initial states [79, 80] (see also [81, 82] for related discussions). However, in more general cases it is possible that the quench also produces higher n-tuples of correlated quasiparticles. An explicit example in a non-interacting model is reported in Ref. [83, 84, 85] , where the authors found fine-tuned families of initial states for which the quench does not produce pairs but only higher n-tuples of quasiparticles. In this case, the entanglement dynamics is still captured by a semiclassical picture, but Eq. (2.4) has to be modified [83].

2.4 Organization of the thesis

In the present Chapter 2 the general framework in which the work here collected is embedded has been introduced. We conclude with an outline of the thesis. The text is divided into two parts:

Part. I concerns the out-of-equilibrium dynamics of low-dimensional systems with confinement. More precisely, in Chapter 4 the modifications, both in the spectrum and real-time quench dynamics, resulting from the presence of confinement in a spin ladder are investigated. While in Chapter 5 the possible occurrence of the phenomenon of false vacuum decay in spin models is investigated.

Part. II focuses on the quench dynamics of quantum entanglement in integrable spin chains. More in detail, in Chapter 7 it is showed how the quasiparticle picture introduced in Sec. 2.3 can be extended to characterize the non-equilibrium evolution of the entanglement entropy in a different class of states: the Thermofield Double States (TFD). In Chapter 8 an alternative methodology, allowing for predictions of the real-time evolution of the Rényi entropies in integrable models, is developed.

Part I

Confined dynamics in quantum spin chains

Chapter 3

Overview

Confinement of elementary particles is renowned as a fundamental mechanism for our understanding of fundamental interactions of nature. The prototypical example of such a phenomenon is quark confinement in quantum chromodynamics (QCD) [86] which is a ruling principle of strong interactions: quarks cannot be isolated at low-energy and they are only found in composite particles called hadrons such as baryons and mesons. Indeed, the mass of ordinary matter is in an overwhelming majority in the binding energy of protons and neutrons rather than in the masses of truly elementary particles such as quarks and electrons.

The idea behind the confinement of quarks in the high energy physics framework lies in the fact that an effective linear potential between the quarks arises from the gauge degrees of freedom: the large distance behavior of strong interaction mediated by the gluons is described as a potential linearly increasing with the particle distance $V(r) \approx \sigma r$ (where σ is known as *string tension*); in contrast, when two particles with opposite electrical charges are interacting, the Coulomb potential $V(r) \approx \frac{1}{r}$ does not diverge for large inter-particle distance. While in the Coulomb case it is possible to bring the inter-particle distance to infinite, the attempt to separate two color charges ends in the creation of another couple quark-antiquark (a process known as *string breaking*). Many aspects of confinement in relevant gauge theories in high-energy physics still are poorly understood and subject to intense investigations (the interested reader may find a detailed review in [87]). The lack of analytical techniques, due to the intrinsic non-perturbative nature of confinement, and the difficulty to perform numerical simulations of strong interactions on classical devices, challenge our ability to understand confinement in the relevant gauge theories (like QCD).

Recently, the possibility of using tools from quantum technologies for studying problems of strongly coupled quantum field theories has attracted a lot of interest [88, 89, 90, 91]. On the one hand, tensor-network approaches are promising candidates for studying non-equilibrium properties that cannot be accessed with traditional Monte Carlo simulations. These approaches have been successfully applied to $1+1$ and $2+1$ dimensional lattice gauge theories [92, 93, 94, 95, 96, 97, 98, 99] but they suffer from limitations with dimensionality. Therefore, there has been an increasing interest in the

toolbox of quantum simulators [100, 101, 102, 103, 104, 105, 106]. The hope is that controllable quantum systems in table-top experiments will help us understand difficult problems in quantum field theory, including, for example, confinement of the elementary excitations. In this context, one-dimensional quantum spin models represent the ideal framework for benchmarking quantum simulators: they can host particle confinement [107, 108], a property that can be observed in the non-equilibrium dynamics after a quantum quench [22, 109, 110]; it has also been suggested that their real-time evolution can reveal interesting phenomena including collisions of particles and bubble nucleation [111, 112, 113, 114, 115, 116]. Indeed, as we shall further discuss in the following, a remarkable discovery is that a similar phenomenology is displayed in the ordered phase of several condensed matter systems. Here the charged particles/anti-particles are domain walls toggling between degenerate ground states and an effective long-range potential emerges from the local interaction as a consequence of a symmetry-breaking mechanism: one of the two ground states acquires a finite energy density with respect to the other. Thus, pairs of domain wall states possess an energy proportional to the number of frustrated degrees of freedom between them.

3.1 Confinement in condensed matter physics

As theoretically proposed in the late seventies [107, 108] and directly verified in the last decade in a number of experiments with inelastic neutron scattering or other spectroscopic probes [117, 118, 119, 120, 121, 122, 123], confinement of excitations is a relevant phenomenon also in condensed matter physics. Following the pioneering work by McCoy and Wu [107], confinement has then been found and investigated with various analytical and numerical methods in thermal equilibrium in several quantum one-dimensional models [124, 125, 126, 127, 128, 129, 130, 131, 132, 1, 133, 134].

To date, confinement has been found and studied in great detail in many one-dimensional and quasi-one-dimensional magnetic insulators, with Ising-like [107, 108, 126, 128, 129] or Heisenberg-like [135, 136, 137, 138, 139, 140, 141, 142, 143, 144] interactions. Remarkable was the very recent experimental observation of the peculiar eight-particles E8-symmetric [145, 146] structure, predicted in [147], of the spectrum of the quantum transverse Ising chain close to the quantum critical point with a perturbative longitudinal field. Results achieved through neutron scattering and THz spectroscopy experiments on $CoNb_2O_6$ and $BaCo_2V_2O_8$. In all these cases, the spin-1/2 excitations (kinks or spinons) not only form bound states with integer spin, as a consequence of an (even weak) attractive interaction, but they cannot be observed as free particles at low energy, exactly like quarks in high energy physics. In very recent times, it has been proposed that many quantitative aspects of confinement (such as the masses of the bound states) can be accessed very effectively following the non-equilibrium real time dynamics [148, 22], a protocol that is routinely exploited in ultracold atoms and trapped ions experiments. This observation started an intensive theoretical activity on the subject [149, 150, 109, 151, 152, 153, 154, 155, 156, 157, 115, 111, 112, 158, 159, 2, 160] that lead to direct experimental implementation of a quantum simulator with trapped ions [110],

as well as several new theoretical and experimental ideas to understand lattice gauge theories in real time [148, 161, 162, 163, 103, 104]. Also, it was very recently observed on a IBM quantum computer [164] simulating a TFIM with external longitudinal field (the same model employed in [22]).

The time evolution after a quantum quench is typically characterised by lightcone spreading of correlators [16, 17] and by a linear growth of entanglement in time [41]. Remarkably, confinement of elementary excitations fundamentally alters this picture: the light cone spreading and the growth of entanglement are highly suppressed [22]. Furthermore, while typically the order parameter decays exponentially [16], in a confining scenario it oscillates with frequencies related to the masses of the mesons [22, 115]. Recent works showed that confinement may lead to the absence of thermalisation [152, 157], to the emergence of rare non-thermal states (*scars*) in the many-body spectrum [149, 150], and to fracton dynamics [160] as well as to anomalously slow dynamics [153, 154]. All these works addressed the dynamics of spin chains.

3.1.1 Quantum Transverse Field Ising chain

Before we embark on the analysis of more complicated models, the main features of confinement in condensed matter systems are reviewed through the Ising model with transverse and longitudinal fields in his ferromagnetic phase. McCoy and Wu studied this problem for the first time in the classical two-dimensional Ising field theory [107]: they showed how, in presence of an external symmetry breaking field, the two-point function develops a sequence of imaginary poles in momentum space; those poles correspond to the masses of the confined bound states. Now we focus on the quantum Ising chain, the Hamiltonian of the model reads

$$H = -\sum_{j=-\infty}^{\infty} \left[J\sigma_j^z \sigma_{j+1}^z + h_x \sigma_j^x + h_z \sigma_j^z \right] , \tag{3.1}$$

where σ_j^α are the Pauli matrices acting on site j. Here is the external longitudinal field h_z that triggers the symmetry breaking mechanism, but first we select $h_z = 0$. In this case the model possess a $\mathcal{Z}_2$ symmetry associated with the global flipping of all the spins. The model is exactly solved through a Jordan-Wigner mapping to free fermions. By tuning $J > 0$ we select a ferromagnetic nearest-neighbour interaction. When the transverse field is below the critical value $|h_x| < J$ we are in the ordered ferromagnetic phase and the Hamiltonian in eq. 3.1 has two degenerate ground states $|\psi_+\rangle$ and $|\psi_-\rangle$ identified through the non-vanishing expectation value of the local magnetization $\langle\psi_\pm| \sigma_j^z |\psi_\pm\rangle = \pm\sigma$. The fundamental excitations are freely propagating topologically charged domain walls called kinks interpolating between the two ground states. When an even small longitudinal field h_z is introduced, the original $\mathcal{Z}_2$ symmetry is broken and the degeneracy between the two ground states is lifted: the one with $\langle\sigma_j^z\rangle$ aligned to h_z becomes the new ground state while the other acquires a macroscopic energy difference with the first one; two-kinks configurations pay an energy cost proportional to the extension of the anti-aligned domain between them. Thus, similarly to quarks in QCD, kinks are not anymore allowed

to propagate freely and they get confined into *mesons*, which are neutrally charged particles with respect to the $\mathcal{Z}_2$ symmetry. As a consequence of the V-shaped confining potential, the mass of each meson is embedded in the binding energy of the *string* between the kinks; see fig 3.2 for a pictorial representation.

It should be now introduced how relevant information about the confined physics of the model is unraveled by following the non-equilibrium real-time evolution of suitable observables. There are three main concept we shall here illustrate:

- Suppression of the light cone spreading of correlators.
- Suppression of entanglement growth.
- Masses of the bound states are accessible through the so called *quench spectroscopy*

In Ref. [22] the quench protocol is applied preparing the system at $t = 0$ in the ground state of Eq. 3.1 for certain values of the parameters $h_x \neq 0$ and $h_z = 0$, then those parameters are suddenly changed. In [22] the role of h_x and h_z are exchanged with respect to the convetion adoped for Eq. 3.1. The ground state of the model is known to be low-entangled and the quasiparticle picture applies: after the abrupt change of the parameters pairs of kinks of opposite momenta are created and they propagate according to their characteristic speed. This is visible in the two-point connected correlations $\langle \sigma^z_1, \sigma^z_{1+\ell} \rangle_c$ showed in Fig. 3.1 (a), $h_z = 0$ case. In the same figure the effect of the light cone suppression is detected, even for a small longitudinal field.

An intuitive picture of what we are observing is easily obtained in the semi-classical limit $h_x \to 0$ and illustrated in Fig 5.1. The Hamiltonian is diagonal in the basis of classical spin configurations: $|\psi_+\rangle$ and $|\psi_-\rangle$ appear as $|\ldots\uparrow\uparrow\uparrow\uparrow\ldots\rangle$ and $|\ldots\downarrow\downarrow\downarrow\downarrow\ldots\rangle$ while kinks are $|\ldots\uparrow\uparrow\uparrow\downarrow\downarrow\downarrow\downarrow\ldots\rangle$. Pairs of kinks produced after the quench propagate in opposite directions until the confining potential halts their motion and pulls them back, leading to oscillatory motion. Another relevant effect is found in the long-lived oscillations of the time evolution of local observables: a representation is showed Fig 3.1 (b) for the expectation value of the local magnetization $\langle \sigma^x \rangle$, which is known to exponentially decay to zero when $h_z = 0$ [165]. The masses of the mesons are detected in the power spectrum of such local observables, a technique now dubbed *quench spectroscopy*. Finally, there is one more observable that is very sensitive to modification in the properties of the spectrum of the model: the entanglement entropy. In Fig 3.1 (c) the time evolution of the bipartite Von Neuman entropy is presented for different values of the longitudinal field and the dramatic slowdown of the entanglement growth is undeniable.

3.2 Outlook

The mechanism described above can be generalized to other ferromagnetic as well as anti-ferromagnetic models. All the concepts introduced are going to be further examined in depth in Chap. 4. We are going to study and accurately characterize the out-of-equilibrium dynamics of yet another system displaying confinement of elementary excitations: the model is a Heisenberg-Ising spin ladder in which confinement is triggered

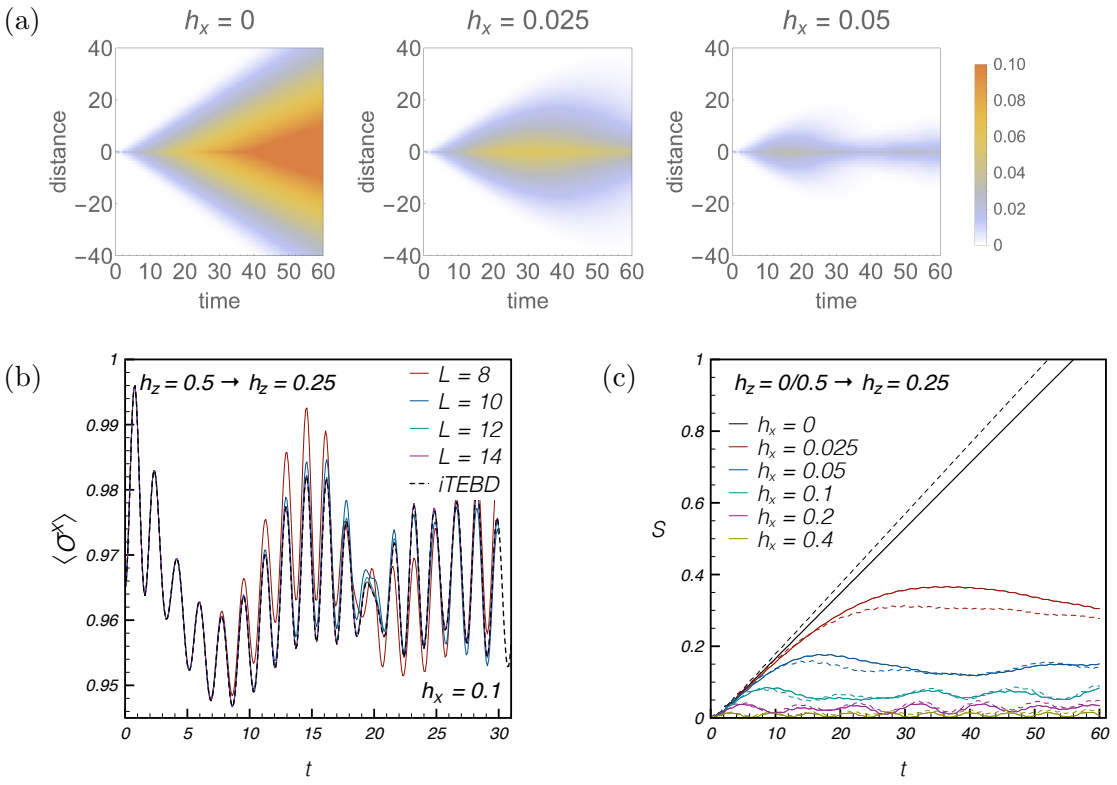

Figure 3.1: In the figures the role of h_x and h_z is exchanged with respect to Eq. 3.1. Panel (a): Time evolution of the connected correlator $\langle \sigma^z_1, \sigma^z_{1+\ell} \rangle_c$ after quenching $h_x = 0.5, h_z = 0$ to $h_z = 0.25$ and $h_x = 0.025, 0.05$. Panel (b): $\langle \sigma^x(t) \rangle$ after quenching from $h_z = 0.5, h_x = 0$ to $h_z = 0.25$ and $h_x = 0.1$. Different numerical methods in comparison: dots are iTEBD results, lines are exact diagonalisation results for $L = 8, \ldots, 14$. Panel (c): Time evolution for the bipartite Von Neuman entropy. Figure taken from [22].

by internal interactions rather than an external field. In a ladder geometry the composite excitations (mesons) have a richer variety than in purely one-dimensional systems. As we shall see, this allows for more exotic non-equilibrium phenomena characterised by different energy scales. A detailed study of the low energy sector of the model is going to be performed. Thereafter, signatures of the specific velocities of the mesons of the model are identified within the light-cone structure of two-point correlation functions. Moreover, meson masses are measured from the real time analysis of the time evolution of the order parameter.

In Chap. 5 it is going to be showed that the false vacuum decay is accessible to current optical experiments. For instance in quantum analog simulators of spin chains with confinement of the elementary excitations, which mimic the high energy phenomenology but in one spatial dimension. We study the non-equilibrium dynamics of the false vacuum

in a quantum Ising chain and in an XXZ ladder. The false vacuum is the metastable state that arises in the ferromagnetic phase of the model when the symmetry is explicitly broken by a longitudinal field. This state decays through the formation of "bubbles" of true vacuum. Using iTEBD simulations, we are able to study the real-time evolution in the thermodynamic limit and measure the decay rate of local observables. We find that the numerical results agree with the theoretical prediction that the decay rate is exponentially small in the inverse of the longitudinal field.

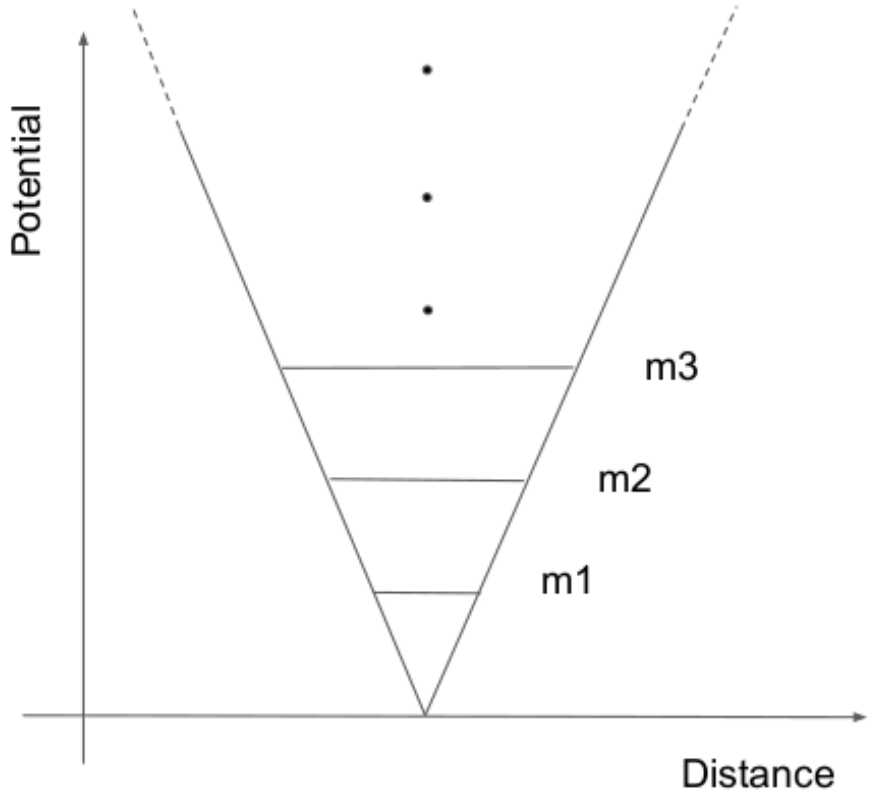

Figure 3.2: Sketch of different mesons states emerging from pair of kinks confined in a V-shaped potential.

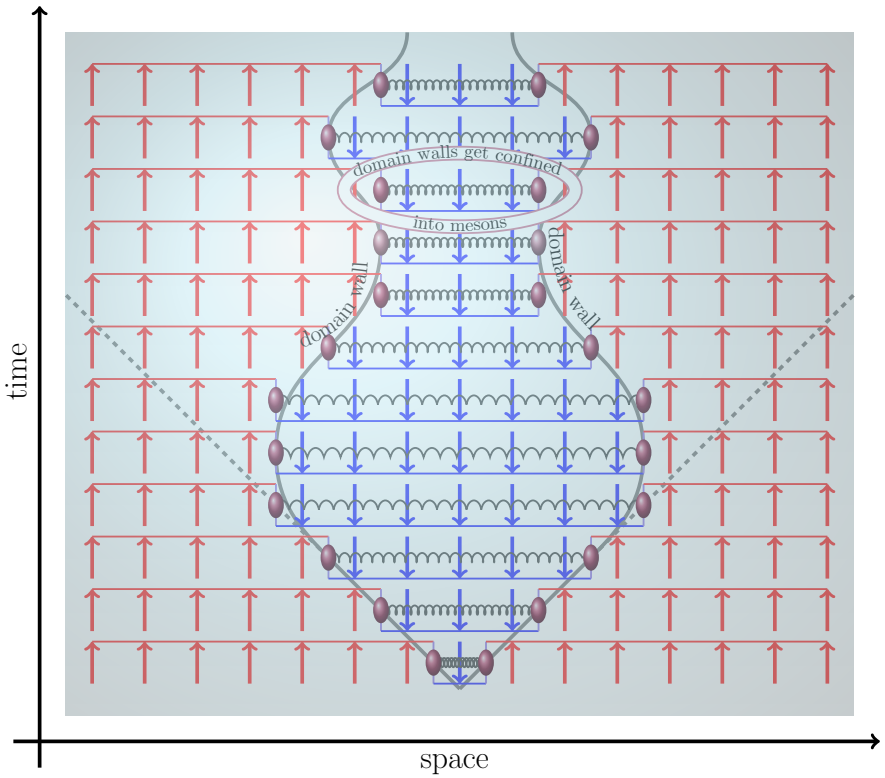

Figure 3.3: Pictorial representation of the real time dynamics of a meson in the semi-classical limit: two counter-propagating domain walls bounce back and forth because of the long range interaction provided by the longitudinal field. Figure taken from [22]

Chapter 4

Confinement in the spectrum of a Heisemberg spin ladder

In this chapter we are interested in studying the dynamics of a confining spin ladder. Fundamental results about confinement in condensed-matter systems have been achieved through the experimental study of various compounds (i.e. $KCuF_3$[166, 167, 168], Sr_2CuO_3[169] or $YbAs_3$ [170]) that can be modelled as one-dimensional systems with a certain amount of inter-chain interaction. These studies on spin ladders were partially motivated by Haldane's prediction of a gap in the excitation spectrum for integer-S antiferromagnets [171], as well as by the work of Shiba [172] who suggested that a weak inter-chain coupling between two spin 1/2 Heisenberg chain can explain the occurrence of discrete lines in the Raman spectrum of $CsCoCl_3$ and $CsCoBr_3$ [173, 174]. Consequently, quasi one-dimensional spin ladders experienced an increasing research activity and the occurrence of confinement in these models has been intensively studied [135, 136, 137, 138, 139, 140, 141, 142, 143, 144, 175, 176, 177, 178, 179, 180, 181], finally leading to remarkable observations through neutron scattering and high-resolution terahertz spectroscopy [117, 118, 119, 120, 121, 122, 123]. An astonishing result is the very recent experimental observation of the same $E8$ structure identified in the critical Ising chain in a quasi-one-dimensional antiferromagnet $BaCo_2V_2O_8$ under transverse field [182]. The model we will focus on is a spin ladder in its anti-ferromagnetic gapped phase realised as two Heisenberg XXZ spin-(1/2) chains coupled via an Ising-like interaction along the longitudinal (easy axis) direction [128, 1]. Explicitly the Hamiltonian reads

$$
\begin{aligned}
H(\Delta_{||},\Delta_{\perp}) =& \frac{J}{2}\sum_{j=1}^{L}\left[\sigma^x_{j,1}\sigma^x_{j+1,1}+\sigma^y_{j,1}\sigma^y_{j+1,1}+\Delta_{||}(\sigma^z_{j,1}\sigma^z_{j+1,1}+1)\right] \\
&+\frac{J}{2}\sum_{j=1}^{L}\left[\sigma^x_{j,2}\sigma^x_{j+1,2}+\sigma^y_{j,2}\sigma^y_{j+1,2}+\Delta_{||}(\sigma^z_{j,2}\sigma^z_{j+1,2}+1)\right] \\
&+J\Delta_{\perp}\sum_{j=1}^{L}\sigma^z_{j,2}\sigma^z_{j,1}\,.
\end{aligned}
\tag{4.1}
$$

Here $\sigma^{\alpha}_{j,k}$ denotes the Pauli spin operators at the j^{th} site of chain $k\in\{1,2\}$ and we impose periodic boundary conditions, $\sigma^{\alpha}_{L+1,k}=\sigma^{\alpha}_{1,k}$. The parameter J sets the energy scale, in the following we set it to $J=1$. We focus on the regime $\Delta_{||}\in(1,+\infty)$ for the anisotropy parameter of the chains which corresponds to their gapped antiferromagnetic phases. The last term couples the two spin chains with an Ising-like interchain interaction. Without losing generality, we set $\Delta_{\perp}>0$, i.e. an antiferromagnetic coupling of the chains. The sign of $\Delta_{\perp}$ can be reversed with a spin flip applied to one of the two chains, without altering the spectrum.

The model is highly symmetric. The z component of the total magnetization on each chain, $M_k=\sum_j\sigma^z_{j,k}$, is conserved, corresponding to two $U(1)$ symmetries. In the limiting case of zero inter-chain coupling ($\Delta_{\perp}=0$) the physics of the model is reduced to that of two independent XXZ anti-ferromagnetic spin chains and a $\mathbb{Z}_2\times\mathbb{Z}_2$ symmetry associated with the spin flip $\sigma^{y/z}_{j,k}\to-\sigma^{y/z}_{j,k}$ of each chain is displayed. The coupling $\Delta_{\perp}\neq0$ explicitly breaks this symmetry: the residual one is the global spin flip of both chains (a single $\mathbb{Z}_2$). Moreover, there is an additional symmetry related to the swapping of the chains $\sigma^{\alpha}_{j,1}\leftrightarrow\sigma^{\alpha}_{j,2}$. Finally, due to translational invariance, the energy levels are organized as eigenstates of the total momentum P.

One of the motivations to study the effects of confinement in antiferromagnetic ladders lies in the fact that, in contrast to spin chains where confinement is triggered by a symmetry-breaking field or long-range interactions, in a ladder geometry the confining potential naturally emerges as the effect of the (even small) local interaction between the chains, as can be easily seen in a mean field treatment [128, 137, 138, 139]. This mechanism is reminiscent of quark confinement in chromodynamics, where the role of the attractive potential is played by the gauge field, i.e. the mediator of strong interactions. Similarly, in a ladder, the spins of one chain are additional degrees of freedom which effectively mediate the interactions between the particles of the other chain. Consequently, the external field is not required because the staggered magnetization of one chain provides an effective staggered field for the other. There are various possible ladders featuring confinement (e.g., those composed of Ising-like chains), but many of these require an external magnetic field which imposes difficulties in prospective cold atomic realizations (see however [183]). Here we focus instead on coupled Heisenberg-type spin chains described by the Hamiltonian (5.8) in which no external field, either longitudinal or transverse, makes an appearance, making them suitable for cold atom experiments.

For example, the two chains in Eq. (5.8) can be mapped by a Jordan–Wigner transformation to spinless fermions coupled by a density-density interaction. This model can be easily realized by freezing the spin degrees of freedom in real fermion gases, e.g. utilizing the techniques of Ref. [184] for Ytterbium atoms. Alternatively, one can use the true spin degrees of freedom and freeze the charge degree of freedom in spin 1/2 fermionic condensates.

There is however a fundamental difference between confinement in ladders and chains with an external field. Indeed, since for the ladders one symmetry is spontaneously broken, there are (at least) two true ground states (vacua) and the neutral mesons with respect to the confined charge can interpolate between the same vacuum or between different ones. This feature leads to the existence of two types of neutral bound states which we dub intrachain ('Type 1') and interchain ('Type 2') mesons interpolating, respectively, between the same or different vacua. We stress that 'Type 2' interchain mesons are not charged bound states that exist in some other theories and interpolate between true and false vacua.

A recent work [179] studied the properties of bound states on an XXZ chain in the anti-ferromagnetic region with the confining potential provided by an external staggered field. This model can be interpreted as arising from a mean field treatment of the XXZ ladder in (5.8), with the staggered field encoding the mean field effect of one chain on the other [128, 137, 138, 139]. Although such a mean-field treatment is rather accurate to capture an entire family of bound states, it completely misses another one. We go beyond this approximation, and study the full system in the strong anisotropy regime. As generally anticipated above, the main new theoretical insight is that beyond the already known (intrachain) mesons that also appear in the mean field approach, we identify another class of bound states that we dub interchain mesons.

The chapter is structured in the following way. In Section 4.1 we describe the elementary excitations (intrachain and interchain mesons) and study their spectrum in the strong anisotropy regime. In Section 4.2 we use a semiclassical approach to find a more accurate estimate of the spectrum in the regime of moderate anisotropy. In Section 4.3 we introduce an approximation to capture the spectrum of two-meson states. In Section 4.4 we discuss the nature of the first excited states and find a transition as a function of the anisotropy parameters. Afterwards, in Section 4.5 we introduce the quench protocol and we study numerically its non-equilibrium dynamics. More precisely, the effects of confinement in the model are displayed through the behaviour of the entanglement entropy evolution in Subsection 4.5.1, through the spreading of two-point correlation functions in Subsection 4.5.2, and in the oscillations of the order parameter in Subsection 4.5.3. We give our conclusions in Section 4.6. In Appendix 4.A we report some details about semiclassical quantization.

4.1 Elementary excitations in the strong anisotropy regime

Our goal here is to provide an accurate description of the spectrum of the Heisenberg-Ising ladder Hamiltonian (5.8) in the regime with confining quasiparticles. To set clearly

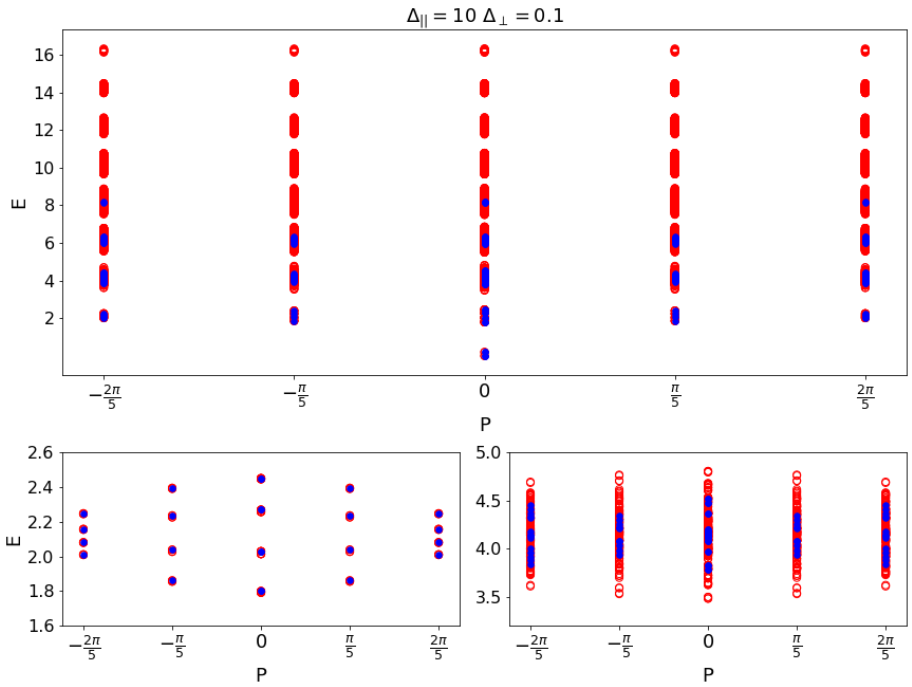

Figure 4.1: Spectrum of the Heisenberg-Ising ladder Hamiltonian (4.2) for $\Delta_{||} = 10$ and $\Delta_{\perp} = 0.1$ (red circles) compared with the XXZ-chain in a staggered field (blue symbols), see Eq. (4.4). Both spectra are in the sector of zero magnetization. *Top:* Entire spectrum of both Hamiltonians for $L = 10$. For large enough $\Delta_{||}$, the spectrum is organized in bands with fixed number of particles (kinks). The ladder has many more states than the corresponding chain. *Bottom:* Zooms of the two-particle and four-particle sectors close to energy $E \sim 2$ and $E \sim 4$ respectively. For the two-particle sector and even L, the spectra of the two models are in one-to-one correspondence (modulo a four-fold degeneracy which is resolved at higher order in ϵ). This is no longer the case for the four-particle sector (and for odd L in the two-particle sector).

the problem, we report the entire spectrum of the Hamiltonian in the sector of zero magnetization for $L = 10$, calculated numerically by means of exact diagonalization. We consider $\Delta_{||} = 10$ and $\Delta_{\perp} = 0.1$. The spectrum is organized in bands of fixed even number of particles around the energies equal to this number (in units of $\Delta_{||}$). In the figure, together with the spectrum of the ladder, we report the numerically calculated spectrum of the XXZ spin-chain in a staggered field which is a mean field description of the ladder. As can be seen clearly, the ladder has many more states than the corresponding chain, which is obvious as the Hilbert space of the ladder is exponentially larger than that of the chain. In the bottom panels, we report zooms of the two-particle and four-particle sectors. Inside each band, there is a fine structure given by states with precise quantum numbers. Here, we are after an accurate characterization of this fine structure and of the effects of confinement. A first observation that will have a very

simple explanation later is that the two-particle spectrum of the ladder is in one-to-one correspondence with that of the chain. This is true modulo a four-fold degeneracy that is a consequence of the discrete symmetries of the Hamiltonian (4.2) (spin flip and chain swap) and is lifted in higher perturbative order in $\epsilon = 1/\Delta_{||}$. We then notice that the correspondence between the chain and the ladder is not valid for the four-particle sector, where there are many more states that we will describe in the following. We stress that the correspondence between the two-particle sectors in the ladder and in the chain does not hold for odd L.

In order to understand the structure of the elementary excitations, it is instructive to focus first on the parameter regime $\Delta_{||} \gg 1$. In this Ising limit it is useful to rescale the Hamiltonian (5.8) by $\Delta_{||}$ [179], i.e.

$$\begin{aligned} H_{\mathrm{I}}(\epsilon, \Delta_\perp) = & \sum_{\alpha=1,2} \sum_{j=1}^{L} \left[\epsilon(\sigma^+_{j,\alpha}\sigma^-_{j+1,\alpha} + \sigma^-_{j,\alpha}\sigma^+_{j+1,\alpha}) + \frac{1}{2}(\sigma^z_{j,\alpha}\sigma^z_{j+1,\alpha} + 1) \right] \\ & + \epsilon\Delta_\perp \sum_{j=1}^{L} \sigma^z_{j,2}\sigma^z_{j,1} \,, \end{aligned} \tag{4.2}$$

where $\epsilon = 1/\Delta_{||}$. We study this Hamiltonian perturbatively in ϵ.

When $\epsilon = 0$, the two chains are decoupled and the hopping terms are absent. The Hamiltonian has four degenerate ground states given by the four possible combinations of the Néel $|\Psi_1\rangle = |\uparrow\downarrow\uparrow\downarrow \dots\rangle$ and anti-Néel $|\Psi_2\rangle = |\downarrow\uparrow\downarrow\uparrow \dots\rangle$ states of the two chains (here $|\uparrow\rangle$ is chosen with quantization axis in the z direction, i.e., $\sigma^z_j|\uparrow\rangle = |\uparrow\rangle$). In the units of Eq. (4.2) all these ground states have exactly zero energy for $\epsilon = 0$. The fundamental excitations of each chain are kinks $|K_{\alpha\beta}(j)\rangle$ interpolating between the two vacua $|\Psi_\alpha\rangle$ and $|\Psi_\beta\rangle$ ($\alpha, \beta \in \{1,2\}, \alpha \neq \beta$) at the bond between sites j and $j+1$ (cf. Fig. 4.2). Depending on the orientation of the neighbouring spins, each domain wall can carry spin $s = +1/2$ (in the case $\uparrow\uparrow$) or $s = -1/2$ (if $\downarrow\downarrow$): note that the spin s and the parity of the site $\rho = j \bmod 2$ on the chain $\alpha \in \{1,2\}$ are related by $s = (-1)^\alpha(1/2 - \rho)$. For $0 < \epsilon \ll 1$ and $\Delta_\perp = 0$, the exactly known ground states of the chains are still almost Néel and anti-Néel states, but their degeneracy is lifted for finite L yielding exponentially small (in L) splittings. Similarly, the hopping term hybridizes the kink states and lifts their extensive degeneracy. Moreover, in the $\epsilon \to 0$ expansion the kinks are associated to the dispersion relation

$$\omega(p) = 1 - 2\varepsilon \cos 2p. \tag{4.3}$$

Because each chain is in an anti-ferromagnetic phase with two degenerate ground states, the ladder made of two decoupled spin chains has a four-fold degenerate ground state manifold ($|\Psi_{++}\rangle$, $|\Psi_{+-}\rangle$, $|\Psi_{-+}\rangle$, $|\Psi_{--}\rangle$, where the shorthand stands for $|\Psi_{ij}\rangle = |\Psi_i\rangle_1 \otimes |\Psi_j\rangle_2$ with $i, j = \pm$ and $1, 2$ referring to the two chains) that is split by an inter-chain coupling $\Delta_\perp \neq 0$. For $\Delta_\perp \gtrsim 0$, $|\Psi_{+-}\rangle$ and $|\Psi_{-+}\rangle$ are the two degenerate ground states, whereas $|\Psi_{++}\rangle$ and $|\Psi_{--}\rangle$ acquire an extensive energy gap $\sim L\Delta_\perp$ on top of the ground state (for $\Delta_\perp < 0$ the opposite is true). In the thermodynamic limit, the latter two become *false vacua* and together with all the formerly low lying

excitations above them are pushed to the top of the spectrum. On the ladder a single kink in one of the two chains toggles between a true and a false vacuum (illustrated in grey and red, respectively, in Fig. 4.2). This implies that the nature of the low-lying excitations change qualitatively when the coupling between the chains is turned on. The low energy sector only bears states with an even number of kinks since there must be a true vacuum both on the left and on the right of these states. Consequently, states made with two kinks become the elementary excitations in the spectrum. The energy acquired by the false vacuum between the two kinks induces an effective linear potential between them: the two kinks are confined in excitations that we call *mesons*, following a standard terminology in the literature. Because of the presence of two true vacua, we can distinguish between two classes of mesons: 'Type 1' *intra-chain* mesons are interpolating between the same vacuum while 'Type 2' *inter-chain* mesons are interpolating between two different vacua (see Fig. 4.2 to grasp the idea with a graphical representation).

We now illustrate more clearly the difference between these two mesons in terms of the symmetries of the model. For $\Delta_\perp = 0$ the model has a $\mathbb{Z}_2 \times \mathbb{Z}_2$ symmetry associated with the total spin flip along each chain. A kink on a given chain has a non-zero $\mathbb{Z}_2$ charge for the spin-flip symmetry on that chain. When $\Delta_\perp$ is turned on, the symmetry is explicitly broken and only one $\mathbb{Z}_2$ symmetry is left (i.e. the global spin-flip of both chains). A charge Q can be assigned to the explicitly broken symmetry: this charge corresponds to the parity of the total number of kinks. As a consequence of confinement, the low-energy spectrum can harbour only neutral objects, while charged objects are pushed up in the spectrum. Both 'Type 1' and 'Type 2' mesons are neutral with respect to this symmetry, i.e. they have $Q = 0$. The remaining $\mathbb{Z}_2$ symmetry is spontaneously broken in the ground state. Another charge q may be assigned to this different symmetry: 'Type 1' mesons correspond to $Q = 0$ and $q = 0$ while 'Type 2' to $Q = 0$ and $q = 1$. Very importantly, since this second symmetry is not explicitly broken, low-energy states do not need to be neutral with respect to q. On the contrary, it is possible to have charged excitations ('Type 2' mesons) which are the sort of composite kinks for the spontaneously broken global spin-flip symmetry. While at first, this phenomenon can sound rather peculiar, it is actually very similar to what happens for strong interactions: the mesons are neutral particles for the color charge but they are not for the electrical charge, related to another symmetry of nature.

In finite volume L, because of periodic boundary conditions, chains with an odd number of sites can host an odd number of kinks while chains with an even number of sites can host an even number of kinks. Namely, for L odd there are only $q = 1$ states while for L even only $q = 0$ states (the opposite holds for anti-periodic boundary conditions). Consequently, as long as $\Delta_\perp \ll \Delta_{||}$, the lowest energy states are 'Type 1' mesons if L is even and 'Type 2' mesons if L is odd. In the following, we give a quantitative account of their dispersion relation both for an infinite system and for a ladder of finite size. The approach we exploit here is rather standard: we project the many-body Hilbert space onto the 2-kink sector yielding an effective two-body Hamiltonian which can be treated with elementary quantum mechanics techniques. As discussed above, the degeneracy of the ground and excited states gets lifted at the first order in ϵ, thus the dispersion

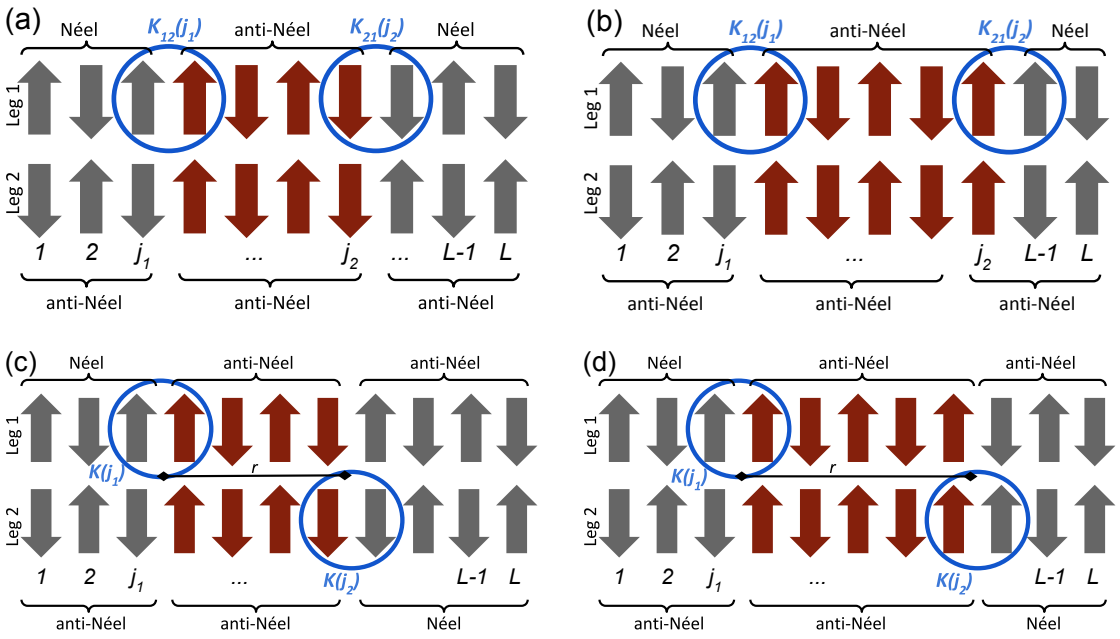

Figure 4.2: Schematic picture of the possible mesons in the ladder. In (a) and (b) we have 'Type 1' intrachain mesons built from two kinks on the same chain. Instead, in (c) and (d) we have 'Type 2' interchain mesons built from two kinks on the different chains. 'Type 1' mesons interpolate between the same kind of vacua, while 'Type 2' mesons interpolate between vacua of different kind. The coupling $\Delta_\perp$ induces a linear potential between the kinks, because the energy cost scales with the distance of the kinks equal to the number of spins that have frustrated interchain links (shown in red). This distance is even for kinks of opposite spins (a,c) and odd for kinks of the same spin (b,d).

relation of the low-energy meson excitations, which correspond to the low lying many-body levels, can be well described by a first order perturbative analysis in ϵ restricted to the two-kink sector.

4.1.1 'Type 1' intrachain mesons

'Type 1' or intrachain mesons are formed by kinks on the same chain, as shown in Fig. 4.2. In the regime $\Delta_\perp \ll \Delta_{||} = \epsilon^{-1}$, the interchain interaction can be studied in a mean field fashion [128, 137, 138, 139], by focusing on one of the chains and treating the spontaneous staggered magnetization $\bar{\sigma}$ of the other chain as an effective external field:

$$\hat{H}_{\rm S}(\epsilon, h) = \sum_{j=1}^{L} \left[\epsilon \left(\sigma_j^+ \sigma_{j+1}^- + \sigma_j^- \sigma_{j+1}^+ \right) + \frac{1}{2}(\sigma_j^z \sigma_{j+1}^z + 1) \right] + \epsilon h \sum_{j=1}^{L} (-1)^j \sigma_j^z \,. \tag{4.4}$$

where $h = \bar{\sigma}\Delta_\perp$. Here we assume that the other chain is in the approximate anti-Néel state; the Néel case follows by the global spin flip symmetry. In the limit $\Delta_{||} \gg 1$, the

staggered magnetization is $\bar{\sigma} \approx 1$. The excitations of the infinite antiferromagnetic chain (i.e. Hamiltonian (4.4) with $L \to \infty$) and their confinement have been studied using various approximations in Ref. [179]. Here we extend the analysis of this work to finite chains. We introduce the projector $\hat{P}_2$ onto the 2-kink subspace spanned by the basis $|K_{\alpha\beta}(j_1)K_{\beta\alpha}(j_2)\rangle$. The action of the projected Hamiltonian $\hat{H}_2 = \hat{P}_2\hat{H}_{\rm S}\hat{P}_2$ on 2-kink states is easily worked out as

$$\begin{aligned}\hat{H}_2(\epsilon,\Delta_\perp)|K_{\alpha\beta}(j_1)K_{\beta\alpha}(j_2)\rangle = \\ &[2+(-1)^\alpha \epsilon h(L-2j)]\,|K_{\alpha\beta}(j_1)K_{\beta\alpha}(j_2)\rangle \\ +\epsilon\big\{&[|K_{\alpha\beta}(j_1-2)K_{\beta\alpha}(j_2)\rangle + |K_{\alpha\beta}(j_1)K_{\beta\alpha}(j_2+2)\rangle]\,(1-\delta_{j,L-1})(1-\delta_{j,L-2}) \\ &+[|K_{\alpha\beta}(j_1)K_{\beta\alpha}(j_2-2)\rangle + |K_{\alpha\beta}(j_1+2)K_{\beta\alpha}(j_2)\rangle]\,(1-\delta_{j,1})(1-\delta_{j,2})\big\}\,,\end{aligned} \tag{4.5}$$

where $1 \le j = j_2 - j_1 \le L-1$. The first line gives the effective potential, while the second and third lines describe the hopping of the kinks by two sites. The Kronecker-delta factors encode the hard-core nature of the kinks.

Exploiting translational invariance by 2 sites, we are looking for the energy eigenfunctions in the sector of total spin s in the form

$$|\Psi_n(s=\pm1)\rangle = \sum_{j_1=\frac{3-s}{2}}^{L-\frac{1+s}{2}}{}' \sum_{r=1}^{L-1}{}' \psi_n^{(s)}(r|P)e^{iP(j_1+r/2)}|K_{12}(j_1)K_{21}(j_1+r)\rangle\,, \tag{4.6a}$$

$$|\Psi_n^{(\rm o)}(s=0)\rangle = \sum_{j_1=1}^{L-1}{}' \sum_{r=2}^{L-2}{}' \psi_n^{(\rm o)}(r|P)e^{iP(j_1+r/2)}|K_{12}(j_1)K_{21}(j_1+r)\rangle\,, \tag{4.6b}$$

$$|\Psi_n^{(\rm e)}(s=0)\rangle = \sum_{j_1=2}^{L}{}' \sum_{r=2}^{L-2}{}' \psi_n^{(\rm e)}(r|P)e^{iP(j_1+r/2)}|K_{12}(j_1)K_{21}(j_1+r)\rangle\,, \tag{4.6c}$$

where the primed sums run over odd or even integers, and the momentum of the center of mass P is quantized as $P = k\,2\pi/L$, $k = -\lfloor \frac{L}{4} \rfloor, \ldots, \lfloor \frac{L}{4} \rfloor$. The limited range of the momentum reflects the doubling of the unit cell due to the staggered background field. The "o/e" superscripts refer to the odd and even sites on which the kinks are located. The parity of the distance r is fixed by the spin of the kinks: $r = 2, 4, \ldots L-2$ if the total spin is 0 and $r = 1, 3, \ldots L-1$ if the total spin is ±1 (see Fig. 4.2).

Using these expressions, the eigenvalue problem of $\hat{H}_2$ leads to the discrete Sturm–Liouville equation

$$(2+2\epsilon\Delta_\perp\, r)\psi_n^{(a)}(r) + 2\epsilon\cos(P)\big[\psi_n^{(a)}(r+2) + \psi_n^{(a)}(r-2)\big] = E_n^{(a)}(P)\,\psi_n^{(a)}(r), \tag{4.7}$$

for all relative wave functions $\psi_n^{(a)}(r|P)$, $a \in \{+1, -1, \mathrm{o}, \mathrm{e}\}$. Here E_n are the excitation energies with respect to the ground state energy $\mathcal{E}_{\rm GS} = -\epsilon\Delta_\perp L$. The boundary conditions are $\psi_n^{(\pm1)}(-1) = \psi_n^{(\pm1)}(L+1) = 0$ and $\psi_n^{(\rm o/e)}(0) = \psi_n^{(\rm o/e)}(L) = 0$. The solutions can be written down exploiting the recurrence relation satisfied by the Bessel functions of

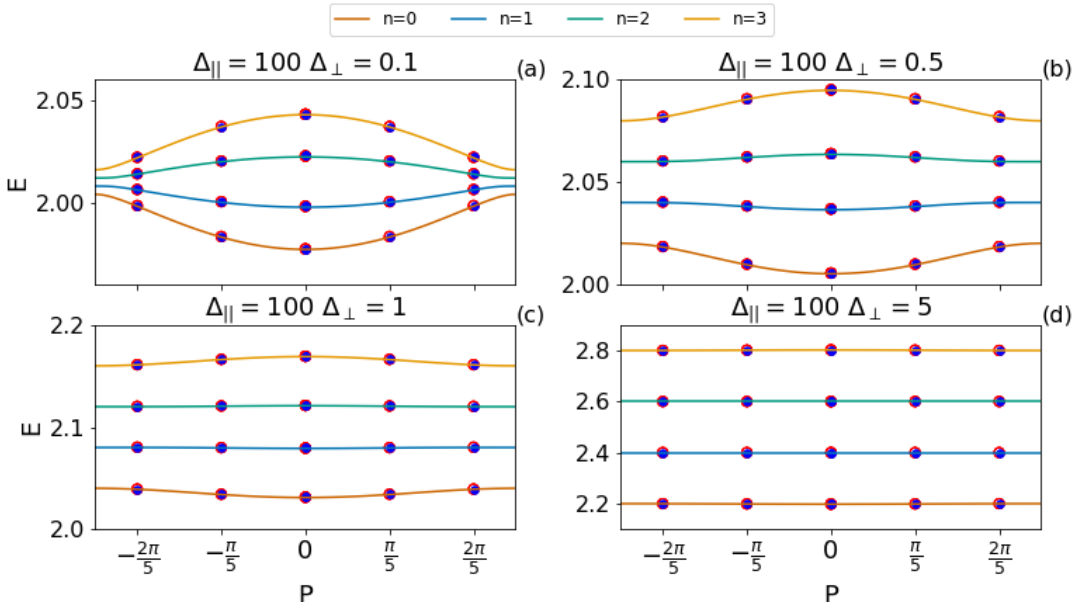

Figure 4.3: Low-lying part of the spectrum in the spin $s = 0$ sector of the ladder in Eq. (4.2) (red circles) and of the staggered XXZ chain in Eq. (4.4) (blue dots) for $L = 10$, $\Delta_{||} = 100$, and $\Delta_\perp = 0.1, 0.5, 1, 5$. The numerical data have been obtained by exact diagonalization. The dispersion relations of the mesons in the 2-kink approximation (4.9) are shown in continuous lines, obtained by solving Eq. (4.7) numerically. The internal quantum number n of each curve is in the legend on top of the plot. In the strong anisotropy regime, and for even L, the ladder is equivalent to the staggered XXZ chain in the two-kink sector.

the first $J_{\nu+1}(z) + J_{\nu-1}(z) = 2\nu/z\, J_\nu(z)$ and similarly for and the second kind $Y_\nu(z)$, obtaining

$$\psi_n^{(a)}(r|P) = N_n^{(a)} \left[J_{\nu_n^{(a)}(P)-r/2}(\Delta_\perp^{-1} \cos P) + A_n^{(a)}\, Y_{\nu_n^{(a)}(P)-r/2}(\Delta_\perp^{-1} \cos P) \right] , \qquad (4.8)$$

where $N_n^{(a)}(P)$ is the normalization and $\nu_n^{(a)}(P)$ and $A_n^{(a)}(P)$ are determined by the boundary conditions. These solutions are labeled by the integer n and their energy eigenvalues are

$$E_n^{(a)}(P) = 2 + 4\epsilon\Delta_\perp\, \nu_n^{(a)}(P)\,. \qquad (4.9)$$

We plot the energy levels $E_n(P)$ obtained by solving Eq. (4.7) (or equivalently Eq. (4.9)) for $L = 10$ in the case of total spin $s = 0$ in Fig. 4.3. These analytic predictions are compared to the exact diagonalization results both for the ladder Hamiltonian (4.2) and for the staggered chain Hamiltonian (4.4) for $\Delta_{||} = 100$ and different values of the interchain coupling $\Delta_\perp$. For these couplings, the low energy part of the ladder spectrum matches perfectly the spectrum of the staggered XXZ chain. Moreover, both spectra are well captured by the 2-kink approximation.

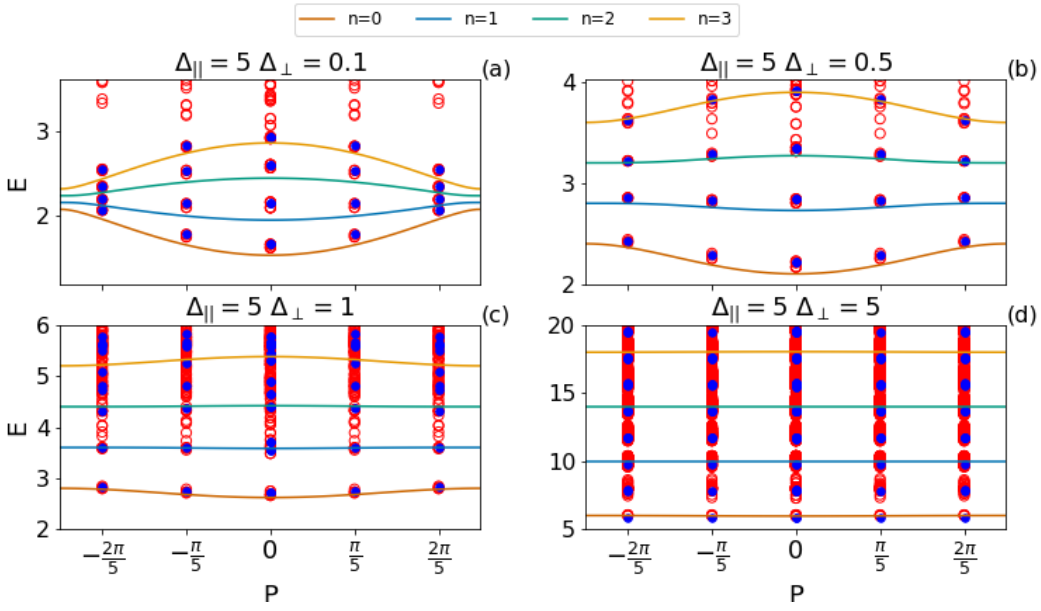

Figure 4.4: Low-lying part of the spectrum in the spin $s = 0$ sector of the ladder in Eq. (4.2) (red circles) and of the staggered XXZ chain in Eq. (4.4) (blue dots) obtained by exact diagonalization for $L = 10$, $\Delta_{||} = 5$, and $\Delta_\perp = 0.1, 0.5, 1, 5$. The dispersion relations of the mesons in the 2-kink approximation are shown in continuous lines, obtained by solving Eq. (4.7) numerically. The internal quantum number n is in the legend on top of the plot.

In Fig. 4.4 we explore the robustness of this effective description as we move away from the strong anisotropic region by reporting a comparison with the numerical results from exact diagonalization for a ladder of length $L = 10$ with $\Delta_{||} = 5$. Even though the quantitative agreement is worse for $\Delta_{||} = 5$ than for $\Delta_{||} = 100$, the effective two-kink Hamiltonian still represents a good qualitative description of the low energy states as long as the energy bands of different kink numbers are well separated. Indeed, the main qualitative effect is that as $\Delta_\perp$ increases (at fixed $\Delta_{||}$), some high energy states, which are not captured by the mean-field staggered XXZ chain, come down to low energy and mix up (and at some point hybridize) with the part of the spectrum we are able to describe. At a more quantitative level, even for the smallest values of $\Delta_\perp$ we observe deviations that anyhow were expected. Indeed, as $\Delta_{||}$ is decreased, the fundamental excitations interpolate between vacua that cannot be approximated by a Néel or an anti-Néel state. Moreover, the nontrivial scattering properties of those excitations will start to play a role. Both effects will be investigated in the next section.

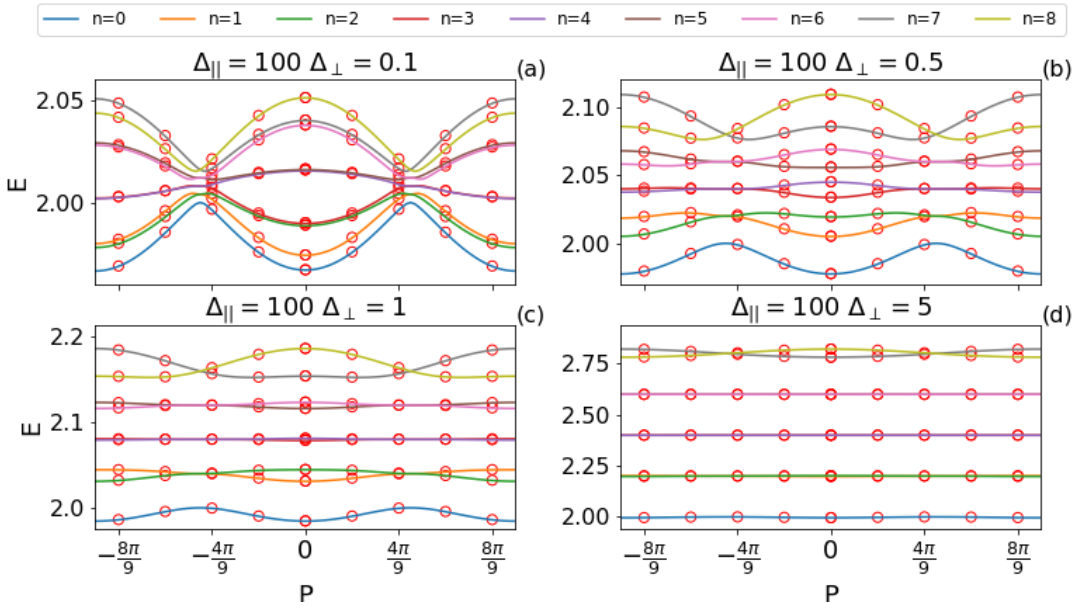

Figure 4.5: Low-lying part of the spectrum in the spin sector $s = 0$ of the ladder (4.2) (red circles) for $L = 9$, $\Delta_{||} = 100$, and $\Delta_\perp = 0.1, 0.5, 1, 5$. The dispersion relations of the mesons in the 2-kink approximation (4.14) are shown in continuous lines, obtained by solving Eq. (4.11) numerically. The internal quantum number n is in the legend on top of the plot. Notice many qualitative different features compared to the ladder of even length in Fig. 4.3.

4.1.2 'Type 2' interchain mesons

We now turn to the meson excitations that are formed by two kinks located on different chains (see Fig. 4.2). On a ladder with periodic boundary condition, these states can only exist for L odd, and they have no equivalent in a staggered XXZ chain.

We can follow steps very similar to those for intrachain mesons in the previous subsection. We first project onto states having one kink on each leg of the ladder. The main difference is that in this case there is no hard-core constraint for the kinks as they can cross by passing above/below each other and hence their wave function is

$$|\Psi_n(s)\rangle = \sum_{j_1=1}^{L} \sum_{r=0}^{L-1} \phi_n(r|P,s) e^{iP(j_1+r/2)} |K(j_1)\rangle_1 |K(j_1+r)\rangle_2 \,, \tag{4.10}$$

where the subscripts $1, 2$ label the legs of the ladder. The spins of the kinks should add up to s. The center of mass momentum P is quantized as $P = k\,2\pi/L$, $k = -\left\lfloor \frac{L}{2} \right\rfloor, \ldots, \left\lfloor \frac{L}{2} \right\rfloor$.

The equation for the relative wave function in all spin sectors turns out to be

$$(2 + 2\epsilon\Delta_\perp \ell_s(r))\phi_n(r) + 2\epsilon\cos(P)\left[\phi_n(r+2) + \phi_n(r-2)\right] = E_n(P)\,\phi_n(r), \tag{4.11}$$

with $r = 0, 1, \dots L-1$. The function $\ell_s(r)$ is the length of the string between the kinks and is defined as

$$\ell_{s=0}(r) = \begin{cases} r \text{ if } r \text{ even} \\ L-r \text{ if } r \text{ odd}, \end{cases} \qquad \ell_{s=\pm 1}(r) = \begin{cases} r \text{ if } r \text{ odd} \\ L-r \text{ if } r \text{ even}. \end{cases} \tag{4.12}$$

Note that swapping the chains corresponds to $r \leftrightarrow L-r$ which also changes the parity of r, thus the definitions (4.12) are consistent with this symmetry. The boundary conditions are $\phi_n(-2) = \phi_n(L-2)$, $\phi_n(2) = \phi_n(L+2)$, and $\phi_n(-1) = \phi_n(L-1)$, $\phi_n(1) = \phi_n(L+1)$. The solutions are given by

$$\phi_n^{(\pm)}(r|P,s) = (\pm)^r N_n^{(\pm)}(P,s) \left[J_{\nu_n^{(\pm)}(P,s)-\ell(r)/2}(\Delta_\perp^{-1}\cos P) + \right. \\ \left. + A_n^{(\pm)}(P,s)\, Y_{\nu_n^{(\pm)}(P,s)-\ell(r)/2}(\Delta_\perp^{-1}\cos P) \right] , \tag{4.13}$$

where $N_n^{(\pm)}(P,s)$ is the normalization, $\nu_n^{(\pm)}(P,s)$ and $A_n^{(\pm)}(P,s)$ are fixed by the boundary conditions which now relate the wave function at odd and even sites. Notice that the four boundary conditions give only two independent equations. $\phi_n^{(+)}(r)$ are symmetric, while $\phi_n^{(-)}(r)$ are anti-symmetric under the exchange $r \leftrightarrow L-r$. The energies are given by

$$E_n^{(\pm)}(P,s) = 2 + 4\epsilon\Delta_\perp\, \nu_n^{(\pm)}(P,s)\,. \tag{4.14}$$

In Fig. 4.5 we compare the levels obtained from Eq. (4.14) with the results of exact diagonalization of the ladder Hamiltonian for $L = 9$ in the spin sector $s = 0$ for $\Delta_{||} = 100$ and different values of the interchain coupling $\Delta_\perp$. Similarly to the intrachain mesons, the spectrum is very well captured by the effective 2-kink description. The figure also demonstrates the richer structure of the 'Type 2' interchain mesons as they have about twice as many internal excitations as the 'Type 1' intrachain mesons have.

In Fig. 4.6 the same comparison is shown for $\Delta_{||} = 5$ and various values of $\Delta_\perp$. Analogously to the case of 'Type 1' mesons, the overall structure of the spectrum is captured by the 2-kink approximation in the regions where the bands are well separated. The deviations of exact numerical results from the 2-kink approximation are more pronounced than for $\Delta_{||} = 100$, because the dressing of the fundamental excitations becomes relevant for small $\Delta_{||}$.

We conclude this section by mentioning that bound states between two coupled 1+1 dimensional models have been observed also in conformal field theories [311], but in a very different context that does not lead to confinement.

4.2 A semiclassical approach for finite $\Delta_{||}$

When approaching smaller values of the anisotropy parameter $\Delta_{||}$ at $\Delta_\perp = 0$, the ground state of the model and its fundamental excitations experience significant changes. The doubly degenerate ground states $|\Psi_+\rangle$ and $|\Psi_-\rangle$ of both chains still have antiferromagnetic order but with a smaller average staggered magnetization $\pm\bar{\sigma}$. The latter

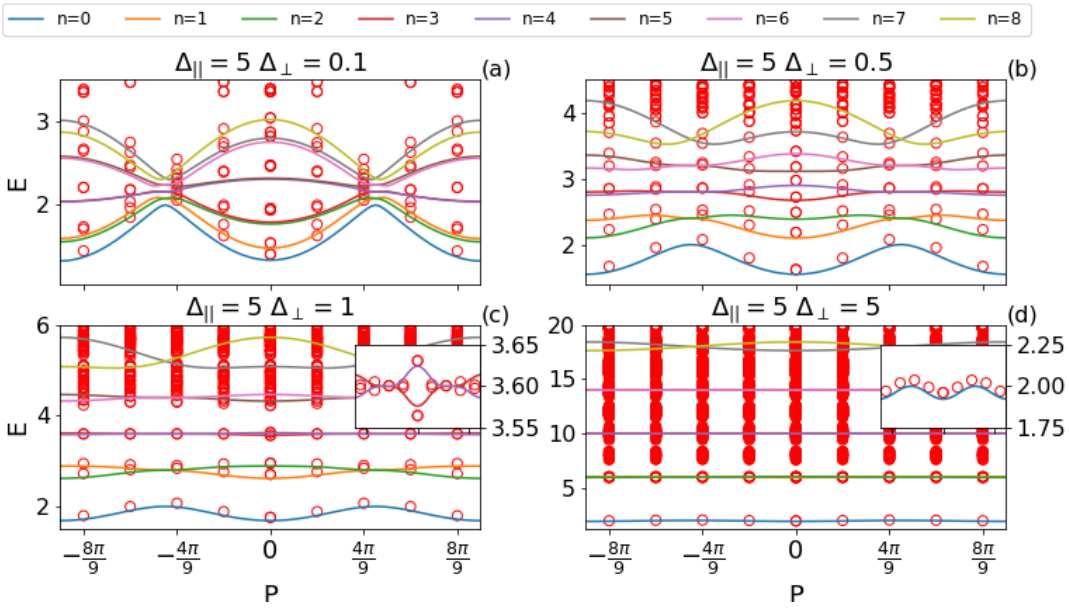

Figure 4.6: Low-lying part of the spectrum in the spin sector $s = 0$ of the ladder (4.2) (red circles) for $L = 9$, $\Delta_{||} = 5$, and $\Delta_\perp = 0.1, 0.5, 1, 5$. The dispersion relations of the mesons in the 2-kink approximation (4.14) are shown as continuous lines, obtained by solving Eq. (4.11) numerically. The internal quantum number n is in the legend on top of the plot. The insets show the accuracy of our approximation in resolving the spectrum on a more refined scale.

is exactly known from the Bethe ansatz solution of the XXZ spin chain and it is given by

$$\bar{\sigma} = \prod_{n=1}^{\infty} \left(\frac{1 - e^{-2n\gamma}}{1 + e^{-2n\gamma}} \right)^2 , \qquad \Delta_{||} = \cosh(\gamma) \, . \tag{4.15}$$

As $\Delta_{||}$ decreases, the ground states with the above staggered magnetization are no longer well approximated by a Néel or an anti-Néel state. The elementary excitations are still topological quasiparticles that interpolate between the two vacua. Like their $\Delta_{||} \to +\infty$ counterpart, they carry half-integer spin $s = \pm 1/2$. However, due to the properties of the model, they are strongly interacting particles with non-trivial dispersion relation and scattering phase. The low-energy sector of the spectrum of the model still is dominated by the two kind of bound states so far described , however the illustration in Figure 4.2 is a faithful picture of the mesons only in the limit $\Delta_{||} \to \infty$. Nonetheless, it holds qualitatively as long as we are in the gapped anti-ferromagnetic phase $\Delta_{||} > 1$. In this section we describe how these properties affect the 'Type 1' intrachain mesons. The most pragmatic way to treat the presence of a non-vanishing $\Delta_\perp$ would be a perturbative expansion in small $\Delta_\perp$ around the exact eigenstates at $\Delta_\perp = 0$. The latter approach is rather technical and involves a Bethe–Salpeter equation with a perturbative form factor expansion. Although less rigorous, here we follow another, more heuristic approach

whose main advantage is having a straightforward physical interpretation. Following Ref. [130], the idea is to look for semi-classical bound states of the Hamiltonian

$$H(x_1, x_2, \vartheta_1, \vartheta_2) = \omega(\vartheta_1) + \omega(\vartheta_2) + f(|x_2 - x_1|)\,, \tag{4.16}$$

where

$$f = 2\epsilon\Delta_\perp \bar{\sigma}^2, \tag{4.17}$$

is the "string tension" taking into account the average magnetization of both chains, and we introduced the continuum coordinates $x_1, x_2 \in \mathbb{R}$ and their canonical conjugate momenta ϑ_1, ϑ_2. The function $\omega(\vartheta)$ is the lattice dispersion relation of the kink quasiparticle obtained by a Bethe Ansatz approach [185]

$$\omega(\vartheta) = \frac{2\epsilon K(k)}{\pi} \sinh\gamma\sqrt{1 - k^2\cos^2\vartheta}\,, \tag{4.18}$$

where $K(k)$ is the complete elliptic integral whose modulus k is related to the anisotropy through the relation $K(\sqrt{1-k^2})/K(k) = \gamma/\pi$. The Hamiltonian (4.16) describes the classical motion of two particles experiencing a long range interaction with kinetic energy given by the exact kinetic energy of a kink of the XXZ chain. After a canonical transformation to center of mass and relative coordinates,

$$X = \frac{x_1 + x_2}{2}\,, \qquad\qquad x = x_2 - x_1\,, \tag{4.19}$$

$$\Theta = \vartheta_1 + \vartheta_2\,, \qquad\qquad \vartheta = \frac{\vartheta_2 - \vartheta_1}{2}\,, \tag{4.20}$$

the Hamiltonian reads

$$H(X, \Theta; x, \vartheta) = \varepsilon(\vartheta|\Theta) + f|x|, \tag{4.21}$$

with $\varepsilon(\vartheta|\Theta) = \omega(\Theta/2 - \vartheta) + \omega(\Theta/2 + \vartheta)$. In these new variables, the equations of motion are

$$\dot{X} = \frac{\partial\varepsilon}{\partial\Theta}\,, \qquad\qquad \dot{\Theta} = 0\,, \tag{4.22}$$

$$\dot{x} = \frac{\partial\varepsilon}{\partial\vartheta}\,, \qquad\qquad \dot{\vartheta} = -f\,\mathrm{sgn}(x)\,. \tag{4.23}$$

The total momentum Θ is an integral of motion as well as the energy

$$E = \varepsilon(\vartheta|\Theta) + f|x|\,. \tag{4.24}$$

The bound state energies can be obtained via the Bohr–Sommerfeld quantization condition which reads as

$$\oint \vartheta dx = 2\pi(n + \delta)\,, \qquad\qquad n = 0, 1, 2, \ldots, \tag{4.25}$$

where the integral is taken over the closed path in the (ϑ, x) classical phase space, and δ is a phase shift discussed below. In principle, the energies obtained from this

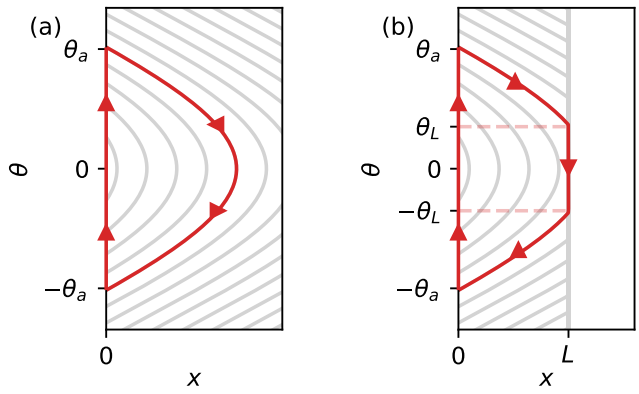

Figure 4.7: Classical trajectories in phase space (x, θ) for the Bohr–Sommerfeld quantization. The grey lines are the various trajectories at fixed energy. In infinite volume, the trajectories are always like the red one depicted in (a). In finite volume L we have a hard cutoff that deforms some trajectories as reported in (b).

equation become more and more accurate with increasing n. For simplicity, we restrict the analysis to the case when $\varepsilon(\vartheta|\Theta)$ has a single minimum at $\vartheta = 0$ which holds for $\Theta < \Theta_c = \arccos\left(\frac{1-\sqrt{1-k^2}}{1+\sqrt{1-k^2}}\right)$ [179]. The path is an arc in the $x > 0$ half plane (see Fig. 4.7-a) parameterized using Eqs. (4.24) and (4.23) starting from $x(0) = 0^+, \vartheta(0) = \vartheta_a$:

$$x(t) = \frac{E - \varepsilon(\vartheta(t)|\Theta)}{f}\,, \tag{4.26}$$

$$\vartheta(t) = \vartheta_a - ft\,, \tag{4.27}$$

where ϑ_a satisfies $E = \varepsilon(\vartheta_a|\Theta)$. The turning point is at

$$x_{\max} = \frac{E - \varepsilon(0|\Theta)}{f}, \tag{4.28}$$

and is reached at time $t_{\max} = \vartheta_a/f$. After another $t_{\max}$ time elapses, the two kinks scatter at $x(2t_{\max}) = 0$ which abruptly flips the sign of ϑ, so the phase space path is closed by a straight segment at $x = 0$ connecting $-\vartheta_a$ with ϑ_a. These phase space paths are reported in Fig. 4.7-a. The left hand side of Eq. (4.25) reads

$$\begin{aligned}\oint \vartheta dx &= -\int_{-\vartheta_a}^{\vartheta_a} d\vartheta\vartheta \frac{dx(\vartheta)}{d\vartheta} = -\frac{1}{f}\int_{-\vartheta_a}^{\vartheta_a} d\vartheta\vartheta\dot{x}(\vartheta) \\ &= \frac{1}{f}\int_{-\vartheta_a}^{\vartheta_a} d\vartheta\vartheta \frac{\partial\varepsilon(\vartheta|\Theta)}{\partial\vartheta} = \frac{1}{f}\left(2E\vartheta_a - \int_{-\vartheta_a}^{\vartheta_a} d\vartheta\varepsilon(\vartheta|\Theta)\right)\,,\end{aligned} \tag{4.29}$$

where Eq. (4.23) was used to trade the time derivative for a derivative with respect to $-\vartheta$.

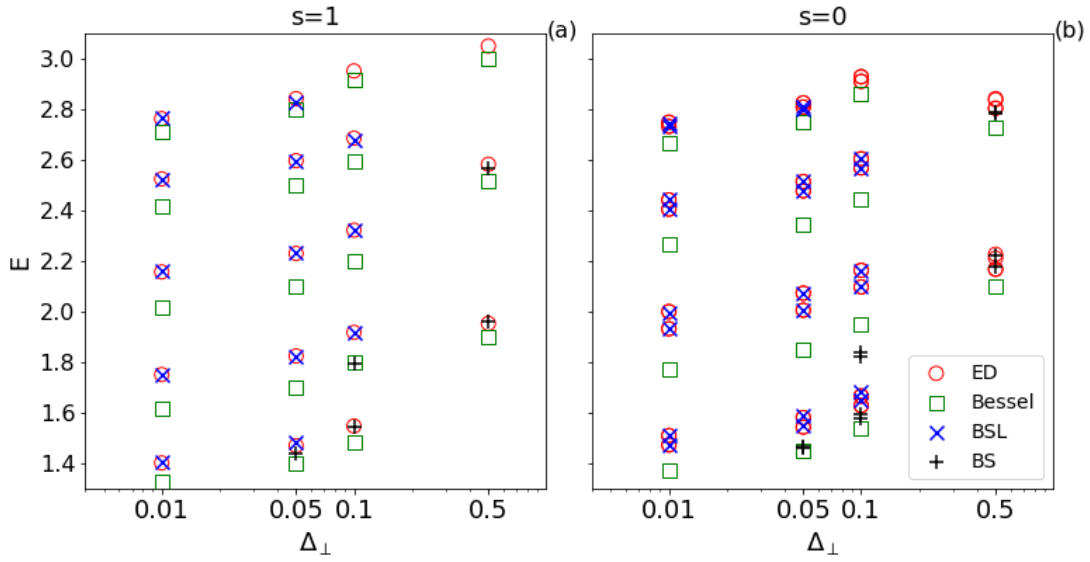

Figure 4.8: Comparison of various approximations for the intrachain meson energies at $\Delta_{||} = 5$ in the sectors with spin $s = 0$ (right) and $s = 1$ (left), both with total momentum $P = 0$. The exact diagonalization results are shown in red empty circles. The full symbols correspond to the 2-kink approximation of Sec. 4.1.1 ("Bessel"), the infinite volume semiclassical ("BS") and the finite volume semiclassical ("BSL") results according to the color code shown in the legend.

The phase shift δ receives two kinds of contributions. First, at the regular turning point there is a $\pi/2$ phase shift ($\delta = 1/4$). Second, at $x = 0$ we have to take into account the scattering phase shift of the particles. In the Ising regime $\Delta_{||} \gg 1$, the kinks behave as free hard core particles, so their scattering phase shift is simply π. This is equivalent to enforcing that the relative wave function vanish at the origin, and leads to $\delta = 1/2$, the same as for a particle suffering a hard reflection. Away from the Ising limit the kinks have a nontrivial, momentum-dependent scattering phase shift $\phi_\eta(p_1, p_2)$ that can be obtained via Bethe ansatz (see Appendix 4.A for its detailed expression). The index η accounts for the spins of the kinks and will be dropped from now on to simplify the notation. This phase needs to be added to the left hand side of Eq. (4.25), which leads to

$$2E(\vartheta_a) - \int_{-\vartheta_a}^{\vartheta_a} dq\, \varepsilon(\vartheta|\Theta) = 2\pi f \left(n + \frac{3}{4}\right) + f\,\phi\left(\frac{\Theta}{2} - \vartheta_a, \frac{\Theta}{2} + \vartheta_a\right) . \tag{4.30}$$

The procedure has to be modified in finite volume, when the maximum separation $x_{\max}$ can become larger than the system size L. There are two possible cases depending on the value of $x_{\max}$. If $x_{\max} < L$, then the energy levels are given by the solutions

Figure 4.9: Schematic pictures of 4-kink states for a ladder of even length: (a) a 4-kink state composed of two intrachain mesons and (b) a 4-kink state composed of two interchain mesons.

of Eq. (4.30), while for $x_{\max} > L$ the system does not reach the turning point but experiences another scattering at $x = L$. The integration paths in phase-space are shown for the two cases in Fig. 4.7-b.

Let us denote by ϑ_L the momentum right before the reflection at $x = L$. Then the momentum ϑ jumps from ϑ_L to $-\vartheta_L$ so the arc in the phase space is chopped to have a flat part at $x = L$. As a consequence, the new quantization equation reads

$$2f\vartheta_L L + 2E(\vartheta_a - \vartheta_L) - 2\int_{\vartheta_L}^{\vartheta_a} dq\, \varepsilon(q|\Theta) = 2\pi f\,(n+1) + f\,\phi\left(\frac{\Theta}{2} - \vartheta_a, \frac{\Theta}{2} + \vartheta_a\right) + f\,\phi\left(\frac{\Theta}{2} - \vartheta_L, \frac{\Theta}{2} + \vartheta_L\right), \quad (4.31)$$

together with the conditions $\varepsilon(\vartheta_a|\Theta) = E$ and $\varepsilon(\vartheta_L|\Theta) = E - fL$.

We compare the predictions for the intrachain meson energies with spin $s = 0$ at $P = \Theta = 0$ (meson mass gaps) of the 2-kink effective equation (4.7) and those of the semiclassical quantization (4.30), (4.31) with exact diagonalization data of the ladder at $\Delta_{||} = 5$ in Fig. 4.8. The plot clearly shows that while the 2-kink approximation with hard-core kinks breaks down, the (finite volume) semiclassical approximation yields an excellent agreement with the exact diagonalization results. Thanks to the spin-dependent phase shift, this approximation also predicts the energy splitting for the case $s = 0$, which partially lifts the degeneracy of the spectrum (from four-fold to two-fold) in the thermodynamic limit and cannot be captured with the first approach. Remarkably, even though the semiclassical method is supposed to work well for high energy bound states with large quantum numbers, it gives accurate results even for the lowest lying mesons.

4.3 Composite excitations

We recall that in the regime $\Delta_{||} \gg 1$ and $\Delta_{||} \gtrsim \Delta_{\perp}$, the energy spectrum of the Hamiltonian (5.8) is organized in bands of states with a given number of kinks, as shown in Fig. 4.1. In the previous two sections, we developed an effective systematic description for the low lying 2-kink states. Here, we introduce a more heuristic treatment to grasp the nature of some of the higher excited states. We focus on the case of even L and zero magnetization in both chains, i.e. $M_1 = M_2 = 0$.

The first class of states lying above the 2-kink ones are obviously the four-kink states. For even L, the latter can either be a combination of two intrachain (Fig. 4.9-a) or of two

interchain mesons (Fig. 4.9-b). Notice that for odd L we instead have only combinations of one intrachain and one interchain meson, a situation that we do not describe here. In the zeroth order approximation in which we neglect the interaction between mesons, the energy levels of the four-kink states is just the sum of the dispersion relations obtained in the preceding sections for the single mesons, i.e.

$$E(n_1, n_2, p, P) = \frac{1}{2}\left[E_{n_1}\left(\frac{P}{2}+p\right) + E_{n_2}\left(\frac{P}{2}-p\right) + \{n_1 \leftrightarrow n_2\}\right], \tag{4.32}$$

where n_1 and n_2 collectively label the internal states of the mesons, $p = (p_1 - p_2)/2$ is the relative momentum and $P = p_1 + p_2$ is the total momentum of the mesons. The labels $n_{1,2}$ are assigned from the less energetic to the most energetic internal states at $P = 0$. Since we are treating the two mesons as non-interacting particles, we have some strong constraints on the allowed values of the relative momentum p. First, the finite-volume quantization of p is affected by the reduced effective volume where the kinks can move freely due to the constraint that they cannot overlap. Accordingly, the relative momentum is quantized as $p = m\pi/L_{\text{eff}}$ with m integer. The effective available volume is $L_{\text{eff}} = L - 2$ for two interchain mesons (two kinks on each chain) and $L_{\text{eff}} = L - 4$ for two intrachain mesons (the four kinks are all on the same chain). Moreover, since they cannot overlap, the states with $p = 0$ are forbidden. These two reasonable assumptions will be justified also a posteriori by the correct description of the relevant part of the energy spectrum.

The approximation of non-interacting mesons works for large enough $\Delta_\perp$ and in the limit $\Delta_{||} \gg 1$. Indeed, when $\Delta_\perp$ becomes too small, the internal oscillations of each meson become so wide that the 4-kink states cannot be interpreted as a composition of separate mesons. Furthermore, this approximation is not expected to be effective for large $n_{1,2}$ because higher meson states have a more extended wave function (as it can be immediately deduced by looking at the spreading of the Bessel functions with respect to their index).

We compare the spectra of the ladder and of the staggered XXZ chain in Figs. 4.10 and 4.11. In the former figure we report all states in the energy interval $E \in [4, 5]$ and identify some smaller windows (indicated by large rectangles) that are analyzed in detail in the latter figure. The first simple fact evident in both figures is that there are many more 4-kink states in the ladder than in the chain, reflecting the presence of interchain mesons which do not exist on the chain. Hence, for the 4-kink states, the mean-field treatment does not predict much.

We present a more quantitative analysis in Fig. 4.11. Here we zoom in the regions within the colored rectangles in Fig. 4.10. The spectrum in these windows is compared with the energy levels computed with Eq. (4.32). Notice that the red rectangle appears three times and the green one twice, where the green area is a further zoom of the red one. We make this choice because we plot the dispersion relation with different quantum numbers that cannot be put on the same graph in a clear manner. On top of each panel we report the quantum numbers corresponding to the spin and the internal energy levels of the mesons that are displayed in the plot.

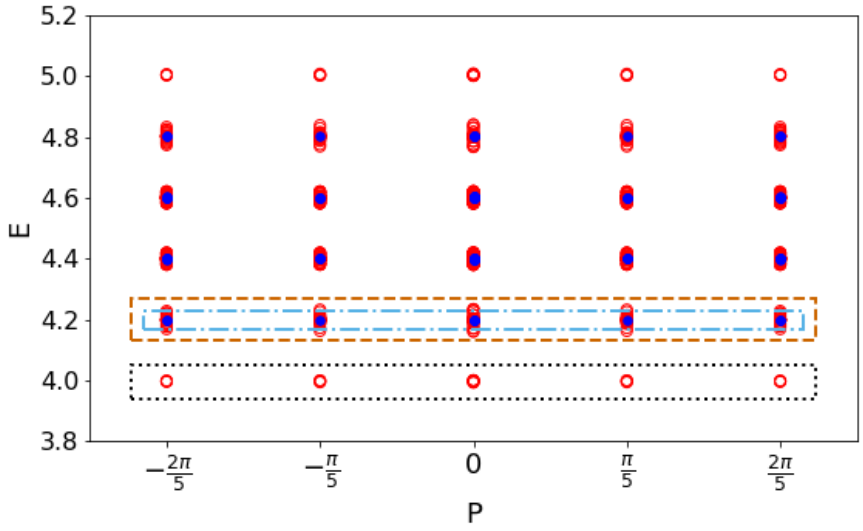

Figure 4.10: Spectrum of the ladder (red circles) and the staggered XXZ chain (blue dots) for energies in the interval $E \in [4, 5]$ where four-kink states lie for large $\Delta_{||}$. We report data for the zero magnetization sector in both chains $M_1 = M_2 = 0$. We work at $\Delta_\perp = 5$, $\Delta_{||} = 100$, and $L = 10$. The blue, red, and green rectangles are the regions that are magnified in Fig. 4.11.

Despite the roughness of the approximation, it is remarkable that Eq. (4.32) captures some features of the spectrum. For example, the four dispersions plotted in the frames (b) and (c) very neatly describe families of states that are well separated from each other. Also in panel (f), the intrachain states (that exist also for the staggered chain but with different momentum quantization, as it is clear from the fact that they alternate) are well captured by our approximation. Instead, resolving the states within the green frames in Figs. 4.11 is beyond the purpose of our approximation. It is a dense region where the separation of the states is comparable to higher perturbative orders in ϵ that are neglected in our description. On the other hand, all the states that are sufficiently isolated in the spectrum (on an energy scale of order ϵ), are well captured by this approximation. We remark that while, in virtue of confinement, the single-meson bands described in Sec. 4.1 remain discrete and well separated in energy when L goes to infinity, the two-meson bands become denser and fall in the continuum part of the spectrum.

4.4 A transition for the first excited states

We have already shown in Sec. 4.1 that, in the limit of large $\Delta_{||}$ and moderate $\Delta_\perp$, the low-lying excitations of a ladder with even L in the sector of zero magnetization are well captured by an effective model of a spin chain in staggered field; the lowest excitations are intrachain ('Type 1') mesons, confined bound states of kinks. Decreasing the value

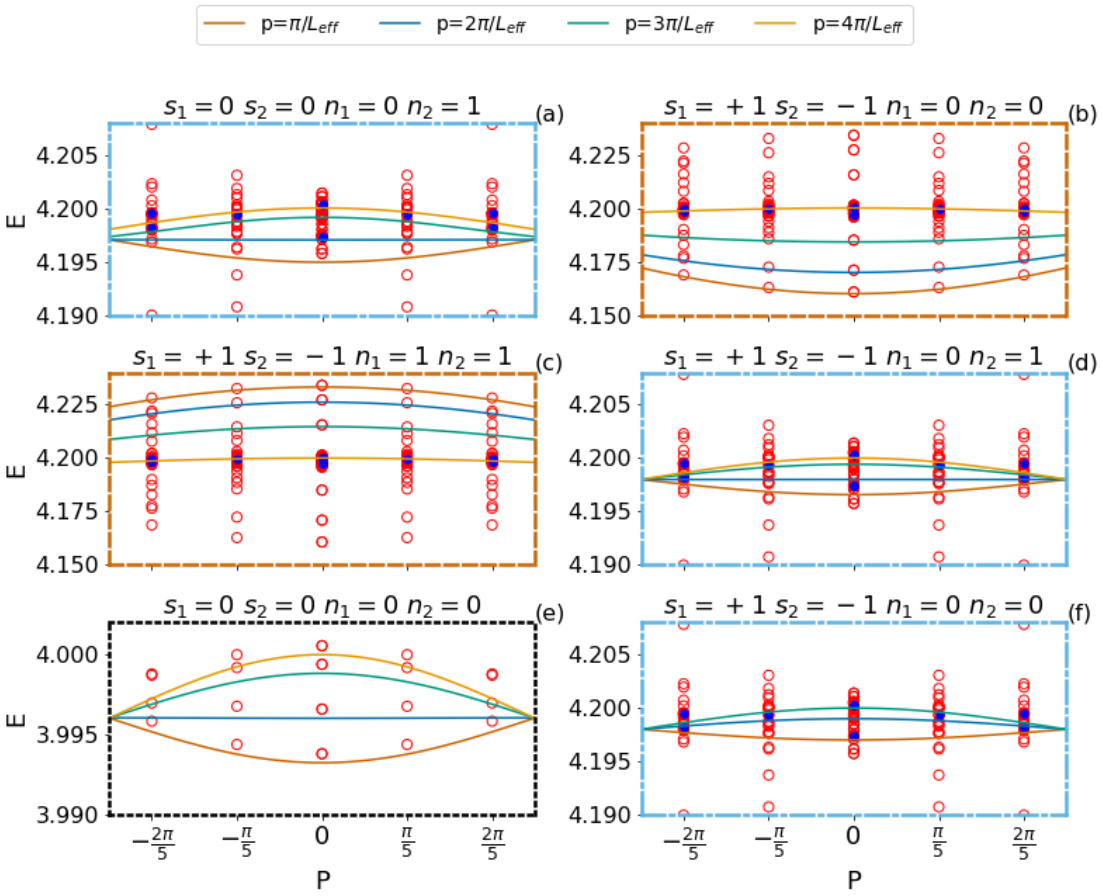

Figure 4.11: Zooms of the marked areas in Fig. 4.10. The different symbols are the numerical data. The frame colors (red, green, and blue) correspond to the colors of the rectangles in Fig. 4.10. The green area is a further zoom of the red one. The continuous lines correspond to the noninteracting two-meson approximation (4.32) for interchain 'Type 2' (a,b,c,d,e) and intrachain 'Type1' (f) mesons. Each panel shows these approximate energy levels for fixed values of the spins and internal labels of the mesons corresponding to the quantum numbers reported above each panel. The different lines correspond to different values of the relative momentum p reported in the legend on top of the plot. $L_{\rm eff} = L - 2$ or $L_{\rm eff} = L - 4$ for interchain and intrachain mesons, respectively.

of $\Delta_{||}$, we observe that the nature of the first excited states changes qualitatively. This can be understood from a simple classical argument. The lowest lying intrachain meson (Fig. 4.12-a) has energy $E_{\rm intra} \simeq 2 + 4\Delta_{\perp}/\Delta_{||}$, while the least energetic interchain meson (Fig. 4.12-b) has $E_{\rm inter} \simeq 2$. Despite being less energetic, we cannot find this interchain excitation in the low-energy spectrum in the zero-magnetization sector, because, as discussed in Sec. 4.1.2, a single meson of this type carries magnetizations $s_{1,2} = \pm 1/2$

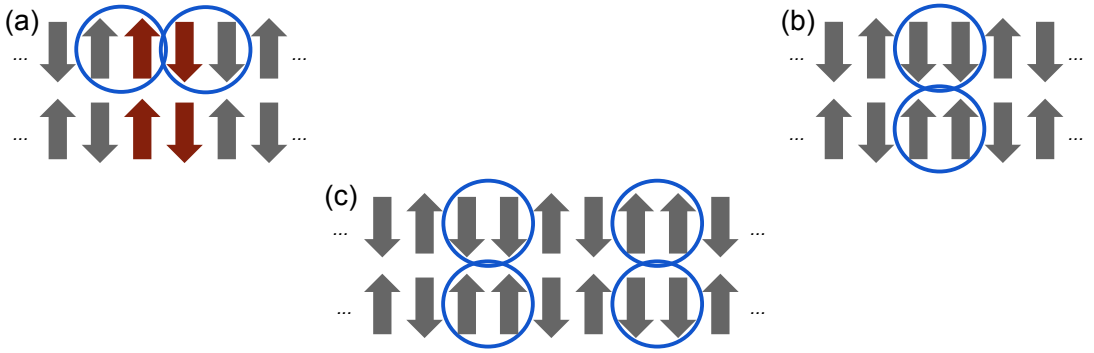

Figure 4.12: Schematic pictures of the lowest-lying (a) intrachain and (b) interchain mesons. For $\Delta_\perp \lesssim 2\Delta_{||}$ the intrachain meson (a) represents the first excited state. In the regime $\Delta_\perp \gtrsim 2\Delta_{||}$ the low-energy sector is made of states with pairs of interchain mesons (c).

on the two chains and it is only compatible with odd L. However, when $\Delta_{||}$ is sufficiently small, the energy of the first intrachain meson becomes so large that it is comparable with the energy $2E_{\text{inter}} \simeq 4$ of a two-meson state of 'Type 2' (Fig. 4.12-c). This happens when $2E_{\text{inter}} = E_{\text{intra}}$, i.e. for $\Delta_{||} \sim 2\Delta_\perp$.

We illustrate this transition in Fig. 4.13 for $\Delta_{||} = 100$ and $\Delta_{||} = 5$ by showing all the numerically calculated zero-momentum eigenstates in the relevant energy range as functions of $\Delta_\perp$, for $\Delta_\perp$ around $\Delta_{||}/2$. The blue dots represent the 'Type 1' intrachain single meson states of the staggered XXZ chain. As expected, when $\Delta_\perp \approx \Delta_{||}/2$, the two kinds of states become nearly degenerate. At this point, the single meson and the 2-meson states hybridize. As the interchain two-meson states are invariant under the chain swap transformation, they only hybridize with intrachain meson states that are also invariant under chain swapping.

The observed phenomenon is not a quantum phase transition as it does not concern the ground state but the excited states. As a matter of fact, similar "transitions" take place already for smaller $\Delta_\perp$ at higher energy levels involving states with more kinks and mesons. Nonetheless, the change in the nature of the low-energy sector has important physical consequences. It can be observed, for example, in the non-equilibrium dynamics after a quantum quench, where the spreading of correlations is determined by the quasiparticle excitations. While in the absence of confinement excitations can propagate freely, in the presence of an attractive potential quasiparticles get confined into mesons and hence the spreading of entanglement and correlations is suppressed. This is what we expect when $\Delta_{||} \gtrsim 2\Delta_\perp$. Conversely, for $\Delta_{||} \lesssim 2\Delta_\perp$, the low-energy sector is a continuum of two-meson states: while kinks are still confined in mesons, the spreading of correlation is not suppressed because the pairs of mesons are free to move with opposite momenta. Therefore, in a quench a dramatic difference between the two regimes is likely to emerge.

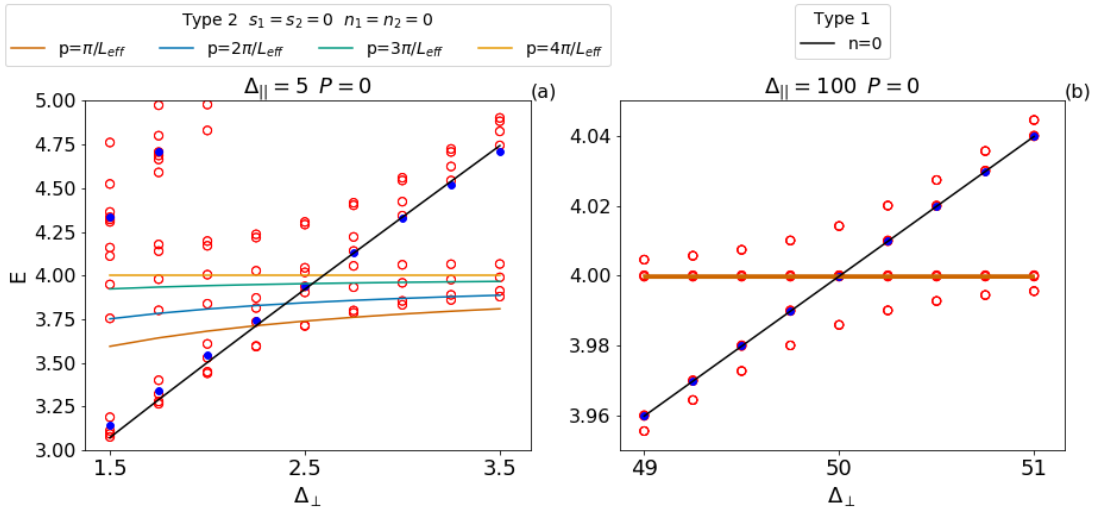

Figure 4.13: Spectrum on the ladder (red circles) and on the staggered chain (blue dots) around the level crossing near $\Delta_{||} \approx 2\Delta_\perp$. The violet solid line shows the numerical prediction for the first level of intrachain mesons computed using Eq. (4.7). The other lines are extracted from Eq. (4.32) for two interchain mesons with $s_1 = s_2 = 0$ and $n_1 = n_2 = 0$ like in Fig. 4.11-e. The corresponding quantum numbers are shown in the legend.

4.5 Quench dynamics

In this section we report the results of numerical simulations for the time evolution after a quench obtained by using the infinite volume Time Evolving Block Decimation (iTEBD) algorithm [186]. The system is prepared in a product state of the two chains with one chain in the Néel $|\Psi_1\rangle = |\uparrow\downarrow\uparrow\downarrow\ldots\rangle$ and the other in the anti-Néel state $|\Psi_2\rangle = |\downarrow\uparrow\downarrow\uparrow\ldots\rangle$, i.e., in the ground state of the model in the limit $\Delta_{||} \to \infty$, $\Delta_\perp \geq 0$. Thereafter, the quench is realised by letting the system evolve under the Hamiltonian with finite $\Delta_{||} > 1$ and $\Delta_\perp > 0$ (i.e., by suddenly changing both the inter-chain and intra-chain couplings). The real time evolution after the quench is performed with a Trotter step $\delta t = 10^{-2}$. The bond dimension χ is set to 512. We checked the stability of the numerical simulations with respect to changes in χ and δt.

In the following, we investigate the effects of confinement (i.e., of a non-zero the inter-chain coupling $\Delta_\perp$) on the evolution of the entanglement entropy, the one-point function of the order parameter, and its equal time two-point correlation function. We will take advantage of the results and the methodologies presented in previous part of this chapter in order to interpret the dynamics.

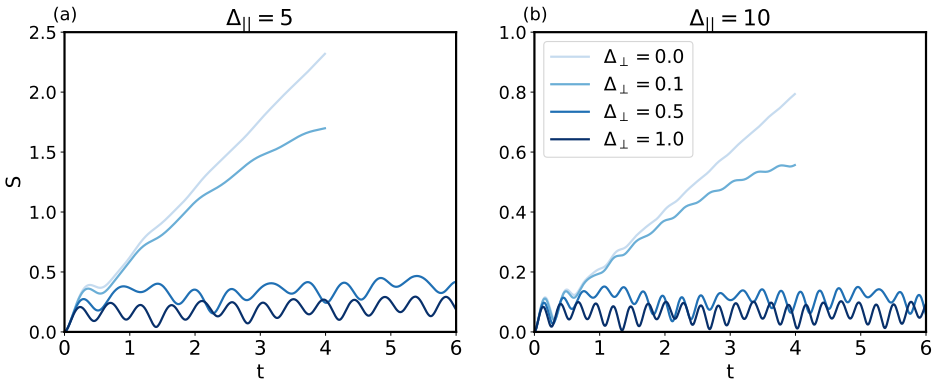

Figure 4.14: Time evolution of the half chain entanglement entropy (4.33) after a quench from a state with one chain in the Néel state and the other in the anti-Néel state, i.e. the ground state for $\Delta_{||} = \infty$. The post-quench Hamiltonian has (a) $\Delta_{||} = 5$ and (b) $\Delta_{||} = 10$. The different shades of blue correspond to different values of $\Delta_\perp$, as shown in the legend. Note that the linear growth for $\Delta_\perp = 0$ is turned into an oscillatory behaviour in the presence of confinement.

4.5.1 Entanglement entropy

Here we focus on the half chain entanglement entropy, measured through the von Neumann entropy

$$S(t) = -\mathrm{Tr}\left[\rho_\mathrm{h}(t) \log \rho_\mathrm{h}(t)\right], \tag{4.33}$$

of the half chain reduced density matrix ρ_h obtained from the full density matrix $\rho(t) = |\psi(t)\rangle \langle\psi(t)|$ by tracing out the degrees of freedom of the other half chain. The results are shown in Fig. 4.14.

When the inter-chain coupling $\Delta_\perp$ is zero, the well-known linear growth of the half-chain entanglement entropy is observed. This limiting case is essentially a standard quench in the two independent XXZ chains in the anti-ferromagnetic region, whose dynamics have been thoroughly studied in Refs. [44, 45]. For the sake of readability, the main concepts that have been already discussed in Sec. 2.3 are here recalled. The dynamics of an integrable model, due to the infinite number of conserved quantities, may be understood in terms of quasiparticles complemented by the knowledge of the stationary states from Bethe Ansatz. Here the quasiparticle picture [41] provides an intuitive yet quantitative framework for quenches: the pre-quench state acts as a source of pairs of quasiparticles with opposite momenta. The pair of particles are entangled and, by traveling ballistically, they spread quantum correlations through the system. In an interacting integrable model there are different quasiparticle species, each one contributes to $S(t)$ proportionally to the number of quasiparticles shared between the two subsystems. Therefore, $S(t)$ is the sum over the independent contributions of each quasiparticle species. Since they travel ballistically, a pair of quasiparticles can spread correlations over a distance that grows linearly in time, leading to a linear growth $S(t) \propto$

t. We observe this linear behaviour in Fig. 4.14 (top lines) for two different post-quench values of $\Delta_{||}$.

We remember that a linear entanglement growth is generically expected also in non-integrable models, despite the lack of well defined quasiparticles (see for instance [68, 73]). In the model we are studying, the presence of the inter-chain Ising coupling $\Delta_\perp$ does break integrability. However, once the inter-chain coupling $\Delta_\perp$ is introduced, the growth of the entanglement entropy is significantly slowed down with the appearance of large oscillations that are stable within the observation time. The behaviour of the von Neumann entropy showed in Fig. 4.14, similarly to the Ising case discussed in Sec. 3.1.1, can be explained with the following argument. In contrast to kinks that can only appear in pairs, the excitations produced in the quench for $\Delta_\perp \neq 0$ mainly consist of single mesons: these mesons have zero momentum, and they contribute to entanglement through the mechanism of Bloch oscillations resulting in the periodic variation of the size of the meson ("breathing"). Correlations can only spread roughly up to the distance set by the largest separation of the two kinks forming the meson. Therefore, the entanglement entropy grows linearly only for a limited time (independent of system size) and then bounce back oscillating. The frequencies of the oscillations are expected to correspond to the meson masses and their differences (we do not report here the analysis of the frequencies of these oscillations because it is identical to the one below in Fig. 4.17 for the one-point function).

Above the two-particle threshold, a small fraction of mesons are expected to be produced in pairs with non-zero and opposite momenta. These pairs of mesons can propagate freely, leading eventually to a linear growth of entanglement entropy at long times. However, the production of meson pairs is very small for the small quenches we studied and its effect on the entanglement is too slow to be detected numerically. However, as shown in Sec. 4.5.2, some effects of the production of pairs of mesons are detectable in the time evolution of two-point correlations.

4.5.2 Light cones in the two-point function

In this section we investigate the effect of the inter-chain coupling $\Delta_\perp$ on the spreading of two-point correlation functions. We focus on the equal time connected two-point function of the local staggered magnetisation, i.e. $C_s(\ell) = \langle(-1)^\ell S^z_{i,\alpha} S^z_{i+\ell,\alpha}\rangle_c = \langle(-1)^\ell S^z_{i,\alpha} S^z_{i+\ell,\alpha}\rangle - \langle(-1)^i S^z_{i,\alpha}\rangle^2$. Because of the Lieb–Robinson bound [187], there is a maximal velocity of propagation $v_{\max}$. Consequently, at time t all the connected correlators vanish at distances $\ell \geq v_{\max} t$.

Let us start by considering $\Delta_\perp = 0$. Like the other observables, the behaviour of two-point connected correlators can be understood in terms of the quasiparticle description of the XXZ chain, as introduced in Sec. 2.1: the quasiparticles travel ballistically with velocities $v(\lambda) < v_{\max}$, leading to the light cones observed in Fig. 4.15-(a),(f). The velocity $v_{\max}$ is related to the maximum speed of excitations built on top of the stationary state, see Ref. [188]. As pointed out in Sec. 3.1.1 for the Ising chain, in the presence of confinement the quasiparticles (i.e. the kinks) cannot move anymore ballistically and

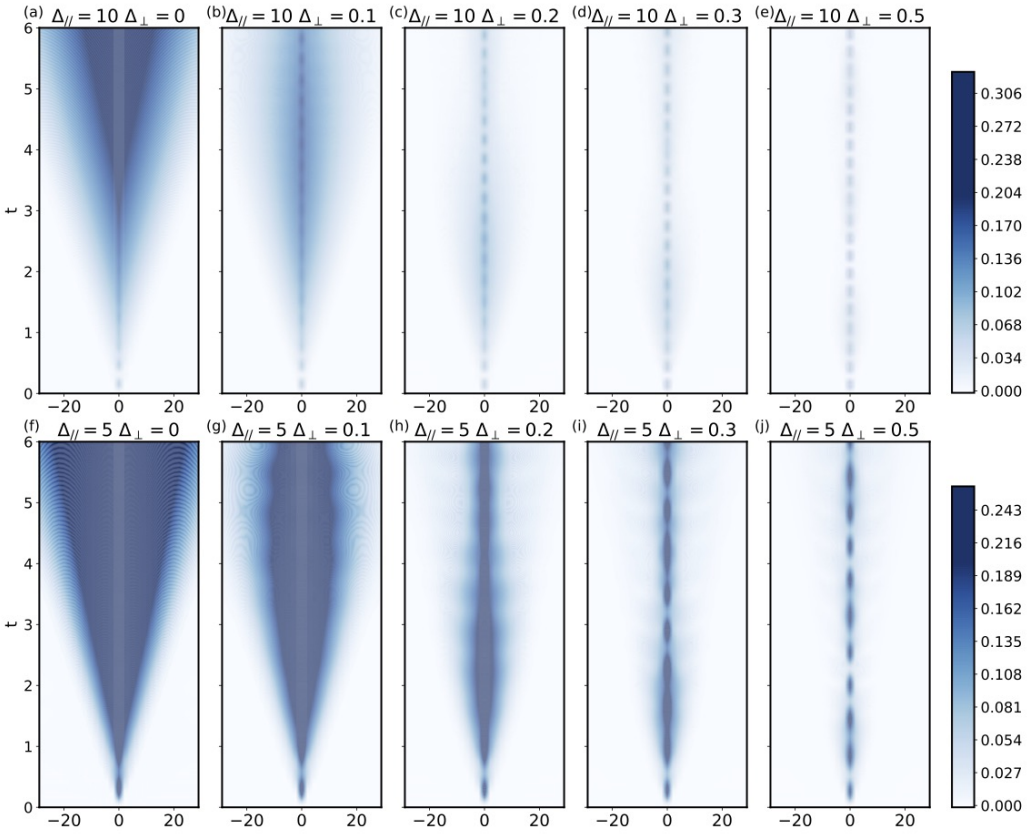

Figure 4.15: Space-time plots of the time evolution of the single-chain connected staggered two-point function $C_s(\ell) = \langle (-1)^\ell S^z_{i,1} S^z_{i+\ell,1} \rangle_c$ after a quench. The initial state has one chain in a Néel state and the other in anti-Néel state. The final Hamiltonian has $\Delta_{||} = 10$ (top row) and $\Delta_{||} = 5$ (bottom row) with $\Delta_\perp = 0, 0.1, 0.2, 0.3, 0.5$. The standard ballistic light cones for $\Delta_\perp = 0$ (a,f) are strongly suppressed by turning on a non zero $\Delta_\perp$.

they show a characteristic breathing shape with an amplitude of the oscillation related to width of the zero-momentum meson. This transition from the ballistic growth to the confined regime is reported in Fig. 4.15 showing clearly that when $\Delta_\perp \neq 0$, the quasiparticles are confined into mesons. As a consequence the correlations are strongly suppressed and they are considerably non-zero only in the region where the mesons extend, see again Fig. 4.15.

Till now the form of the correlations does not show qualitative differences compared to the confining Ising chain reported in Ref. [22]. In order to observe the effect of the presence of different species of mesons, in Fig. 4.16 we re-plot some of the density plots of Fig. 4.15 on a different scale (with respect to Fig. 4.15, being the figure symmetric,

we consider the half plots with $\ell > 0$). In this way we can appreciate the small signal due to the production of pairs of mesons of opposite momenta: weak components of the signal, previously hidden, become visible showing several light cones. The signal clearly shows that these secondary light cones are a consequence of propagating mesons: as these are heavier particles compared to the kinks, they move at a lower velocity. To understand quantitatively their structure, we compare them with the maximal speed of propagation of the different mesons and of the kinks. These velocities are extracted with the help of the approximate techniques developed in the previous sections for the derivation of the dispersion relations ω_m, where m runs on the kind, spin and parity of the meson. The maximal speed of propagation of the a given meson is then obtained as $v_{\max}^{(m)} = \max\left(\frac{\mathrm{d}\omega_m(p)}{\mathrm{d}p}, p \in [-\pi/2, \pi/2]\right)$ (the derivative of the dispersion relations is computed numerically with a proper discretisation of the center of mass momentum P). In the figure we report all the speeds of propagation of the lightest (i.e. fastest) meson for each type (details in the caption). We compare them to the kink speed, expected to describe the $\Delta_\perp = 0$ case (and obtained from Eq. (4.18)).

Let us now finally discuss the results are shown in Fig. 4.16 for two values of the intra-chain coupling $\Delta_{||} = 5, 10$ and inter-chain coupling $\Delta_\perp = 0.2, 0.3, 0.5$. Right after the quench, the evolution of the light cone is always compatible with the one predicted from the free kink dispersion relation. Once the two kinks are created with opposite momenta, they do not immediately feel the confining potential and they experience an almost-free initial propagation. Subsequently, they bounce back, and the signal deviates significantly from the free slope. The main signal is associated to zero momentum intra-chain mesons which corresponds to the breathing observed in Fig. 4.15. Indeed, similarly to kinks in a single chain, inter-chain mesons are topological excitations and can be created by local operations only in pairs. Outside of the first meson breathing zone, secondary light cones develop which are visible on the scale of Fig. 4.16. In all the cases that are shown, the first secondary cone (the darkest one in the figure) has a slope which is compatible with the maximal speed of propagation associated intra-chain mesons. For this speed, we report the derivation with the two approaches of Sec. 4.1.1 and 4.2 (red and yellow curves) although the differences are very small and the numerical data (accessible in the observation time) are unable to discriminate among the two. The other secondary light cones (the one in lightest blue) are expected to be explained in terms of lighter mesons. In particular, some signal from pairs of propagating inter-chain mesons are also expected to be present. Though our results are not conclusive, in (c),(d),(e) and (f) a weaker signal is deviating from the main secondary lightcone and it is roughly compatible with the slopes we predicted for the inter-chain mesons.

4.5.3 Time evolution of the staggered magnetisation and masses of the mesons

After the entanglement entropy and correlation functions, we turn to the study of 1-point functions of the staggered magnetisation of a single chain $m_s = \langle(-1)^i S^z_{i,1}\rangle$, which is a local order parameter of the model in the anti-ferromagnetic region. The numerical

results are presented in Fig. 4.17 for the post-quench couplings $\Delta_{||} = 10$ in (a),(b) and (c); $\Delta_{||} = 5$ in (d) (e) and (f). For $\Delta_{\perp} = 0$ (i.e. quenching $\Delta_{||}$ in an XXZ chain), the anti-ferromagnetic order is expected to relax exponentially [16, 17, 189], as showed by the solid grey line in the (a) and (d) panels. For $\Delta_{\perp} \neq 0$, instead, the staggered magnetisation is trapped in stable oscillations, exactly like the local magnetization in the Ising chain in Fig. 3.1 (b) (see also [81, 82]). In the right hand side of Fig. 4.17, (i.e. (b),(c),(e) and (f)), we show the results in the frequency domain after performing a Fourier analysis of the signals obtained for $\Delta_{\perp} = 0.3, 0.5$. The dominant oscillation frequencies appear as well-defined peaks.

In order to show that the peaks correspond to the mass gaps of the mesons, we display the results of two different approximations for the masses discussed in Sec. 4.1.1 and .4.2. We compare the numerical predictions with both BS and Bessel approaches. To analyse the data we recall that the Hamiltonian in Eq. (5.8) preserves the parity of the state and the total spin along each chain. Consequently, the post-quench state is constrained to share those properties with the initial state. In our case, the latter has one chain in Néel and the other in an anti-Néel state, so the relevant mesons must have total spin $s = 0$ along each chain of the ladder and must have positive parity. In the right hand side panels of Fig. 4.17 we report theoretical predictions for the $s = 0$ intra-chain mesons. It is evident that the Bessel approach roughly captures the position of the peaks, but quantitatively is a bit off. This is not surprising since the very same conclusion was also drawn for the equilibrium data in Sec. 4.2. However, for those states for which we found a solution of the BS quantisation condition, we have an an extremely precise description of the peaks. Furthermore, the improvement of accuracy of the BS approach compared to Bessel is more appreciable for $\Delta_{||} = 5$ than for $\Delta_{||} = 10$. This is explained as the more the longitudinal coupling $\Delta_{||}$ is decreased the more the corrections due to the non-trivial two-kink scattering, (and the precise form of their dispersion relation) become relevant. We finally mention that a similar spectroscopy analysis can be done also for the entanglement entropy, but the obtained results are completely equivalent to those for the staggered magnetisation and so are not reported here.

4.6 Conclusions

In this chapter we performed two tasks: we systematically characterized the spectrum of the Heisenberg-Ising ladder with Hamiltonian (5.8) as well as its quench dynamics in the region of parameters presenting confinement, i.e. in the ordered antiferromagnetic phase of the two chains for $\Delta_{||} > 1$. Our first main result is that we find two kinds of quasi-particle excitations, which we dub intrachain and interchain mesons, that correspond to bound states of kinks within the same chain or between different ones, respectively. Very importantly, intrachain mesons can be also obtained by means of a mean field treatment mapping the Hamiltonian to a staggered chain. Interchain mesons are genuine features of the ladder and they were not known by other means. They are expected to be a common characteristic of ladders with Ising-like rung interactions that lead to confinement. In fact, their existence is a consequence of the spontaneous braking of one symmetry.

Hence, there are two equivalent true vacua and neutral mesons can interpolate between the same or different ones. One-particle intrachain (interchain) mesons are present only when the total ladder has even (odd) length. Conversely, two-particle states of interchain mesons are present also for even L. We quantitatively characterized the meson states. First, in the limit of large $\Delta_{||}$ we find the one-particle meson dispersion by projecting on the two-kink subspace. We release the condition of very large anisotropy exploiting semiclassical quantization. We also describe the four-kink (two mesons) states in the dilute approximation, i.e. treating the two mesons as non-interacting particles. Finally, we point out an interesting transition for the first excited state in even length ladders. At fixed $\Delta_{||}$, the first excited state is a one-particle intrachain meson state for small $\Delta_{\perp}$, but as the latter is increased it crosses over to a two interchain meson state.

We then showed that the through spectroscopy of the order parameter evolution (and also of the entanglement entropy not reported here) the masses of the $s = 0$ intra-chain mesons can be accessed, see Fig. 4.17. A very remarkable finding is that while the two-point function are strongly suppressed because of confinement (see Fig. 4.15), there are feeble secondary light cones (see Fig. 4.16) in which the existence of all types of mesons can be observed as a consequence of a very small production of pairs of mesons with opposite momenta.

We finally discuss some lines of future research. A first question concerns the physics of more than two coupled chains (e.g. three for a start). Are there new kinds of bound states that can emerge from the enlarged local Hilbert space? It would be interesting to investigate also the case of anisotropic Heisenberg-like (XXZ) interchain coupling which is more relevant to experiments on spin-chain compounds. Another intriguing question is whether confinement may also give rise to non-thermal states in the middle of the many-body spectrum, in analogy to the recently introduced many-body scars [19, 190], or incidentally, it is possible that the hybridisation with multiparticle states could eventually allow the system to thermalise, but on extremely long times scales. It would be very interesting to find even approximate methods to argue whether this is the case. However, in this context, it might be necessary to go beyond the low-density approximation, a goal which is very hard to achieve with standard techniques.

4.A Kink scattering phases

In this Appendix, we collect the exact expressions for the scattering phases which are used in the semiclassical quantization equations in Sec. 4.2.

In the gapped antiferromagnetic phase of the XXZ chain, in the absence of external magnetic fields, the elementary excitations are spin-1/2 topological excitations, $|K_{\alpha\beta}(\vartheta)\rangle_s$ interpolating between the two degenerate vacua α, β. Their momenta and z spin component are labeled by ϑ and s, respectively. Their dispersion relation can be

parameterized by the so-called rapidity variable $\lambda \in [\pi/2, \pi/2]$ as [191]

$$\vartheta(\lambda) = \frac{\pi}{2} - \mathrm{am}(2K\lambda/\pi, k)\,, \tag{4.34a}$$

$$\omega(\lambda) = \frac{2K}{\pi}\sinh(\gamma)\mathrm{dn}(2K\lambda/\pi, k)\,, \tag{4.34b}$$

where $K = K(k)$ is the complete elliptic integral of modulus k with

$$\frac{K(\sqrt{1-k^2})}{K(k)} = \frac{\gamma}{\pi}\,, \tag{4.35}$$

and $\mathrm{am}(x,k)$ and $\mathrm{dn}(x,k)$ are the Jacobi amplitude and delta amplitude. The parameterization (4.34) is equivalent to the form (4.18) in the main text.

These particles are interacting which is manifested in their nontrivial scattering properties. In the total spin zero channel, corresponding to the scattering of a $s = 1/2$ and a $s = -1/2$ particle, the scattering matrix is diagonalized by the combinations

$$|K_{\alpha\beta}(\vartheta_1)K_{\beta\alpha}(\vartheta_2)\rangle_{\pm} = \frac{1}{\sqrt{2}}\left(|K_{\alpha\beta}(\vartheta_1)K_{\beta\alpha}(\vartheta_2)\rangle_{\frac{1}{2},-\frac{1}{2}} \pm |K_{\alpha\beta}(\vartheta_1)K_{\beta\alpha}(\vartheta_2)\rangle_{-\frac{1}{2},\frac{1}{2}}\right). \tag{4.36}$$

The scattering phases are defined as

$$|K_{\alpha\beta}(\vartheta_1)K_{\beta\alpha}(\vartheta_2)\rangle_{ss} = w_0(\vartheta_1,\vartheta_2)|K_{\alpha\beta}(\vartheta_2)K_{\beta\alpha}(\vartheta_1)\rangle_{ss}\,, \tag{4.37a}$$

$$|K_{\alpha\beta}(\vartheta_1)K_{\beta\alpha}(\vartheta_2)\rangle_{\pm} = w_{\pm}(\vartheta_1,\vartheta_2)|K_{\alpha\beta}(\vartheta_2)K_{\beta\alpha}(\vartheta_1)\rangle_{\pm}\,. \tag{4.37b}$$

They were obtained in Ref. [185] using Bethe ansatz with the result

$$w(\vartheta_1,\vartheta_2) = -e^{i\phi_\eta(\vartheta_1,\vartheta_2)}\,, \tag{4.38}$$

$$\phi_\eta(\vartheta_1,\vartheta_2) = \Phi_\eta(\lambda_1-\lambda_2)\,, \tag{4.39}$$

$$\Phi_0(\lambda) = -\lambda - \sum_{n=1}^{\infty}\frac{e^{-n\gamma}\sin(2\lambda n)}{n\cosh(n\gamma)}\,, \tag{4.40}$$

$$\Phi_{\pm}(\lambda) = \Phi_0(\lambda) + \chi_{\pm}(\lambda)\,, \tag{4.41}$$

$$\chi_{+}(\lambda) = -i\ln\left(-\frac{\sin[(\lambda-i\gamma)/2]}{\sin[(\lambda-i\gamma)/2]}\right), \tag{4.42}$$

$$\chi_{-}(\lambda) = -i\ln\left(\frac{\cos[(\lambda-i\gamma)/2]}{\cos[(\lambda-i\gamma)/2]}\right) \tag{4.43}$$

with $\vartheta_k = \vartheta(\lambda_k)$ as in Eq. (4.34a). The scattering phases $\phi_\eta(\vartheta_1,\vartheta_2)$ are the ones that appear in Eqs. (4.30) and (4.31) with η chosen according to the the total spin of the particles.

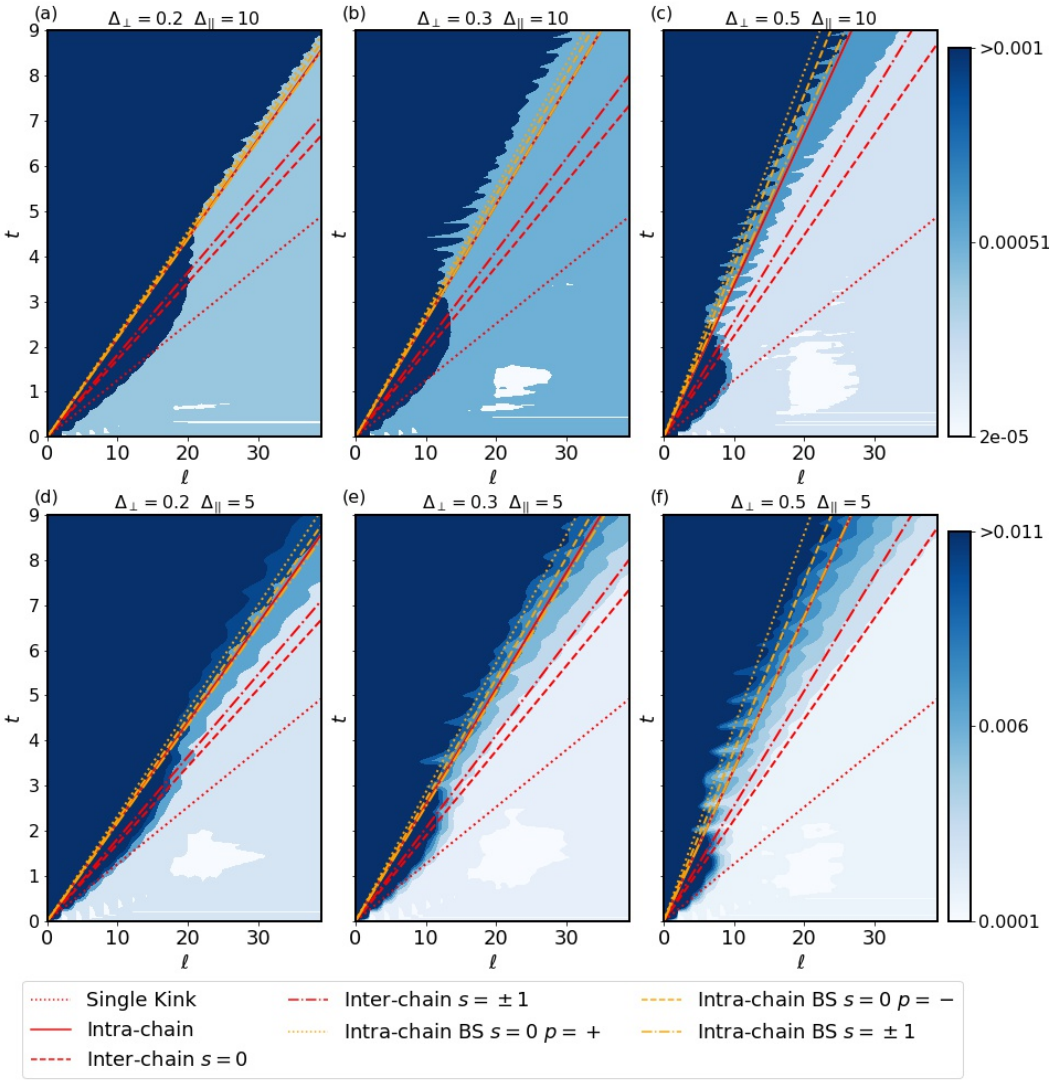

Figure 4.16: Density plot for time evolution of the single-chain connected staggered two-point function $C_s(\ell) = \langle (-1)^\ell S^z_{i,1} S^z_{i+\ell,1} \rangle_c$ after a quench. The initial state has one chain in the Néel state and the other in the anti-Néel state. The post-quench Hamiltonian has $\Delta_{||} = 10$ with $\Delta_\perp = 0, 0.1, 0.5$ in (a), (b) and (c) respectively and $\Delta_{||} = 5$ with $\Delta_\perp = 0, 0.1, 0.5$ in (d) , (e) and (f). The scale in the colour plot is tuned in such a way that a weaker signal compared to Fig. 4.15 is visible. The straight lines correspond to the maximal speed of propagation of the different particles. The red dotted line corresponds to the kink propagation speed, obtained from Eq. (4.18). The other lines describe the propagation of the two kinds of mesons. All yellow lines are BS predictions (Eq. 4.30) while the red ones are Bessel (Eq. 4.7). In the Bessel approximation, all intra-chain mesons have the same maximal speed (that is why we report a single curve). These are resolved by the BS approach showing two lines, one for spin $s = 0$ and negative parity the other for spin $s = \pm 1$. Inter-chain mesons are instead found only in the Bessel approximation.

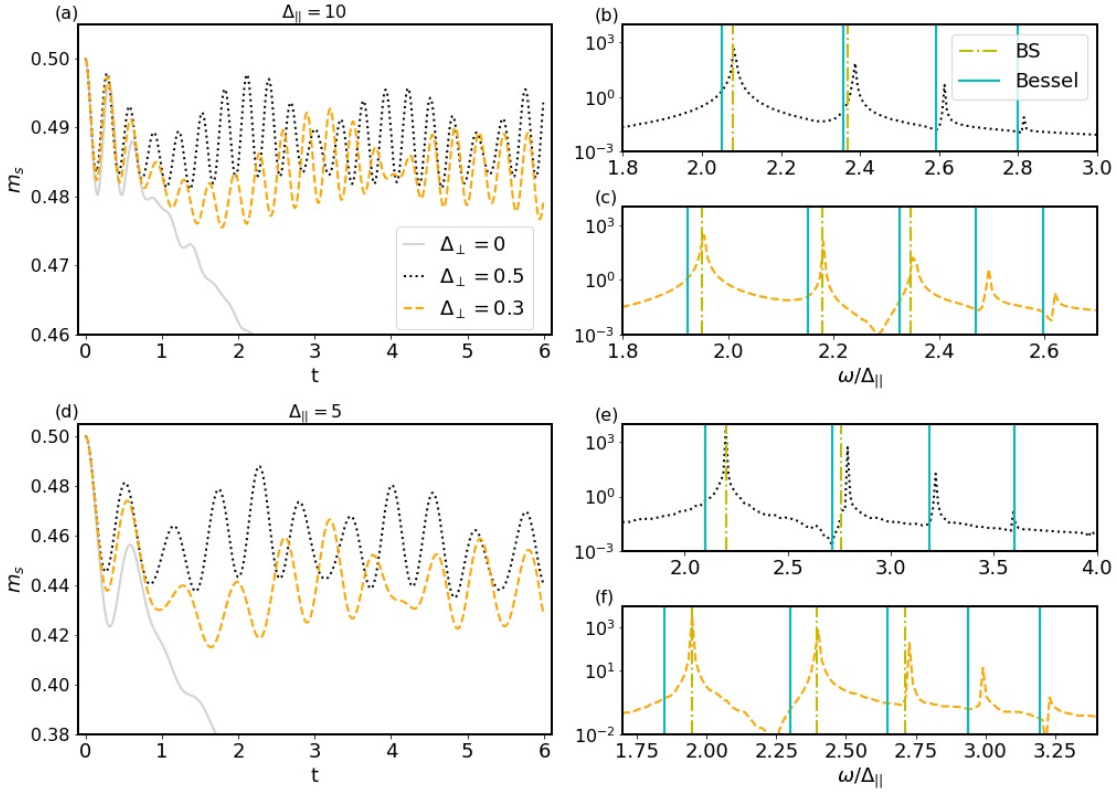

Figure 4.17: Time evolution of the staggered magnetisation after a quench from a state with one chain in a Néel state and the other in Anti-Néel state. The final Hamiltonian has $\Delta_{||} = 10$ (a) and $\Delta_{||} = 5$ (d) with $\Delta_\perp = 0.5$ (dotted) or $\Delta_\perp = 0.3$ (dashed). The light grey line is the quench to $\Delta_\perp = 0$. (b) and (c) represent the Fourier analysis relative to $\Delta_{||} = 10$ for $\Delta_\perp = 0.5$ and $\Delta_\perp = 0.3$ respectively. Likewise, (e) and (f) show the Fourier analysis relative to $\Delta_{||} = 5$. In (b) (c) (e) and (f) the peaks are compared with the prediction extracted from the semi-classical approximation (BS) (dot-dashed lines) and the exact diagonalisation of the effective two-body Hamiltonian (Bessel) (straight lines).

Chapter 5

False Vacuum Decay in spin chains

The false vacuum decay has been a central theme in physics for half a century with applications to cosmology and to the theory of fundamental interactions. This fascinating phenomenon is even more intriguing when combined with the confinement of elementary particles. Due to the astronomical time scales involved, the research has so far focused on theoretical aspects of this decay. The possibility that our universe, as it cooled down, may have settled into a metastable state (false vacuum) that may eventually decay was proposed by Coleman in 1977 and has been since then one of the most popularized ideas of physical cosmology [192, 193, 194, 195]. The decay would happen through bubble nucleation, i.e. the formation of bubbles of true vacuum that rapidly expand: the probability for this process to occur is extremely small, and studying this phenomenon is notoriously challenging due to its intrinsic non-perturbative character.

In this chapter, we propose to study the decay of the false vacuum in quantum spin models using simulations of real-time dynamics after a quantum quench.

5.1 False vacuum decay

To illustrate the phenomenon of false vacuum decay, we recall again the quantum Ising chain in transverse and longitudinal fields, our prototypical model for confinement. For the sake of readability, here the main points of the dissertation performed in Sec. 3.1.1 are renewed. The Hamiltonian of the model reads

$$H(h_x, h_z) = -\sum_i \left(\sigma_i^z \sigma_{i+1}^z + h_x \sigma_i^x + h_z \sigma_i^z\right) , \tag{5.1}$$

where σ_i^α are Pauli operators, and the amplitudes h_x and h_z are the transverse and longitudinal field, respectively.

For $h_z = 0$ the model has a $\mathbb{Z}_2$ symmetry that is spontaneously broken for $|h_x| < 1$ (ferromagnetic phase). In this phase there are two ground states characterized by opposite magnetizations $\langle \sigma_i^z \rangle = \pm M$, with $M = (1 - h_x^2)^{1/8}$ [196]. The model is diagonalized

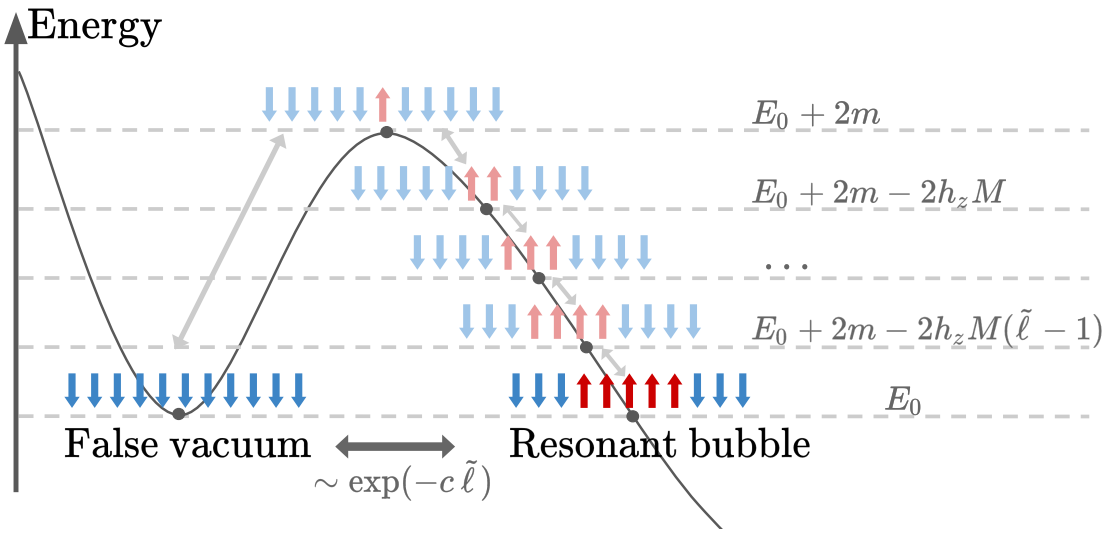

Figure 5.1: *Illustration of bubble formation* (false vacuum is in blue, true vacuum in red). The process that leads to the resonant bubble goes through $O(\tilde{\ell})$ off-resonant states: a small bubble is (virtually) created and expanded until it reaches the resonant size $\tilde{\ell}$. As a consequence, the matrix element that drives the false vacuum decay is exponentially small in $\tilde{\ell} \propto h_z^{-1}$.

with a mapping to free fermions: the corresponding excitations in the ferromagnetic phase are kinks that interpolate between domains with opposite magnetization [197]. The kinks can propagate freely and have dispersion relation

$$\omega(\theta) = 2\left(1 - 2h_x \cos\theta + h_x^2\right)^{1/2}. \tag{5.2}$$

For a longitudinal field $h_z \neq 0$, the $\mathbb{Z}_2$ symmetry is explicitly broken and the degeneracy between the two ground states is split by an extensive quantity $\sim 2h_z MN$, where N is the number of sites in the chain: the state with magnetization aligned with the external field (the *true vacuum*) is the ground state of the model, while the one with opposite magnetization (the *false vacuum*) is a metastable state.

The false vacuum is at high energy, so it can resonantly decay into the continuum of multi-meson states. While this decay is a very complicated process, the basic mechanism can be understood as the formation of bubbles of true vacuum in the system. Creating a bubble of size ℓ requires the energy given by the masses of the two kinks lowered by $2h_z M\ell$. When this energy becomes zero, the bubble is resonantly excited. This bubble can then further decay through other resonant processes. However, for h_z sufficiently small, the phenomenon of bubble formation is very slow. This slowness can be understood by the following simple heuristic argument. A resonant bubble of size $\tilde{\ell}$ results from the frequent creation of a small bubble (of size of order 1) that then should expand until it reaches the resonant size $\tilde{\ell} \gg 1$ (see Fig. 5.1). This expansion is a high-order process in the perturbation theory in h_z and, as a consequence, the matrix element for

exciting the resonant bubble is exponentially small in $\tilde{\ell} \propto h_z^{-1}$.

The decay of the metastable false vacuum in the Ising chain has been studied in Ref. [126], where the following expression of the decay rate per site was obtained [1]:

$$\gamma = \frac{\pi}{9} h_z M \exp\left(-\frac{q}{h_z}\right) \tag{5.3}$$

with $q = |f(-i \ln h_x)|/M$ and $f(\theta) = 2\int_0^\theta \omega(\alpha)\, \mathrm{d}\alpha$. Note that q and M only depend on h_x. This rate γ can be interpreted as the number of resonant bubbles that are created per unit time divided by the number of sites. In agreement with the argument explained above, the decay is non-perturbative in the longitudinal field, with an exponential dependence on h_z^{-1}. While the exponential dependence in Eq.(5.3) is a well established result coming from different rigorous computations, the prefactor originates from approximated procedures and might be subject to future improvements.

We note that an analogous mechanism drives the phenomenon known as *string breaking*. String breaking is typically understood as the saturation of the effective interaction between two static charges (or kinks, in this case) at large distance, due to the screening effects of other charges: in other words, the string that extends between the two static charges is broken by the creation of dynamical charges. In the model we are studying, the string corresponds to a false vacuum domain and the string breaking effect corresponds to the formation of a bubble in the domain. The dynamics of string breaking has been studied in this model, in other spin chains, and lattice gauge theories [198, 162, 199, 163, 200, 201, 202, 203, 204, 205, 104, 161, 208, 152, 154, 151], and similar expressions for the decay rate were found.

5.2 Quench protocol and methods

Our goal here is to show that a window of Hamiltonian parameters of the Ising spin chain (h_x, h_z) exists such that the false vacuum decay can be observed through numerical simulations of the non-equilibrium dynamics after a quantum quench. The quench protocol is the following: i) we prepare the system in the ferromagnetic state with all the spins in the $\sigma_i^z = 1$ direction; ii) we evolve the system in imaginary time with the Hamiltonian $H(h_x, -h_z)$ using infinite volume time evolving block decimation (iTEBD) until we achieve a good convergence to the ground state; iii) we quench $-h_z \to h_z$ and evolve in real time. Using this protocol, we are able to prepare the false vacuum of $H(h_x, h_z)$ and study its evolution in real time using iTEBD. The state preparation ii) is obtained using a Trotter step $\delta t = 10^{-3}$, and the imaginary time evolution stops when the relative change of the energy density is smaller than 10^{-16}. The real time evolution after the quench iii) is performed with a Trotter step $\delta t = 10^{-2}$. The bond dimension χ is set to 512. We checked the stability of the numerical simulations with respect to changes in χ and δt.

[1] In Ref. [126], the rate γ contains an oscillatory term $g(h_z)$: we work here in the approximation $g(h_z) \simeq 1$, which is justified for h_z sufficiently far from 1.

We stress that in our quench protocol the false vacuum decay drives the system toward a thermal state, that has a finite energy density with respect to the true vacuum. Only in the limit $h_z \to 0$ this state tends to the true vacuum.

5.3 Time scales

Before embarking on the analysis of the numerical data, we should have a clear picture of all the time scales entering in the quench dynamics of our model. Starting from the false vacuum, the first process happening is the creation of off-resonant bubbles. During this (relatively) short-time transient, say up to time $\tau_{\rm r}$, the system remains effectively frozen in the false vacuum until the resonant bubbles start being produced. However, here we are not interested in this transient but only in the growth of the resonant bubbles, because this is the process that leads to the false vacuum decay described by the rate (5.3). For the accurate measurement of this rate, we need a clear separation of this time scale from the successive ones. Indeed, at very late time, when most of the false vacuum decayed, since the system is at finite energy density, it starts thermalizing through the propagating states that originate from the decay of the resonant bubbles: the late time dynamics is governed by the thermal state corresponding to the energy of the pre-quench state (only for very small h_z this is close to zero temperature, i.e. the true vacuum). We denote with τ_D the time scale for the onset of thermalization; unfortunately, we do not know how to estimate $\tau_{\rm D}$, but its determination lies beyond the scope of this thesis. For the sake of our numerical investigation, the prediction extracted from Eq.(5.3) must be tested under the assumption of a clean separation of time scales, i.e. $\tau_r \ll \gamma^{-1} \ll \tau_D$. For the Hamiltonian (5.1), such separation of time scales is guaranteed in the regime $h_z \ll 1$ and h_x not too close to 1. The requirement $h_z \ll 1$ is obvious, since as h_z grows all the above time scales $\tau_r, \gamma^{-1}, \tau_D$ become of order one and there cannot be any separation. Similarly, if h_x gets too close to 1, the masses of the kinks become very small and the whole dynamics become faster. In light of such considerations, even though the $h_x \to 1$ case has been studied in [127] and an expression for the decay rate similar to Eq. 5.3 was found (see [206] and [207] for a more comprehensive discussion), the analysis of the $h_x \to 1$ case is left for future works. However, when the fields are reduced, the time scale γ^{-1} soon becomes extremely large (which is the reason why false vacuum decay is generically an elusive phenomenon, see also [158]). Thus the main difficulty of the numerical analysis is to find a window of the Hamiltonian parameters such that there is an optimal balance between a reasonable separation of times scales (to have a time range in which Eq. (5.3) describes something) and its numerical accessibility. We found that such balance is obtained for rather small h_z (of the order of 10^{-2}), but with h_x relatively large $h_x \sim [0.7, 0.9]$: a smaller h_x makes the decay time (γ^{-1}) too long and a larger h_z destroys completely the time-scale separation.

5.4 Results

To estimate the decay rate, we analyze the following two observables

$$F(t) = \frac{\langle \sigma_i^z(t)\rangle + \langle \sigma_i^z(0)\rangle}{2\langle \sigma_i^z(0)\rangle}, \tag{5.4}$$

$$G(t) = 1 - ||\rho(t) - \rho(0)||_1, \tag{5.5}$$

where $\rho(t)$ is the two-site density matrix at time t and $||\rho(t)-\rho(0)||_1$ is the trace distance between the two density matrices. Both quantities can be easily computed in iTEBD, and satisfy $F(0) = G(0) = 1$, while they vanish in the true vacuum. The time evolution of $F(t)$ is fully encoded in the magnetization and, consequently, is expected to decay with a rate

$$\gamma_F \simeq \gamma\tilde{\ell} = \frac{f(\pi)}{18} \exp\left(-\frac{q}{h_z}\right), \tag{5.6}$$

where the factor $\tilde{\ell}$ is fixed through the characteristic length associated to the resonant bubble $\frac{f(\pi)}{2h_z M\pi}$ (see Ref. [126]). Note that for small h_z, this rate is much larger than γ, so the time scale needed to observe the decay in our simulation is significantly reduced.

As an illustrative example for the determination of the decay rates of F and G, in Fig. 5.2 we report their evolution at fixed $h_x = 0.8$ and different values of h_z on a semi-log scale. It is evident that after a short transient, all the data show a distinct exponential decay (linear behavior on semi-log scale).

For all the considered values of h_x and h_z, we performed an exponential fit $O(t) = A_O e^{-\gamma_O t}$, with $O = F, G$. The fit is done in a time range $t_0 < t < t_1$ and then we check the stability of the fit for small variations of t_0, t_1. The resulting decay rates $\gamma_{F,G}$ are plotted in Fig. 5.3-a,b,c as functions of h_z^{-1} again on semi-log scale. The exponential dependence on $1/h_z$, expected from Eq. (5.6), is very clear in the data. We fitted these rates with

$$\gamma_O = k_O e^{-q_O/h_z}, \qquad O = F, G. \tag{5.7}$$

In Fig. 5.3-d we report the obtained coefficients q_F, q_G: they are compatible with each other and they both agree very well with the theoretical prediction $q = |f(-i \ln h_x)|/M$ in the full range of h_x considered. The prefactors k_F and k_G in Eq. (5.7) turn out to be different from what predicted by Eq. (5.6) (the data in Fig. 5.3-a,b,c are shifted compared to the dashed line). However, this shift is not surprising at all because we know that (i) the prefactor depends on the specific observable (e.g., compare Eqs. (5.3) and (5.6)), (ii) we expect it to be more affected by the approximations done in the derivation of Eq. (5.6).

5.5 XXZ ladder

To show the general validity of our analysis, we also consider a second model for confinement. We recall here its Hamiltonian and its main features, which have been extensively

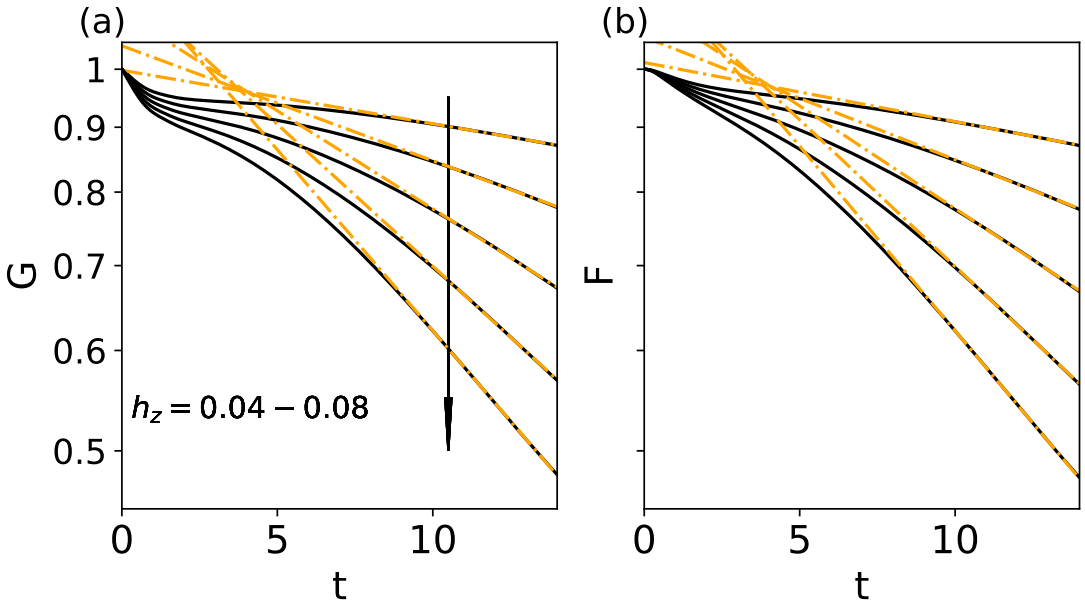

Figure 5.2: *False vacuum decay in the quantum Ising chain.* The time evolution of $F(t)$ and $G(t)$, in Eqs. (5.4) and (5.5), is shown for $h_x = 0.8$ and different values of h_z after the quench $-h_z \to h_z$. The dot-dashed lines are the exponential fits in the decay region performed to extract the decay rates γ_F and γ_G.

addressed in in Chap. 4:

$$H(\Delta_{||}, \Delta_{\perp}) = \frac{1}{2} \sum_{j=1}^{L} \sum_{\alpha=1,2} \Big[\sigma^x_{j,\alpha} \sigma^x_{j+1,\alpha} + \sigma^y_{j,\alpha} \sigma^y_{j+1,\alpha} + \Delta_{||} \sigma^z_{j,\alpha} \sigma^z_{j+1,\alpha} \Big] + \Delta_{\perp} \sum_{j=1}^{L} \sigma^z_{j,2} \sigma^z_{j,1} \tag{5.8}$$

i.e. two XXZ spin-1/2 chains coupled along the longitudinal direction through an anisotropic Ising-like interaction. Compared to the Ising spin chain (5.1), the model possesses two interesting features. The first is that in the absence of the confining interaction (h_z and $\Delta_{\perp}$), the Ising spin chain becomes a free model, while the decoupled XXZ chains constitute an interacting (integrable) spin model. The second one is that confinement is induced by the internal interaction between the chains, a built-in mechanism, instead of an external field (and this is more similar to what happens for quarks). We work in the gapped anti-ferromagnetic phase, i.e. $\Delta_{||} \in (1, +\infty)$ where the model for $\Delta_{\perp} = 0$ has four degenerate antiferromagnetic ground states. The confining potential explicitly breaks the original $\mathbb{Z}_2 \times \mathbb{Z}_2$ symmetry to a single $\mathbb{Z}_2$: the four degenerate ground states at $\Delta_{\perp} = 0$ are split in two doublets separated by an energy of the order $\Delta_{\perp} L$. The two lowest states (the true vacua) are now the stable ground states, while

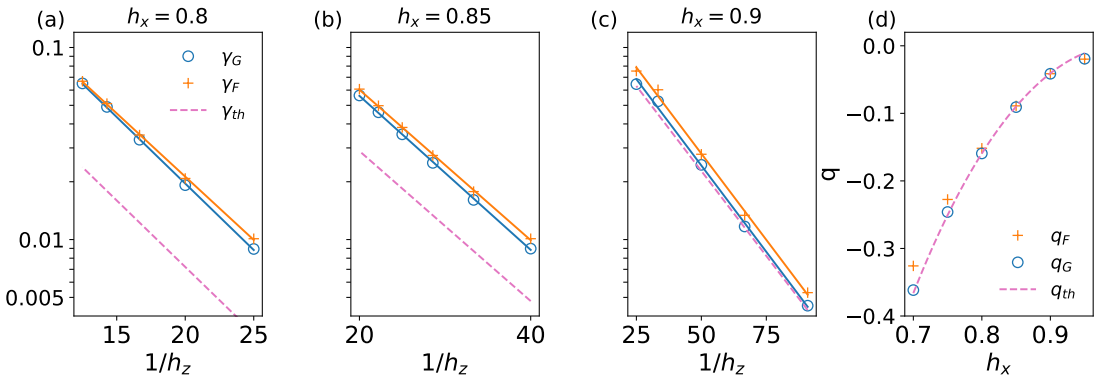

Figure 5.3: *Decay rates in the quantum Ising chain.* In panels (a),(b),(c) we show the decay rates γ_F, γ_G, obtained from the fits of $F(t)$, $G(t)$ as in Fig. 5.2. The continuous lines are the fits of the exponential dependence of the rates in $1/h_z$. The dashed line represents the theoretical prediction (5.6). From the fits the coefficients q_F and q_G are extrapolated and showed against the theoretical value $q_{\rm th} = |f(-i \ln h_x)|/M$ (dashed line) in panel (d).

the other two (the false vacua) are metastable states at high energy and can decay in the continuum of the many-body spectrum.

In analogy with the Ising model, we prepare the false vacuum as the ground state at $-\Delta_\perp$ and then we quench $-\Delta_\perp \to \Delta_\perp$. For several values of the interactions $\Delta_\perp$ and $\Delta_{||}$, we extract the decay rates $\gamma_{F,G}$ for $F(t), G(t)$ (here F in Eq. (5.4) is built with the staggered magnetization and G in Eq. (5.5) with the reduced density matrix of two adjacent rungs). In Fig. 5.4, a) and b), we show the time evolution of G after the quench for two values of $\Delta_{||}$. Even though we do not have analytic predictions for this ladder, we expect that the underlying mechanism of the false vacuum decay is the same so we can fit the decay rate with Eq. (5.7) with the replacement $h_z \to \Delta_\perp$. The test of this scaling for γ_G is presented in Fig. 5.4 c) and d), showing a perfect agreement. The quality of the fit for γ_F is very similar, although in Fig. 5.4 we only report the final values for γ_F and not the data for $F(t)$.

5.6 Conclusions

In chapter we provided robust numerical evidence that for two one-dimensional spin models featuring confinement of elementary excitations it is possible to identify a range of physical parameters such that the rate of false vacuum decay is accessible in measurable time scales. The quench protocol that we described here is amenable to quantum simulation, for example with trapped ions or Rydberg atoms (both can simulate a system with confinement). For the false vacuum preparation, the imaginary time evolution used in the numerics can be replaced by an adiabatic preparation.

We conclude by briefly discussing how the the trapped-ion quench experiment of Ref.

[110] (for the observation of domain wall confinement in real time) can be adjusted to measure the false vacuum decay. In this experiment, the ion dynamics is well captured by a long-range quantum Ising model in which the $\mathbb{Z}_2$ symmetry is spontaneously (and not explicitly) broken. Hence, there are two degenerate real vacua and no false one. In order to get a phenomenology similar to our setup it is sufficient to slightly tilt the effective magnetic field (that in Ref. [110] is in the z direction) via a Rabi rotation, see the review [209]. This tilting provides a small component of the magnetic field along the x axis that breaks the degeneracy of the two vacua with a real and a false one. Then the preparation of the system in the false vacuum and the following quench are done with the very same techniques exploited already in Ref. [110]. Finally one- and two-point functions of the spin can be measured, as already done in Ref. [110], giving access to $F(t)$ and $G(t)$ in Eqs. (5.4) and (5.5).

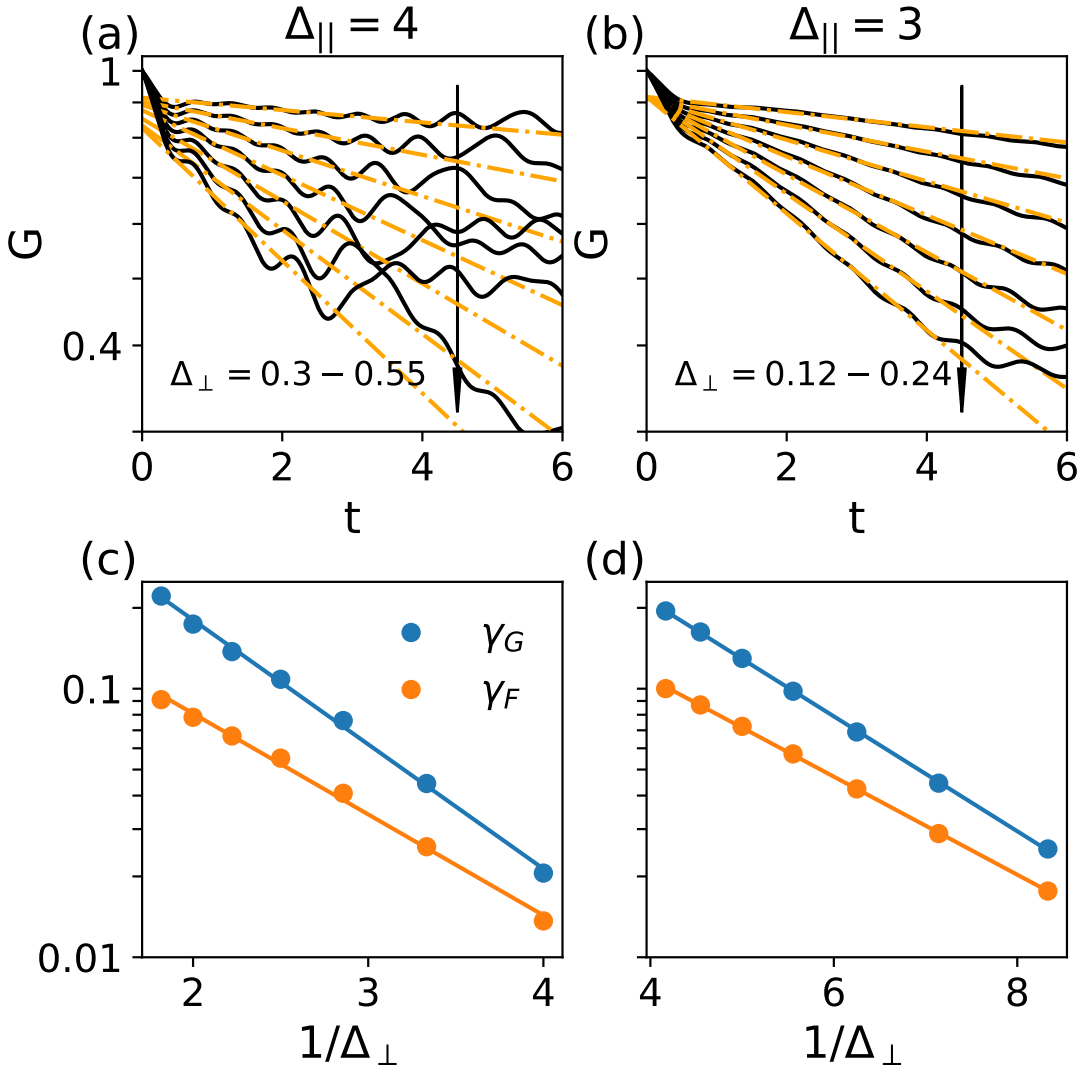

Figure 5.4: *False vacuum decay for the XXZ ladder. Panels (a) and (b):* Time evolution of G in Eq. (5.5) after a quench $\Delta_\perp \to -\Delta_\perp$ with $\Delta_{||} = 4$ (a) and $\Delta_{||} = 3$ (b) with different values of $\Delta_\perp$. In (a) $\Delta_\perp = 0.25, 0.3, 0.35, 0.4, 0.45, 0.5, 0.55$ while $\Delta_\perp = 0.12, 0.14, 0.16, 0.18, 020, 0.22, 0.24$ in (b). The arrows indicate the growing direction of $\Delta_\perp$. *Panels (c) and (d):* decay rates extracted from the fits in (a) and (b), respectively, on semi-logarithmic scale. The continuous lines are fits of the decay rates performed according to Eq. (5.7)

Part II

Entanglement dynamics in integrable systems

Chapter 6

Overview

In Sec. 2.3 we introduced how the quasiparticle picture, originally developed in the CFT framework, represents a powerful tool to capture the entanglement evolution after the application of a quench protocol. This intuitive theoretical setting has then been extended to quantitatively characterise the dynamics of the standard measure of bipartite entanglement — the von Neumann entanglement entropy or simply entanglement entropy [210, 211, 29] – in many different kinds of systems with stable quasiparticles, such as free [41, 43, 45] and interacting integrable models [44, 45] in a large variety of physical contexts. We remind how, within this picture, one postulates that a homogeneous quench produces an extensive number of quasiparticle excitations, which are responsible for propagating the entanglement throughout the system. However, an important assumption is that such quasiparticles are only produced in pairs, which is known to be true for a class of low-entangled initial states. Though not obvious a priori, we show in Chap 7 how the same approach is fruitfully adapted to describe the entanglement dynamics of Thermofield Double States in integrable spin chains and field theories. Indeed, for a natural choice of the Hamiltonian eigenbasis, the TFD evolution may be interpreted as a quantum quench from an initial state which is low-entangled in the real-space representation and displays a simple quasiparticle structure. Based on a semi-classical picture analogous to the one developed for standard quantum quenches and introduced in Sec. 2.3, we conjecture a formula for the entanglement dynamics, which is valid for both discrete and continuous integrable field theories, and expected to be exact in the scaling limit of large space and time scales. We test our conjecture in two prototypical examples of integrable spin chains, where numerical tests are possible. First, in the XY-model, we compare our predictions with exact results obtained by mapping the system to free fermions, finding excellent agreement. Second, we test our conjecture in the interacting XXZ Heisenberg model, against numerical iTEBD calculations. For the latter, we generally find good agreement, although, for some range of the system parameters and within the accessible simulation times, some small discrepancies are visible, which we attribute to finite-time effects.

The quasiparticle picture description of the entanglement growth has recently been challenged by studies on the dynamics of Rényi entropies. Indeed, given the unques-

tionable success of the quasiparticle picture in quantitatively capturing the evolution of the entanglement entropy for integrable systems, it is very natural to assume that the same picture also describes the evolution of Rényi entropies. Several basics facts support this scenario: (i) it holds for free systems [41, 35, 43], (ii) there is no clear qualitative difference between the numerically computed Rényi entropies and the entanglement entropy [212, 213], (iii) in chaotic systems the membrane picture describes both von Neumann and Rényi entropies [73, 74]. The extension of the quasiparticle picture to describe Rényi entropies in the presence of interactions, however, proved to be very challenging [212, 213, 214, 62]. In fact, Ref. [64] showed that no consistent quasiparticle picture can describe the evolution of Rényi entropies in an integrable quantum cellular automaton. A possible explanation of these findings is that, although the quasiparticle picture describes the evolution of entanglement entropy also in the presence of interactions, it fails to describe the growth of Rényi entropies. This would highlight a very unexpected fundamental difference between the two quantities, which complements the accounts of sub-linear growth of Rényi entropies in certain systems with diffusive conservation laws [215, 216, 217].

Motivated by these thoughts, in Chap. 8 it is showed how the slope of the Rényi entropies can be predicted by means of a spacetime duality transformation. In essence, it is argued that the slope coincides with the stationary density of entropy of the model obtained by exchanging the roles of space and time. Therefore, very surprisingly, the slope of the entanglement is expressed as an equilibrium quantity. This observation is exploited to find an explicit exact formula for the slope of Rényi entropies in all integrable models treatable by thermodynamic Bethe ansatz and evolving from integrable initial states. Interestingly, this formula can be understood in terms of a quasiparticle picture only in the von Neumann limit.

Chapter 7

Entanglement dynamics of thermofield double states in integrable models

In this chapter are going to study the entanglement dynamics of thermofield double (TFD) states in integrable spin chains and quantum field theories.

The *thermofield double* (TFD) state is defined on two identical copies (or replicas) of a quantum many-body system or field theory, usually denoted by "left" and "right", and takes the form

$$|\mathrm{TFD}\rangle = \frac{1}{\sqrt{Z_\beta}} \sum_n e^{-\beta E_n/2} |E_n\rangle_L |E_n\rangle_R \,, \tag{7.1}$$

where E_n and $|E_n\rangle$ are the eigenvalues and eigenstates of the Hamiltonian H, β is the inverse temperature, while Z_β is the canonical partition function. The dynamics is given by evolving the left and right copies up to time t_L and t_R, respectively, i.e.

$$|\mathrm{TFD}\,(t_L, t_R)\rangle = \frac{1}{\sqrt{Z_\beta}} \sum_n e^{-\beta E_n/2} e^{-iE_n(t_L+t_R)} |E_n\rangle_L |E_n\rangle_R \,. \tag{7.2}$$

The TFD state plays a very important role in the context of the AdS/CFT correspondence [218], as it was proposed to be dual to an eternal black hole [219, 220]. It provides a controlled setup to investigate various aspects of black-hole physics, and to explore new ideas inspired by quantum information theory, including questions related to quantum scrambling and chaos [221, 222, 223] and quantum complexity [224, 225, 226, 227, 228, 229, 230, 231, 232, 233, 234].

The TFD state is also interesting and appears naturally in the study of non-relativistic quantum many-body systems, since it provides a *purification* of the thermal Gibbs state. For instance, it is at the basis of several efficient tensor-network algorithms to compute thermal expectation values [235].

When $t_L = t_R$, the TFD dynamics can be thought of as a quantum quench [16, 17], where the system is initialized in the state (7.1) and subsequently evolved by the

Hamiltonian

$$H = H_L + H_R = H \otimes \mathbb{1} + \mathbb{1} \otimes H \,. \tag{7.3}$$

Given a subsystem made of two identical regions in the left and right spaces, a natural question pertains to the growth of the corresponding von Neumann entanglement entropy. On the one hand, this quantity is of interest in the context of holography [236] and has already been investigated in many works, see for instance [236, 237, 238, 239, 231, 232, 240]. On the other hand, when $\beta = 0$, it coincides with the entanglement entropy of the evolution operator [241], which features in several recently-proposed measures of quantum scrambling and chaos for non-relativistic many-body systems, see e.g. [242, 243, 244, 245, 246, 247, 248].

In general, it is very challenging to compute the growth of the TFD entanglement entropy after a quench: for short-range models, an exact calculation has been carried out only for non-interacting bosonic quantum field theories [231]. Interestingly, the quasiparticle picture we presented in Sec. 2.3 was recently tested to high precision against exact calculations for the TFD entanglement dynamics in non-interacting bosonic theories [231]. This result is nontrivial: if we interpret the TFD state as the initial state for a quench problem in a two-replica space, it is not obvious, *a priori*, that the picture developed for standard quenches should apply, as the setting is very different. Motivated by the results of [231], here we address a very simple question: *can we extend the quasiparticle picture for the TFD entanglement dynamics to more general integrable models*? We stress that this question is interesting per se and goes beyond its possible connections to holography, as it also applies, for instance, to non-conformal theories and lattice models.

In order to tackle this problem, it is first important to realize that the definition of the TFD state is not unique whenever the Hamiltonian displays spectral degeneracy: different choices for the energy eigenbasis lead to states with distinct physical properties. In this chapter, we will focus on one natural basis for which the TFD state is initially low-entangled in the real space representation. This is a natural choice to make contact with the standard theory of quantum quenches where initial states are typically assumed to be low-entangled, which we remember represents a fundamental starting point for the quasiparticle picture to be applied.

With this definition, we show that the TFD dynamics can be interpreted as a quench where only pairs of quasiparticles are created, and conjecture a generalization of the standard picture for the dynamics of bipartite entanglement entropy. We test our conjecture in two prototypical examples of integrable spin chains. First, in the XY-model, we compare our predictions with exact results obtained by mapping the system to free fermions. Second, in the interacting XXZ Heisenberg model, we test our conjecture against numerical iTEBD calculations.

The rest of this work is organized as follows. In Sec. 7.1 we introduce the TFD state and discuss the choice of the Hamiltonian eigenbasis of interest in this work. We then review the quasiparticle picture for standard quenches, and present its generalization to the case of the TFD dynamics. In Sec. 7.2 we study the case of non-interacting spin chains focusing on the XY model. By mapping the system to free fermions, we obtain an

exact result for the TFD entanglement evolution, which allows us to perform a strict test of the quasiparticle picture. Next, Sec. 8.4.4 is devoted to the analysis of the interacting XXZ Heisenberg chain, where we compare our analytic predictions against numerical iTEBD calculations. Finally, we report our conclusions in Sec. 7.4.

7.1 The TFD state and the quasiparticle picture

7.1.1 The TFD state and the Hamiltonian eigenbasis

Let us begin by defining more precisely the quench protocol. For concreteness, we focus on a 1D lattice model, with Hamiltonian H and associated Hilbert space

$$\mathcal{H} = h_1 \otimes \ldots \otimes h_N \,, \tag{7.4}$$

where $h_j \simeq \mathbb{C}^d$, while N is the system size. Following our introductory discussion, we take two copies of the system, left (L) and right (R), so that the total Hilbert space is $\mathcal{K} = \mathcal{H}^L \otimes \mathcal{H}^R$. In the following, we will also denote by $h_j^{L/R}$ the left and right local Hilbert spaces. We study the quench protocol in which the system is initialized in the TFD state (7.1) and left to evolve according to the Hamiltonian (7.3), so that the state at time $t/2$ after the quench is

$$|\mathrm{TFD}\,(t)\rangle = \frac{1}{\sqrt{Z_\beta}} \sum_n e^{-\beta E_n/2} e^{-iE_n t} \, |E_n\rangle_L \, |E_n\rangle_R \,. \tag{7.5}$$

In the case the model displays spectral degeneracy, the state (7.5) strongly depends on the choice of the Hamiltonian eigenbasis, which we thus need to specify in order to uniquely define the quench protocol. This choice is guided by the notion of locality that we set in the two-replica space: Interpreting the doubled Hilbert space as a lattice with local site $k_j = h_j^L \otimes h_j^R$, we require that the TFD state (7.1) is a low entangled state in this lattice. This choice is very natural, and allows us to make direct contact with the theory of quantum quenches, where initial states are typically assumed to be low entangled.

Let us show that there always exists a Hamiltonian eigenbasis for which the TFD state at $\beta = 0$ is a *product state* in the doubled lattice $\mathcal{K}$. Denoting by $\{|\alpha\rangle_j\}_{\alpha=1}^d$ a basis for h_j, we introduce the following maximally entangled state between $\mathcal{H}^L$ and $\mathcal{H}^R$

$$|\mathcal{I}\rangle = \frac{1}{\sqrt{d^N}} \sum_{\{\alpha_n\}} |\alpha_1, \ldots, \alpha_N\rangle \otimes |\alpha_1, \ldots, \alpha_N\rangle \in \mathcal{K} \,. \tag{7.6}$$

Importantly, $|\mathcal{I}\rangle$ can be written as a product state in $\mathcal{K}$, namely

$$|\mathcal{I}\rangle = \bigotimes_{k=1}^N \left(\frac{1}{\sqrt{d}} \sum_{\alpha=1}^d |\alpha\rangle_k^L \otimes |\alpha\rangle_k^R \right) . \tag{7.7}$$

For the models considered in this work, it is easy to check that one can choose a local basis $\{|\alpha\rangle\}_{\alpha=1}^{d}$ such that

$$\overline{\langle\alpha_1,\ldots,\alpha_N|H|\alpha_1,\ldots,\alpha_N\rangle} = \langle\alpha_1,\ldots,\alpha_N|H|\alpha_1,\ldots,\alpha_N\rangle \ , \tag{7.8}$$

where $\overline{(\cdot)}$ denotes complex conjugation (which is a basis-dependent operation). It follows that there exists a Hamiltonian eigenbasis $\{|E_n\rangle\}_n$ which satisfies

$$\overline{\langle\alpha_1,\ldots,\alpha_N|E_n\rangle} = \langle\alpha_1,\ldots,\alpha_N|E_n\rangle \ . \tag{7.9}$$

Therefore, denoting by $\mathcal{N}$ the matrix which implements the change of basis from $\{|\{\alpha_n\}\rangle\}$ to $\{|E_n\rangle\}$, we obtain that $\langle\{k\}|\mathcal{N}|\{j\}\rangle = \overline{\langle\{k\}|\mathcal{N}|\{j\}\rangle}$, and so

$$\mathcal{N}\mathcal{N}^T = \mathcal{N}\mathcal{N}^\dagger = \mathbb{1} \, . \tag{7.10}$$

Finally, using (7.10), it is a straightforward to show that

$$|\mathrm{TFD}(0)\rangle = \frac{1}{d^{N/2}} \sum_n |E_n\rangle_L \, |E_n\rangle_R = |\mathcal{I}\rangle \ . \tag{7.11}$$

Eq. (7.11) gives us the real-space representation of the infinite-temperature TFD state considered in this work. We note that there is still an ambiguity in its definition, since it depends on the choice of the basis of the local Hilbert space. However, different choices are now related by local unitary transformations, which do not modify the bipartite entanglement. The real-space representation of the finite-time and finite-temperature TFD state is thus simply

$$|\mathrm{TFD}(t)\rangle = \exp\left[-i\frac{t}{2}\left(H_L\otimes\mathbb{1}+\mathbb{1}\otimes H_R\right)\right]\exp\left[-\frac{\beta}{4}\left(H_L\otimes\mathbb{1}+\mathbb{1}\otimes H_R\right)\right]|\mathcal{I}\rangle \ . \tag{7.12}$$

We consider now a bipartition of the two-replica space into the region A_ℓ and its complement A_ℓ^c, where A_ℓ contains the first ℓ sites of both the left and right lattices. The associated Hilbert space is

$$\mathcal{K}_A = (h_1^L\otimes h_1^R)\otimes(h_2^L\otimes h_2^R)\otimes\ldots\otimes(h_\ell^L\otimes h_\ell^R) \, . \tag{7.13}$$

We will be interested in the dynamics of the entanglement between A_ℓ and A_ℓ^c, which can be quantified by the von Neumann entanglement entropy

$$S_{A_\ell}(t) = -\mathrm{tr}\rho_{A_\ell}(t)\ln\rho_{A_\ell}(t) \, , \tag{7.14}$$

where $\rho_{A_\ell}(t)$ is the density matrix at time t reduced to the subsystem A_ℓ, i.e.

$$\rho_{A_\ell}(t) = \mathrm{tr}_{A_\ell^c}\,|\mathrm{TFD}\,(t)\rangle\langle\mathrm{TFD}\,(t)| \ . \tag{7.15}$$

Note that, because of (7.12), $S_{A_\ell}(0) = 0$ for $\beta = 0$.

We will formulate a conjecture for the von Neumann entanglement entropy (7.14) in the scaling limit $\ell, t \to \infty$, where the ratio ℓ/t is kept constant. Our conjecture is based on the quasiparticle picture for standard quenches, which we briefly review in the next subsection.

7.1.2 The TFD quasiparticle content and entanglement dynamics: a conjecture

From the introductory discussion we made in Sec. 2.3, it is not obvious that the standard quasiparticle picture should apply to the TFD dynamics: while the spectrum of the two-replica Hamiltonian (7.3) is still characterized in terms of stable quasiparticles, the TFD state is a very complicated superposition of eigenstates, and one could wonder whether higher n-tuples could contribute. Here we show that, for Bethe Ansatz solvable models, the TFD state (7.12) admits a representation from which the assumption of pairs of quasiparticles appears to be fully justified.

In the following discussion, we will consider an integrable spin chain (or field theory) with periodic boundary conditions, whose eigenstates are parametrized by the sets of quasiparticle rapidities $\{\lambda_j\}$. In addition, we will assume that the real-space representation of the eigenstates $|E(\{\lambda_j\})\rangle$ is such that

$$\overline{\langle\{j\}|E(\{\lambda_j\})\rangle} = \langle\{j\}|E(\{-\lambda_j\})\rangle \ . \tag{7.16}$$

This property can be verified at the level of the eigenfunctions in all integrable models which will be considered in this work. In fact, this relation has a physical meaning: provided that the Hamiltonian is real in the computational basis $|\{j\}\rangle$, complex conjugation corresponds to time inversion, which has the effect of flipping the sign of the quasiparticle momenta.

Since eigenstates with opposite sets of rapidities have the same energy, we can define the new Hamiltonian eigenstates

$$|\mathcal{E}^{+}(\{\lambda_j\})\rangle = \frac{1}{\sqrt{2}}|E(\{\lambda_j\})\rangle + |E(\{-\lambda_j\})\rangle \ , \tag{7.17}$$

$$|\mathcal{E}^{-}(\{\lambda_j\})\rangle = \frac{i}{\sqrt{2}}\left(|E(\{\lambda_j\})\rangle - |E(\{-\lambda_j\})\rangle\right) \ . \tag{7.18}$$

Now, the eigenbasis $\{|\mathcal{E}^{\pm}(\{\lambda_j\})\rangle\}$ satisfies (7.9), and so

$$|\mathcal{I}\rangle \propto \sum_{\alpha=\pm}\sum_{\{\lambda_j\}} |\mathcal{E}^{\alpha}(\{\lambda_j\})\rangle \otimes |\mathcal{E}^{\alpha}(\{\lambda_j\})\rangle \ . \tag{7.19}$$

Using (7.17), we finally obtain

$$|\mathcal{I}\rangle = \frac{1}{d^{N/2}}\sum_{\{\lambda_j\}} |E(\{\lambda_j\})\rangle \otimes |E(\{-\lambda_j\})\rangle \ . \tag{7.20}$$

The interpretation of $|\mathcal{I}\rangle$ in terms of quasiparticles is now clear: it is a superposition of eigenstates, in which any quasiparticle moving in the first replica space with rapidity λ_j is paired to one moving in the second replica space with opposite rapidity $-\lambda_j$.

Eq. (7.20) provides a basis for the application of the standard quasiparticle picture to the TFD dynamics. Based on the latter, we conjecture that Eq. (2.4) describes *exactly*

the TFD entanglement dynamics in the scaling limit of large t and ℓ, with the ratio t/ℓ kept constant.

In order to give Eq. (2.4) predictive power, we need to specify the functions $s_n(\lambda) = s^{\rm TFD}_{(n)}(\lambda)$ and $v_n(\lambda) = v^{\rm TFD}_{(n)}(\lambda)$. Following the logic of Refs. [44, 45], they are determined by the stationary state (GGE) emerging at large times after a quench from the TFD state. Since the latter is a purification of the Gibbs state, the expectation value of all the local conserved quantities coincide with the thermal one, so that the GGE is simply the Gibbs ensemble with inverse temperature β. Thus, we arrive at the identification (dropping the index n)

$$v^{\rm TFD}(\lambda) = v^{\beta}(\lambda)\,, \tag{7.21a}$$

$$s^{\rm TFD}(\lambda) = 2s^{\beta}(\lambda)\,, \tag{7.21b}$$

where $v^{\beta}(\lambda)$ and $s^{\beta}(\lambda)$ are the thermal velocity of excitations and thermodynamic entropy at inverse temperature β, respectively. The factor of 2 in Eq. (7.21b) follows from the fact that the local dimension in the doubled space is the square of the original one. The quasiparticle prediction consisting of Eqs. (2.4) and (8.57) first appeared in Ref. [231], where it has been tested against analytic calculations in free scalar quantum field theories.

We stress that the validity of the quasiparticle picture formulated above is a conjecture: as in the case of standard quenches [44, 45], it is highly non-trivial to derive rigorously predictions in the scaling limit starting from the microscopic theory, even if the explicit spectral decomposition of the initial state is known, cf. Eq. (7.20). Although we expect that in the non-interacting case a rigorous derivation could be carried out by generalizing Ref. [43], at the moment a proof in the presence of interactions appears to be out of reach. In the next sections, we will provide strong evidence of its validity by comparison against analytic and numerical calculations in concrete integrable spin chains.

7.2 The XY model

We begin our analysis of the TFD entanglement dynamics by focusing on a prototypical example of a non-interacting spin chain, the so-called XY model, whose Hamiltonian reads

$$H_{XY}(\gamma,h) = -\frac{1}{2}\sum_{j=1}^{N}\left[\left(\frac{1+\gamma}{2}\right)\sigma_j^x\sigma_{j+1}^x + \left(\frac{1-\gamma}{2}\right)\sigma_j^y\sigma_{j+1}^y + h\sigma_j^z\right]\,, \tag{7.22}$$

where σ_j^α are the Pauli matrices, and periodic boundary conditions are assumed. This model can be solved exactly by means a Jordan-Wigner (JW) transformation. Introducing the fermionic modes

$$c_j = \left(\bigotimes_{k=1}^{j-1}\sigma_k^z\right)\sigma_j^-\,, \qquad c_j^\dagger = \left(\bigotimes_{k=1}^{j-1}\sigma_k^z\right)\sigma_j^+\,, \tag{7.23}$$

the Hamiltonian (7.22) is mapped onto

$$H = -\frac{1}{2}\sum_{j=1}^{N-1}\left(c_j^\dagger c_{j+1} + c_{j+1}^\dagger c_j + \gamma c_j^\dagger c_{j+1}^\dagger + \gamma c_{j+1} c_j\right) + h\sum_{j=1}^{N} c_j^\dagger c_j - \frac{hN}{2} + \frac{P}{2}\left(c_N^\dagger c_1 + c_1^\dagger c_N + \gamma c_N^\dagger c_1^\dagger + \gamma c_1 c_N\right) . \tag{7.24}$$

Here $P = \prod_{j=1}^{N}\left(1 - 2c_j^\dagger c_j\right)$ is the parity operator, which determines periodic (antiperiodic) boundary conditions in the sector of odd (even) fermionic numbers. Since we will be interested in the scaling limit of the entanglement of large subsystem sizes, we can neglect boundary effects, and focus on the fermionic Hamiltonian with periodic boundary conditions [1], i.e.

$$H = -\frac{1}{2}\sum_{j=1}^{N}\left(c_j^\dagger c_{j+1} + c_{j+1}^\dagger c_j + \gamma c_j^\dagger c_{j+1}^\dagger + \gamma c_{j+1} c_j\right) + h\sum_{j=1}^{N} c_j^\dagger c_j - \frac{hN}{2} . \tag{7.25}$$

In order to obtain a mapping to free fermions in the TFD setting, one needs to apply the JW transformation to both replicas independently. However, this procedure leads to a subtlety which needs to be taken into account. Indeed, since operators in the two spaces commute, applying the JW transformation to the two replicas independently yields mixed commutation relations: by construction, given two operators obtained by the JW transformation, they commute if they act on distinct replicas, and anti-commute otherwise. On the other hand, in order to map the spin system onto a truly fermionic one, all the transformed operators should anti-commute. Luckily, there is a simple way to get around this problem, which consists in a redefinition of the fermionic operators. Since this is a rather technical point, we discuss it in Appendix 7.A.

Crucially, the JW transformation maps the space of the first ℓ spins onto that of the first ℓ fermions, for all $\ell < N$. As a consequence, the bipartite entanglement entropy of the original spin chain can be obtained from the corresponding fermionic system [249]. Putting all together, we are left with the problem of computing the bipartite TFD entanglement dynamics for a quadratic fermionic Hamiltonian.

This problem is now analogous to that treated in Ref. [231], where quadratic *bosonic* field theories were considered. There, the TFD entanglement dynamics was computed exactly using that the TFD state is Gaussian, i.e. it satisfies Wick's theorem. This allows one to express its entanglement entropy in terms of the covariance matrix [249], which, in turn, can be computed efficiently at any time. This logic can be followed without modifications also for fermionic degrees of freedom. In the following, we carry out this program explicitly for the model (7.25).

As a first step, we recall that the Hamiltonian (7.25) may be brought to a diagonal

[1] Alternatively, one could also consider the XY spin chain with open boundary conditions, so that no boundary terms appear after applying the Jordan-Wigner transformation.

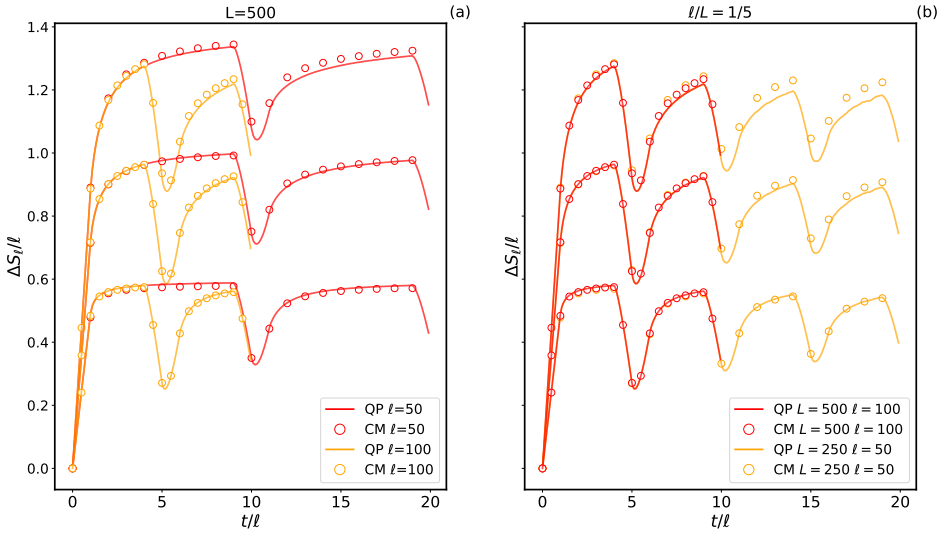

Figure 7.1: Comparison between the exact entanglement dynamics and quasiparticle predictions in the XY spin chain. The system parameters are $\gamma = h = 0$, while in both plots the reverse temperature is $\beta = 0, 2, 4$, increasing from the top to the bottom. In the left panel, the system size is fixed to $L = 500$, and different subsystem sizes are considered. In the right panel, we fix the ratio ℓ/L, and explore the dependence on the system size L. In both figures, we plot $\Delta S_\ell(t)/\ell = [S_\ell(t) - S_\ell(0)]/\ell$, where $S_\ell(0)$ is the bipartite entanglement entropy in the initial state.

form by combining the Fourier transform with the Bogoliubov rotation [250], yielding

$$H = \sum_{q=0}^{N-1} \varepsilon\left(k_q\right) \left\{ b_q^\dagger b_q - \frac{N}{2} \right\} , \tag{7.26}$$

where $k_q = \frac{2\pi}{N} q$, and

$$\varepsilon(\alpha) \equiv \sqrt{(h - \cos\alpha)^2 + \gamma^2 \sin^2\alpha} \, . \tag{7.27}$$

Here $b_j = U_{j,k} c_k$, where $U_{j,k}$ is a suitably defined unitary matrix, whose explicit expression is given in Appendix 7.B. In this basis, the TFD (7.20) reads

$$|\mathrm{TFD}(\mathrm{t},\beta)\rangle = \frac{1}{2^{N/2}} \sum_{\{q_n\}} \exp\left\{ -it \sum_j [\varepsilon(k_{q_j}) - \frac{\beta}{2}\varepsilon(k_{q_j})] \right\} (b_{q_1}^{L\dagger} b_{-q_1}^{R\dagger}) \ldots (b_{q_n}^{L\dagger} b_{-q_n}^{R\dagger}) \, |0\rangle \ , \tag{7.28}$$

where $|0\rangle$ is the vacuum associated with the modes b_j, i.e. $b_j \, |0\rangle = 0$ for all b_j. Note that $|\mathrm{TFD}(0,0)\rangle$ is a product state of Bell pairs, with the modes $b_{q_k}^L$, $b_{q_{-k}}^R$ being maximally entangled.

The covariance matrix of (7.28) is block-diagonal, and thus very easy to compute, as we detail in Appendix 7.B (similar calculations were performed in Ref. [232]). Specifically, introducing the Majorana modes

$$\psi_{2k}^L = \frac{1}{\sqrt{2}}(b_k^{L\dagger} + b_k^L) \, , \qquad \psi_{2k+1}^L = \frac{i}{\sqrt{2}}(b_k^{L\dagger} - b_k^L) \, , \tag{7.29}$$

$$\psi_{2k}^R = \frac{1}{\sqrt{2}}(b_{-k}^{R\dagger} + b_{-k}^R) \, , \qquad \psi_{2k+1}^R = \frac{i}{\sqrt{2}}(b_{-k}^{R\dagger} - b_{-k}^R) \, , \tag{7.30}$$

we obtain

$$\langle \psi_{r_j}^\alpha \psi_{s_j}^\beta \rangle = \tag{7.31}$$

$$= \begin{pmatrix} 0 & \sin[2\varphi(k_j)]\sin[\varepsilon(k_j)t] & \cos[2\varphi(k_j)] & \sin[2\varphi(k_j)]\cos[\varepsilon(k_j)t] \\ -\sin[2\varphi(k_j)]\sin[\varepsilon(k_j)t] & 0 & -\sin[2\varphi(k_j)]\cos[\varepsilon(k_j)t] & \cos[2\varphi(k_j)] \\ -\cos[2\varphi(k_j)] & \sin[2\varphi(k_j)]\cos[\varepsilon(k_j)t] & 0 & -\sin[2\varphi(k_j)]\sin[\varepsilon(k_j)t] \\ -\sin[2\varphi(k_j)]\cos[\varepsilon(k)t] & -\cos[2\varphi(k_j)] & \sin[2\varphi(k_j)]\sin[\varepsilon(k_j)t] & 0 \end{pmatrix} , \tag{7.32}$$

with

$$\varphi(k) = \arctan(e^{-\beta\varepsilon(k)/2}) \, , \tag{7.33}$$

where $\alpha, \beta = L, R$, $r_j, s_j = 2j, 2j{+}1$ and the Majorana modes are ordered as $(\psi_{2j}^L, \psi_{2j}^R, \psi_{2j+1}^L, \psi_{2j+1}^R)$. Finally, setting

$$\chi_{2k}^\alpha = \frac{1}{\sqrt{2}}(c_k^{\alpha\dagger} + c_k^\alpha) \, , \qquad \chi_{2k+1}^\alpha = \frac{i}{\sqrt{2}}(c_k^{\alpha\dagger} - c_k^\alpha) \, , \tag{7.34}$$

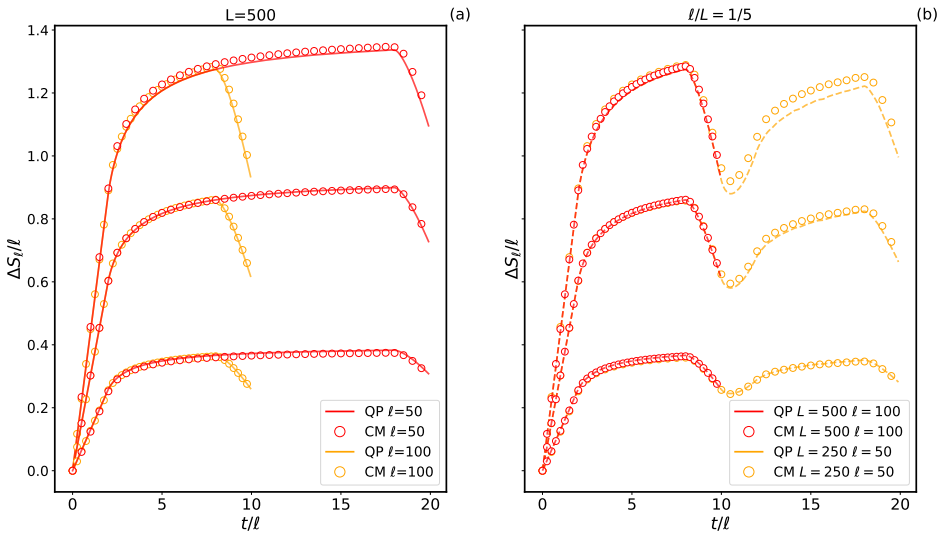

Figure 7.2: Same as Fig. 7.1. The system parameters are $\gamma = 0.5$, $h = 0$, while in both plots the reverse temperature is $\beta = 0, 2, 4$, increasing from the top to the bottom

and expressing the modes $\{c_j\}$ in terms of $\{b_j\}$, we obtain the covariance matrix

$$\Gamma^{\alpha,\beta}_{j,k}(t,\beta) = \langle \mathrm{TFD(t,}\,\beta)|\chi^{\alpha}_{j}\chi^{\beta}_{k}|\mathrm{TFD(t,}\,\beta)\rangle \ . \tag{7.35}$$

Note that the definition of the left/right Majorana modes (7.29) involve opposite quasi-momenta, which must be taken into account when expressing $\{c_j\}$ in terms of $\{b_j\}$ [cf. Appendix 7.B for details].

The covariance matrix (7.35) now gives us direct access to the bipartite von Neumann entanglement entropy $S_\ell(t)$ [249]: denoting by $\Gamma_\ell(t)$ the covariance matrix restricted to the first ℓ sites, we have

$$S_\ell(t) = -\,\mathrm{tr}\left[\frac{1+i\Gamma_\ell(t)}{2}\ln\frac{1+i\Gamma_\ell(t)}{2}\right] . \tag{7.36}$$

This formula can be evaluated in a numerically exact and efficient way for large system sizes and times, and for arbitrary values of the Hamiltonian parameters (7.22). It thus provides the possibility of a very stringent test for our analytic predictions.

Eq. (8.57) has been derived assuming that the limit $N \to \infty$ is taken first, i.e. for $\ell/N \to 0$. On the other hand, when evaluating (7.36), finite-ℓ effects are visible even for relatively large sizes. Therefore, in order to test the quasiparticle picture and following Ref. [231], it is first convenient to adapt the formula (8.57) to a ring geometry where the ratio ℓ/N is kept constant. This also allows us to explore the interesting revivals of the entanglement dynamics. By the usual argument, counting the number of pairs with

one quasiparticle in A and the other in A^c, and taking into account periodic boundary conditions, we arrive at the formula

$$S_\ell(t)/\ell = \int_{-\pi}^{\pi} \mathrm{d}k \begin{cases} (N/\ell) s_{\mathrm{TFD}}(k) \mathrm{frac}\left(\frac{v(k)t}{N}\right) & \text{if } N\mathrm{frac}(\frac{vt}{N}) < \ell\,, \\ s_{\mathrm{TFD}}(k) & \text{if } \ell \leq N\mathrm{frac}(\frac{v(k)t}{N}) < N-\ell\,, \\ (N/\ell) s_{\mathrm{TFD}}(k) \left[1 - \mathrm{frac}\left(\frac{v(k)t}{N}\right)\right] & \text{if } N-\ell < N\mathrm{frac}\left(\frac{v(k)t}{N}\right)\,. \end{cases} \tag{7.37}$$

Since the system is non-interacting, the velocity and entropy contributions of the quasiparticles are not "dressed", and can be immediately read off from the diagonal form of the Hamiltonian (7.26), yielding

$$v_{\mathrm{TFD}}(k) = \varepsilon'(k) \tag{7.38}$$

$$s_{\mathrm{TFD}}(k) = 2\left[\frac{\beta\varepsilon(k)}{1+e^{\beta\omega_n}} + \log(1+e^{-\beta\varepsilon(k)}\right]\,, \tag{7.39}$$

where $\varepsilon(k)$ is given in (7.27), while the extra factor accounts for the doubling of the local Hilbert space dimension.

We have evaluated Eqs. (7.36) and (7.37) for large systems sizes and different values of the system parameters, and systematically compared the results. Examples of our numerical data is given in Figs. 7.1 and 7.2. We find that, at short times and high temperatures, the agreement is extremely good even for relatively small system sizes. As the temperature is lowered and wider time intervals are considered, increasing system sizes are needed in order to observe the same accuracy in the quasiparticle predictions. We also see that the entanglement revivals are perfectly captured by the analytic formula (7.37). In general, we have found excellent agreement between the exact entanglement dynamics and the quasiparticle prediction, giving us very strong evidence for the validity of the conjecture in the non-interacting case.

7.3 The XXZ Heisenberg spin chain

We move on to test our conjecture in genuinely interacting integrable systems and consider the prototypical example of the XXZ Heisenberg model [251]

$$H_{\mathrm{XXZ}} = \frac{1}{4}\sum_{j=1}^{N}\left[\sigma_j^x\sigma_{j+1}^x + \sigma_j^y\sigma_{j+1}^y + \Delta\left(\sigma_j^z\sigma_{j+1}^z - \frac{1}{4}\right)\right]\,, \tag{7.40}$$

where σ_j^α are Pauli matrices acting on the local space $h_j \simeq \mathbb{C}^2$, while Δ is the anisotropy parameter.

Although the model is integrable, interactions make it notoriously hard to analyze its out-of-equilibrium dynamics analytically [10]. For instance, it is not known how to compute the evolution of any non-trivial physical quantity following a quantum quench (with the only exception being the so-called Loschmidt echo [252, 253]). Accordingly, in

order to obtain an exact description of the TFD dynamics, we need to rely on numerical methods of general validity.

Since we are interested in the limit of large system sizes, we employ tensor-network (TN) methods [235]. In order to do so, it is crucial that the infinite-temperature TFD state is a product state in the real-space representation, [cf. Eq. (7.7)] and that, more generally, it maintains low spatial entanglement at finite values of β. Indeed, this allows us to represent it efficiently as a Matrix Product State (MPS) [254] with small bond dimension, and apply standard algorithms for its time evolution.

Unfortunately, the linear growth of the bipartite entanglement entropy poses practical limitations on the time scales which can be simulated [235], and our numerical results are often plagued by severe finite-time effects. For this reason, we limit ourselves to test the quasiparticle prediction in a simple setting where the latter are easier to take into account: we compute the growth of the TFD entanglement entropy for a bipartition of an infinite spin chain. In order to simulate the system directly in the thermodynamic limit we employ the iTEBD algorithm [186].

Importantly, while numerical calculations are performed for infinite systems, in the iTEBD algorithm an approximation is made by introducing a finite *bond dimension* [235] traditionally denoted by χ, which sets an effective cutoff for the maximum entanglement values which can be simulated, and allows us to estimate the interval of validity of our numerical computations.

From the point of view of the quasiparticle picture, Eq. (2.4) simplifies when considering half of an infinite system, since there is no saturation of entanglement. Specifically, taking $\ell \to \infty$ in (2.4), we obtain

$$S(t) = 2t \sum_n \int \mathrm{d}\lambda |v_n(\lambda)| s_n(\lambda)\,, \tag{7.41}$$

where the integral is over all the allowed quasimomenta. This equation is expected to be exact in the limit $t \to \infty$, and yields a prediction for the asymptotic rate of growth $dS(t)/dt$ of the bipartite entanglement entropy.

As before, in order to evaluate (7.41), one needs to specify the quasiparticle content of the model, i.e. the types of possible quasiparticles, together with their velocity and entropy contribution at thermal equilibrium. In the XXZ Heisenberg model, these data can be obtained via the so-called Thermodynamic Bethe Ansatz [78]. Contrary to the non-interacting case, they don't have an elementary form and their structure depends on the value of Δ. Therefore, in the following, we will consider separately the regimes $\Delta > 1$ and $0 < \Delta < 1$, and test the quasiparticle prediction in the two cases [2].

7.3.1 The regime $\Delta > 1$

The structure of the quasiparticles is particularly simple when $\Delta > 1$. In this case, quasiparticles can form bound states of arbitrary numbers, and, in the thermodynamic

[2] Without loss of generality, we can assume $\Delta > 0$, since the case $\Delta < 0$ can be obtained by a unitary similarity transformation, and simultaneously flipping the sign of the temperature [251].

limit, the system is characterized by an infinite set of *rapidity distribution functions* $\{\rho_n(\lambda)\}_{n=1}^{\infty}$. Here $\lambda \in [-\pi/2, \pi/2]$, while the integer n indicates the number of quasiparticles in the bound states. The functions $\rho_n(\lambda)$ can be thought of as a generalization of the quasimomentum occupation numbers describing non-interacting quantum gases at thermal equilibrium. Together with $\{\rho_n(\lambda)\}$, the state of the system is also characterized by the set of *hole* distribution functions $\{\rho_n^h(\lambda)\}$, giving information on the density of vacant quasimomenta which could be occupied by the quasiparticles.

Due to interactions, the relation between $\{\rho_n(\lambda)\}$ and $\{\rho_n^h(\lambda)\}$ is non-trivial, and takes the form [78]

$$\rho_m(\lambda) + \rho_m^h(\lambda) = a_m(\lambda) - \sum_{n=1}^{\infty} \left[a_{mn} * \rho_n\right](\lambda)\,, \tag{7.42}$$

where we defined

$$(f * g)(\lambda) = \int_{-\pi/2}^{\pi/2} d\mu f(\lambda - \mu) g(\mu) \tag{7.43}$$

and

$$a_{mn}(\lambda) = (1 - \delta_{mn})\, a_{|m-n|}(\lambda) + 2a_{|m-n|}(\lambda) + \ldots + 2a_{m+n-2}(\lambda) + a_{m+n}(\lambda), \tag{7.44}$$

$$a_n(\lambda) = \frac{1}{\pi} \frac{\sinh(n\eta)}{\cosh(n\eta) - \cos(2\lambda)}\,. \tag{7.45}$$

with $\cosh(\eta) = \Delta$.

The solution to (7.42) is not unique, and an additional set of equations must be provided in order to completely determine the quasiparticle distribution functions at inverse temperature β. Introducing the function

$$\eta_n(\lambda) = \frac{\rho_n^h(\lambda)}{\rho_n(\lambda)}\,, \tag{7.46}$$

the latter take the form [78]

$$\log \eta_n(\lambda) = -\beta\pi \sinh(\eta) a_n(\lambda) + \sum_{m=1}^{\infty} \left[a_{nm} * \log\left(1 + \eta_m^{-1}\right)\right](\lambda)\,. \tag{7.47}$$

Eqs. (7.42) and (7.47) are a closed set of equations, and can be solved by standard iterative methods. Clearly, in order to do so, one must truncate the infinite system, keeping only a finite number $n_{\max}$ of equations (with the accuracy of the numerical solution increasing with $n_{\max}$). The functions $\rho_n(\lambda)$ and $\rho_n^h(\lambda)$ obtained in this way completely determine the thermal properties of the system. In particular, they allow one to obtain the velocities of the quasiparticles $v_n(\lambda)$ as the solution to [188]

$$[\rho_n^h(\lambda) + \rho_n(\lambda)] v_n(\lambda) = -\frac{\sinh\eta}{2} a_m'(\lambda) - \sum_{n=1}^{\infty} \left[a_{mn} * \rho_n v_n\right](\lambda)\,, \tag{7.48}$$

while $s_n(\lambda)$ is given by the so-called Yang-Yang entropy [78]

$$s_n(\lambda) = [\rho_n(\lambda) + \rho_n^h(\lambda)] \ln[\rho_n(\lambda) + \rho_n^h(\lambda)] - \rho_n(\lambda) \ln \rho_n(\lambda) - \rho_n^h(\lambda) \ln \rho_n^h(\lambda) \,. \tag{7.49}$$

We have solved numerically Eqs. (7.42), (7.47), and (7.48). Plugging the result for $v_n(\lambda)$ and $s_n(\lambda)$ [obtained from (7.49)] into (7.41), we obtain the final quasiparticle prediction for the late-time rate of growth of the bipartite entanglement entropy. A plot for different values of β is displayed in Fig. 7.3.

In Fig. 7.4 we compare the quasiparticle prediction with our numerical iTEBD calculations. In the first plot, we show $dS(t)/dt$ as a function of time for $\Delta = 1, 2, 3$ at $\beta = 0$, reporting data for two different bond dimensions (dashed and solid lines): the time t_0 at which the two curves start to deviate from one another gives us an estimate of the maximum time interval for which our data are reliable. We can see that t_0 decreases with Δ, which is consistent with the fact that the entanglement entropy appears to grow faster for larger Δ at short times.

For all the values of the anisotropy, we see short-time oscillations whose amplitude is large compared to the range of variation of $dS(t)/dt$ displayed in Fig. 7.3. This short-time regime is followed by a slow decaying behavior, suggesting large finite-time effects. In the right panel of Fig. 7.4, we have plotted the difference between the quasiparticle prediction at late times and $dS(t)/dt$, from which we clearly see a power law decay to zero, finally confirming the validity of our analytic formula (7.41).

From Fig. 7.3, we see a very weak dependence of the asymptotic value of $dS(t)/dt$ on the inverse temperature β. On the other hand, the entanglement of the zero-time TFD state increases with β, further limiting the time scales accessible to our simulations. For this reason, we were not able to perform a meaningful test of the dependence on β for $\Delta > 1$.

7.3.2 The regime $0 < \Delta < 1$

The quasiparticle content is significantly more complicated for $\Delta < 1$. Setting $\gamma = \arccos(\Delta)$, simplifications occur when γ/π is a rational number. In this case, quasiparticles can still form bound states, but containing at most a finite number N_b of them. The value of N_b and the properties of the quasiparticles depend on the length of the continued-fraction representation of γ/π [78]. In this section, we will restrict ourselves to the case where the latter is at most two. Values of γ/π with longer continued-fraction representations correspond to a more involved quasiparticle structure, and are only expected to lead to technical, rather than conceptual, complications. We will consider in particular

$$\gamma = \frac{\pi}{1 + \nu_1} \,, \tag{7.50}$$

with $\nu_1 = 2, 3, \ldots$, where we have $N_b = 1 + \nu_1$, and also

$$\gamma = \frac{\pi}{\nu_1 + \frac{1}{\nu_2}} \,, \tag{7.51}$$

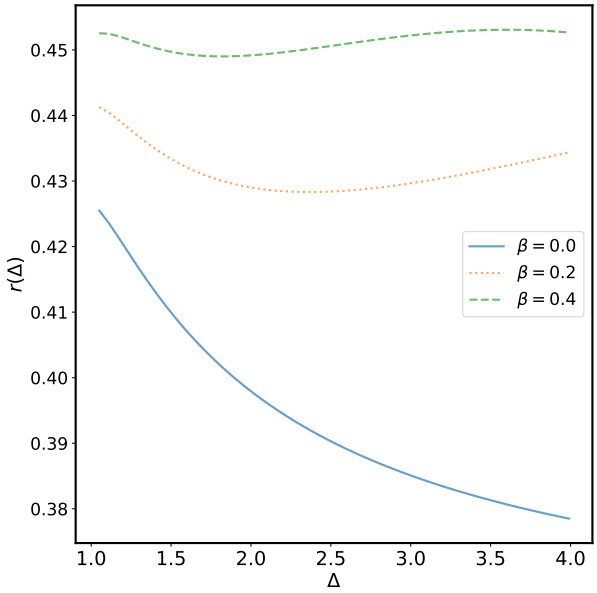

Figure 7.3: Quasiparticle prediction for the asymptotic rate of growth $r(\Delta) = \lim_{t\to\infty} dS(t)/dt$, as a function of $\Delta > 1$ and for different values of $\beta = 0, 0.2, 0.4$. The curves are obtained by evaluating (7.41), after solving numerically Eqs. (7.42), (7.47), (7.48), and using (7.49).

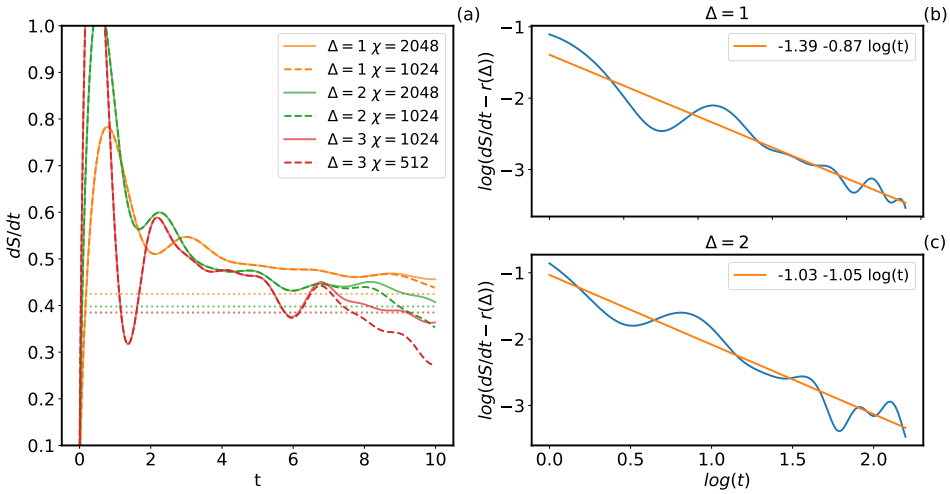

Figure 7.4: Infinite-temperature TFD entanglement dynamics for $\beta = 0$ and $\Delta > 1$. Left: Rate of entanglement growth for different value of Δ as a function of time. Dashed and solid lines correspond to iTEBD data obtained using bond dimension $\chi = 1024$ and $\chi = 2048$, respectively. Straight dotted lines are the predictions from the quasiparticle picture. Right: Difference between the iTEBD data and the asymptotic formula (7.41), in log-log plot. The straight line is a linear fit. The plot clearly reveals a power-law approach to zero, confirming the validity of the quasiparticle prediction.

with $\nu_1, \nu_2 \geq 2$. In this case, the maximum number of quasiparticles forming a bound state is $N_b = \nu_1 + \nu_2$.

As before, we can characterize the system in the thermodynamic limit in terms of the rapidity and hole distribution functions $\{\rho_n(\lambda)\}$, $\{\rho_n^h(\lambda)\}$, where now $n = 1, \dots N_b$, and $\lambda \in (-\infty, +\infty)$. The relation between the two reads

$$a_j(\lambda) = \sigma_j \left[\rho_j(\lambda) + \rho_j^h(\lambda)\right] + \sum_{k=1}^{N_b} [a_{jk} * \rho_k](\lambda)\,, \tag{7.52}$$

where

$$(f * g)(\lambda) = \int_{-\infty}^{\infty} d\mu f(\lambda - \mu) g(\mu)\,, \tag{7.53}$$

and

$$a_{jk}(\lambda) = \left(1 - \delta_{n_j n_k}\right) a^{v_j v_k}_{|n_j - n_k|}(\lambda) + 2a^{v_j v_k}_{|n_j - n_k|+2}(\lambda) + \ldots + 2a^{v_j v_k}_{n_j + n_k - 2}(\lambda) + a^{v_j v_k}_{n_j + n_k}(\lambda)\,, \tag{7.54}$$

$$a^{v_j}_{n_j}(\lambda) = \frac{v_j}{\pi} \frac{\sin(\gamma n_j)}{\cosh(2\lambda) - v_j \cos(\gamma n_j)}\,, \tag{7.55}$$

$$\sigma_j = \text{sign}\,(q_j)\ . \tag{7.56}$$

In Eqs. (7.54), (7.56), n_j, v_j and , q_j depend on the length of the continued-fraction representation of γ. In the case (7.50), we have

$$\begin{cases} n_j = j, & v_j = 1, \quad j = 1, 2 \ldots, \nu_1\,, \\ n_{\nu_1+1} = 1, & v_{\nu_1+1} = -1\,, \end{cases} \tag{7.57}$$

and

$$\begin{cases} q_j = \nu_1 + 1 - n_j \quad j = 1, 2 \ldots, \nu_1\,, \\ q_{\nu_1+1} = -1\,. \end{cases} \tag{7.58}$$

In the case (7.51), instead, we have

$$n_j = \begin{cases} j & 1 \leq j \leq \nu_1 - 1\,, \\ 1 + (j - \nu_1)\,\nu_1 & \nu_1 \leq j \leq \nu_1 + \nu_2 - 1\,, \\ \nu_1 & j = \nu_1 + \nu_2\,, \end{cases} \tag{7.59}$$

$$v_j = \begin{cases} +1 & 1 \leq j \leq \nu_1 - 1\,, \\ -1 & j = \nu_1 \\ \exp\left(i\pi\, \text{floor}\left[(n_j - 1)\,\frac{\nu_2}{1+\nu_1, \nu_2}\right]\right) & \nu_1 + 1 \leq j \leq \nu_1 + \nu_2\,, \end{cases} \tag{7.60}$$

where floor(x) is the floor function, and

$$q_j = \begin{cases} \frac{1+\nu_1\nu_2}{\nu_2} - j & 1 \leq j \leq \nu_1 - 1\,, \\ \frac{1}{\nu_2}\,(j - \nu_1) - 1 & \nu_1 \leq j \leq \nu_1 + \nu_2 - 1\,, \\ \frac{1}{\nu_2} & j = \nu_1 + \nu_2\,. \end{cases} \tag{7.61}$$

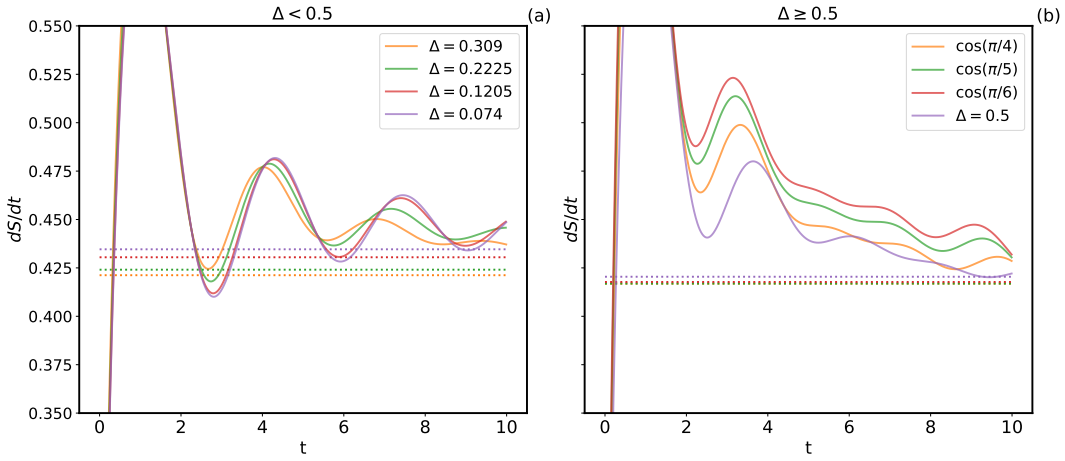

Figure 7.5: Infinite-temperature TFD entanglement dynamics for $\beta = 0$ and $0 < \Delta < 1$. Solid lines correspond to iTEBD data obtained using bond dimension $\chi = 2048$, while straight dotted lines are the predictions from the quasiparticle picture.

Analogously to the case $\Delta > 1$, Eq. (7.52) has to be complemented with an additional set of equations to determine the thermal stationary state. For both cases (7.50) and (7.51), it reads [78]

$$\ln \eta_j(\lambda) = \beta e_j(\lambda) + \sum_{k=1}^{N_b} \sigma_k [a_{jk} * \ln\left(1 + \eta_k^{-1}\right)](\lambda)\,, \tag{7.62}$$

where

$$e_j(\lambda) = -\pi \sin\gamma a_{n_j}^{v_j}(\lambda)\,, \tag{7.63}$$

and $\eta_n(\lambda)$ is defined in (7.46). Finally, from the knowledge of the thermal rapidity and hole distribution functions, the entropy contribution is given by the Yang-Yang entropy (7.49), while the velocity is obtained by solving the system

$$\frac{e_j'(\lambda)}{2\pi} = \sigma_j v_j(\lambda) \left[\rho_j(\lambda) + \rho_j^h(\lambda)\right] + \sum_{k=1}^{N_b} [a_{jk} * v_k \rho_k](\lambda)\,. \tag{7.64}$$

We have solved numerically Eqs. (7.52), (7.62) and (7.64) by standard iterative methods, after introducing a finite cutoff Λ in the space of rapidities.

In Fig. 7.5 we compare the prediction obtained using Eq. (7.41) with our numerical iTEBD calculations. In general, we find that larger finite-time effects are visible, compared to the case $\Delta > 1$. For $0.5 \leq \Delta < 1$, we see that $dS(t)/dt$ appears to decrease in time towards our asymptotic predictions, decaying more slowly as Δ approaches 1. Unfortunately, however, although the data are qualitatively consistent with our prediction, the time scales which we can simulate do not allow us to make a more accurate quantitative comparison.

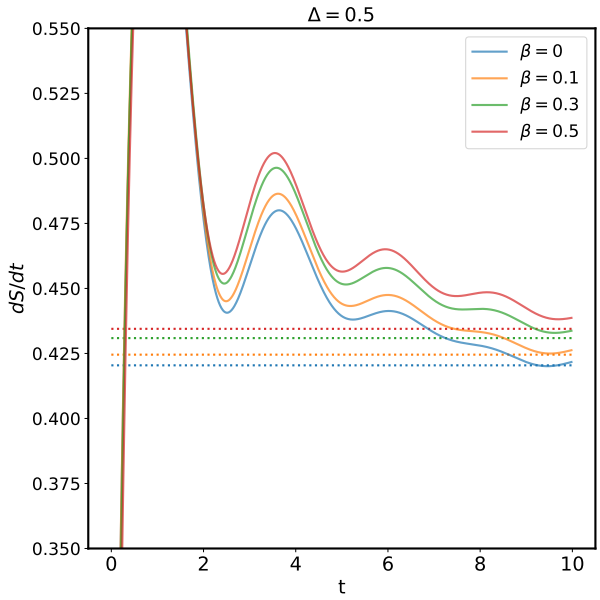

Figure 7.6: Finite-temperature TFD entanglement dynamics for $\Delta = 0.5$. Solid lines correspond to iTEBD data obtained using bond dimension $\chi = 2048$, while straight dotted lines are the predictions from the quasiparticle picture.

The situation appears to be worse in the case $\Delta < 0.5$ shown in the left panel of Fig. 7.5. Here we see large oscillations for the time scales which we can simulate. Perhaps unsurprisingly, oscillations are larger as Δ approaches zero, and, within the accessible time scales, only for $\Delta = 0.309$ we are able to see hints of an eventual damping in their amplitudes and the onset of a slowly decaying behavior, following this transient short-time regime. In general, we interpret the visible discrepancies as a manifestation of large finite-time effects, due to proximity to the non-interacting point $\Delta = 0$. From Fig. 7.5, we also see that finite-time effects are less severe for $\Delta = 0.5$. For this value of the anisotropy, we are able to test the dependence of the TFD entanglement entropy on β. Our results are reported in Fig. 7.6, displaying a good quantitative agreement.

7.4 Conclusions

We have studied the entanglement dynamics of TFD states in interacting integrable systems. We have shown that the TFD evolution may be interpreted as a quantum quench from an initial state which is low-entangled in the real-space representation and displays a simple quasiparticle structure. Based on these considerations, we have generalized the quasiparticle picture developed for standard quenches and conjectured a formula for the evolution of the von Neumann entanglement entropy, which is expected to be exact in the scaling limit of large sizes and times.

In the case of integrable spin chains, where exact or efficient numerical calculations

can be performed, we have tested our conjecture finding convincing agreement. More generally, our formula applies to continuous quantum field theories, including, for instance, the Lieb-Liniger gas or the relativistic sinh- and sine-Gordon models. Although in these cases it would be difficult to simulate exactly the dynamics, the quasiparticle structure of these models is well known, leading to a straightforward application of our formulas.

As mentioned, the entanglement dynamics of the infinite-temperature TFD state coincides with the operator-space entanglement entropy of the evolution operator [241, 255]. Therefore, as a byproduct of our work, we obtained an analytic expression for the latter in generic interacting integrable systems. In this respect, it would be interesting to understand whether a similar quasiparticle description could be obtained for other entanglement-related properties of the evolution operator, such as the tripartite mutual information [242], which characterizes the chaotic and scrambling behavior of the many-body dynamics, the negativity [46, 240, 49] or the symmetry resolved entropies [50, 51]. We leave these questions for future work.

7.A The TFD state and the Jordan-Wigner transformation

In this section we provide more detail about the JW transformation in the TFD setting. For concreteness, let us assume N even, and define the following left and right Majorana operators

$$\tilde{\chi}^{\alpha}_{2j} = \left(\bigotimes_{k=1}^{j-1} \sigma^{z,\alpha}_k\right) \sigma^{x,\alpha}_j \,, \qquad \tilde{\chi}^{\alpha}_{2j+1} = \left(\bigotimes_{k=1}^{j-1} \sigma^{z,\alpha}_k\right) \sigma^{y,\alpha}_j \,, \tag{7.65}$$

where $\alpha = L, R$. This definition corresponds to applying a JW transformation independently on the two replica spaces. We note that the set $\{\tilde{\chi}^L_j, \tilde{\chi}^R_j\}$ does not satisfy a fermionic algebra, but a mixed one, since

$$[\tilde{\chi}^L_j, \tilde{\chi}^R_k] = 0 \,, \qquad \{\tilde{\chi}^{\alpha}_j, \tilde{\chi}^{\alpha}_k\} = \delta_{j,k} \,. \tag{7.66}$$

In order to obtain a truly fermionic algebra, we introduce

$$\chi^L_k = i Q^L \tilde{\chi}^L_k \,, \qquad \chi^R_k = Q^L \tilde{\chi}^R_k \,, \tag{7.67}$$

where

$$Q^L = \prod_{j=1}^{2N} \tilde{\chi}^L_j \,. \tag{7.68}$$

One can easily verify that $\{\chi^{\alpha}_j\}$ satisfy fermionic anticommutation relations, namely

$$\{\chi^{\alpha}_j, \chi^{\beta}_k\} = \delta_{j,k}\delta_{\alpha,\beta} \,, \tag{7.69}$$

and that $\chi_j^{\alpha\dagger} = \chi_j^{\alpha}$. Furthermore, since $(Q^L)^2 = \mathbb{1}$, we have

$$\prod_{j=1}^{s} \tilde{\chi}^{\alpha}_{m_j} = \prod_{j=1}^{s} \chi^{\alpha}_{m_j} \,, \tag{7.70}$$

for any integer s.

From Eq. (7.70), we see that we can reformulate the TFD dynamics in terms of the fermionic operators χ_j^{α}. In order to show that the mapping is well defined, however, we also need to make sure that the infinite-temperature state $|\mathcal{I}\rangle$ originally written in terms of spin degrees of freedom, is transformed into a maximally entangled state $|\mathcal{I}_f\rangle$, which is a product state with respect to the fermionic degrees of freedom. To see this, we first note that the state $|\mathcal{I}\rangle$ is completely determined by the set of relations

$$(\mathcal{O}^L \otimes \mathbb{1}) |\mathcal{I}\rangle = (\mathbb{1} \otimes \mathcal{O}^{R,T}) |\mathcal{I}\rangle \,, \tag{7.71}$$

where $\mathcal{O}$ is any operator and $(\cdot)^T$ denotes transposition with respect to the computational basis. By rewriting this equation in the Majorana basis we obtain

$$\chi^L_{2k} |\mathcal{I}_f\rangle = -i\chi^R_{2k} |\mathcal{I}_f\rangle \,, \qquad \chi^L_{2k+1} |\mathcal{I}_f\rangle = i\chi^R_{2k+1} |\mathcal{I}_f\rangle \,, \tag{7.72}$$

i.e. $|\mathcal{I}_f\rangle$ is a purification of the infinite-temperature state, which is also a product state with respect to the fermionic degrees of freedom.

7.B Details on the TFD entanglement dynamics for quadratic fermionic Hamiltonians

In this Appendix we provide further details about the calculation of the TFD entanglement dynamics for the quadratic Hamiltonian (7.25).

We begin by reviewing the diagonalization of the Hamiltonian (7.25), which is standard and carried out in two steps. First, we take the Fourier transform of the fermionic operators

$$c_j = \frac{e^{i\pi/4}}{\sqrt{N}} \sum_{q=0}^{N-1} e^{i\frac{2\pi}{N}qj} \tilde{c}_q, \qquad \tilde{c}_q \equiv \frac{e^{-i\pi/4}}{\sqrt{N}} \sum_{j=1}^{N} e^{-i\frac{2\pi}{N}qj} c_j \,. \tag{7.73}$$

Next, we perform a Bogoliubov rotation

$$\begin{pmatrix} \tilde{c}_{+q} \\ \tilde{c}^{\dagger}_{-q} \end{pmatrix} = \begin{pmatrix} \cos\vartheta_q & \sin\vartheta_q \\ -\sin\vartheta_q & \cos\vartheta_q \end{pmatrix} \begin{pmatrix} b_{+q} \\ b^{\dagger}_{-q} \end{pmatrix} , \qquad \begin{pmatrix} b_{+q} \\ b^{\dagger}_{-q} \end{pmatrix} = \begin{pmatrix} \cos\vartheta_q & -\sin\vartheta_q \\ \sin\vartheta_q & \cos\vartheta_q \end{pmatrix} \begin{pmatrix} \tilde{c}_{+q} \\ \tilde{c}^{\dagger}_{-q} \end{pmatrix} , \tag{7.74}$$

where we defined

$$\tan(2\vartheta_q) = \frac{\gamma \sin\left(\frac{2\pi}{N}q\right)}{h - \cos\left(\frac{2\pi}{N}q\right)} \,. \tag{7.75}$$

The Hamiltonian becomes diagonal in terms of the new modes

$$H = \sum_{q=0}^{N-1} \varepsilon\left(\frac{2\pi}{N}q\right)\left\{b_q^\dagger b_q - \frac{N}{2}\right\}, \tag{7.76}$$

where

$$\varepsilon(\alpha) \equiv \sqrt{(h-\cos\alpha)^2 + \gamma^2\sin^2\alpha}\,. \tag{7.77}$$

Concatenating the Fourier and Bogoliubov transformation, we may directly write down the initial Majorana modes, defined in Eq. (7.34), in terms of the final ones, defined in Eq. (7.29). We have

$$\begin{aligned}\chi_{j,1} = \frac{1}{\sqrt{2}}(c_j + c_j^\dagger) &= \frac{1}{\sqrt{2}}\sum_{q=0}^{N-1}\left[\frac{1}{\sqrt{N}}e^{i\pi/4}e^{2\pi qj/N}\tilde{c}_q + \frac{1}{\sqrt{N}}e^{-i\pi/4}e^{-2\pi qj/N}\tilde{c}_q^\dagger\right] \\ &= \frac{1}{\sqrt{2N}}\sum_{q=0}^{N-1}\Big[\cos(\vartheta_q)\left(e^{i\pi/4+2\pi qj/N}b_q + e^{-i\pi/4-2\pi qj/N}b_q^\dagger\right) \\ &+ \sin(\vartheta_q)\left(e^{i\pi/4+2\pi qj/N}b_{-q}^\dagger + e^{-i\pi/4-2\pi qj/N}b_{-q}\right)\Big]\,.\end{aligned} \tag{7.78}$$

For the second term in the sum, we may rewrite

$$\begin{aligned}&\sum_{q=0}^{N-1}\left[\sin(\vartheta_q)\left(e^{i\pi/4+2\pi qj/N}b_{-q}^\dagger + e^{-i\pi/4-2\pi qj/N}b_{-q}\right)\right] = \\ &= \sum_{q=0}^{N-1}\left[-\sin(\vartheta_q)\left(e^{i\pi/4-2\pi qj/N}b_q^\dagger + e^{-i\pi/4+2\pi qj/N}b_q\right)\right]\end{aligned} \tag{7.79}$$

and so

$$\begin{aligned}\chi_{j,1} &= \frac{1}{\sqrt{2N}}\sum_{q=0}^{N-1}\Big\{b_q\left[\cos\vartheta_q e^{i\pi/4+2\pi qij/N} - \sin\vartheta_q e^{-i\pi/4+2\pi qij/N}\right] + \\ &+ b_q^\dagger\left[\cos\vartheta_q e^{-i\pi/4-2\pi qij/N} - \sin\vartheta_q e^{i\pi/4-2\pi qij/N}\right] \\ &= \frac{1}{\sqrt{N}}\sum_{q=0}^{N-1}\Big\{\psi_{q,1}\left[\cos\vartheta_q\cos\left(\frac{2\pi qj}{N}+\frac{\pi}{4}\right) - \sin\vartheta_q\cos\left(\frac{2\pi qj}{N}-\frac{\pi}{4}\right)\right] \\ &\qquad + \psi_{q,2}\left[-\cos\vartheta_q\sin\left(\frac{2\pi qj}{N}+\frac{\pi}{4}\right) + \sin\vartheta_q\sin\left(\frac{2\pi qj}{N}-\frac{\pi}{4}\right)\right]\Big\}\,.\end{aligned} \tag{7.80}$$

Analogously, we have

$$\begin{aligned}\chi_{j,2} &= \frac{i}{\sqrt{2N}}\sum_{q=0}^{N-1}\Big\{b_q\left[-\sin\vartheta_q e^{-i\pi/4+2\pi qij/N}-\cos\vartheta_q e^{i\pi/4+2\pi qij/N}\right]\\ &\quad+b_q^\dagger\left[\cos\vartheta_q e^{-i\pi/4-2\pi qij/N}+\sin\vartheta_q e^{i\pi/4-2\pi qij/N}\right]\Big\}\\ &= \frac{1}{\sqrt{N}}\sum_{q=0}^{N-1}\left\{\psi_{q,1}\left[\sin\vartheta_q\sin\left(\frac{2\pi qj}{N}-\frac{\pi}{4}\right)+\cos\vartheta_q\sin\left(\frac{2\pi qj}{N}+\frac{\pi}{4}\right)\right]\right.\\ &\quad\left.+\psi_{q,2}\left[\sin\vartheta_q\cos\left(\frac{2\pi qj}{N}-\frac{\pi}{4}\right)+\cos\vartheta_q\cos\left(\frac{2\pi qj}{N}+\frac{\pi}{4}\right)\right]\right\}.\end{aligned} \tag{7.81}$$

Let us now consider the two-replica Hilbert space and denote by $\psi_{j,\alpha}^{L/R}$ the left/right Majorana fermions. We define the ordered vectors

$$\psi=(\psi_1\dots\psi_N)\,,\qquad \psi_k=(\psi_{k,1}^L,\psi_{k,1}^R,\psi_{k,2}^L,\psi_{k,2}^R)\,, \tag{7.82}$$

$$\chi=(\chi_1\dots\chi_N)\,,\qquad \chi_k=(\chi_{k,1}^L,\chi_{k,1}^R,\chi_{k,2}^L,\chi_{k,2}^R)\,. \tag{7.83}$$

We can rewrite

$$\chi_j=\sum_k A_{j,k}\psi_k\,, \tag{7.84}$$

where $A=\tilde{A}/\sqrt{N}$ and

$$\begin{aligned}[\tilde{A}_{j,k}]_{1,\alpha} &= \left[\cos(\vartheta_q)c^+\left(\frac{2\pi qj}{N}\right)-\sin(\vartheta_q)c^-\left(\frac{2\pi qj}{N}\right),0,-\cos(\vartheta_q)s^+\left(\frac{2\pi qj}{N}\right)+\sin(\vartheta_q)s^-\left(\frac{2\pi qj}{N}\right),0\right]\\ [\tilde{A}_{j,k}]_{2,\alpha} &= \left[0,\cos(\vartheta_{-q})c^+\left(-\frac{2\pi qj}{N}\right)-\sin(\vartheta_{-q})c^-\left(-\frac{2\pi qj}{N}\right),0,-\cos(\vartheta_{-q})s^+\left(-\frac{2\pi qj}{N}\right)+\sin(\vartheta_{-q})s^-\left(-\frac{2\pi qj}{N}\right.\right.\\ [\tilde{A}_{j,k}]_{3,\alpha} &= \left[\sin(\vartheta_q)s^-\left(\frac{2\pi qj}{N}\right)+\cos(\vartheta_q)s^+\left(\frac{2\pi qj}{N}\right),0,\sin(\vartheta_q)c^-\left(\frac{2\pi qj}{N}\right)+\cos(\vartheta_q)c^+\left(\frac{2\pi qj}{N}\right),0\right]\\ [\tilde{A}_{j,k}]_{4,\alpha} &= \left[0,\sin(\vartheta_{-q})s^-\left(-\frac{2\pi qj}{N}\right)+\cos(\vartheta_{-q})s^+\left(-\frac{2\pi qj}{N}\right),0,\sin(\vartheta_{-q})c^-\left(-\frac{2\pi qj}{N}\right)+\cos(\vartheta_{-q})c^+\left(-\frac{2\pi qj}{N}\right)\right.\end{aligned}$$

with

$$c^\pm(x)=\cos(x\pm\pi/4)\,,\qquad s^\pm(x)=\sin(x\pm\pi/4)\,. \tag{7.85}$$

Now, the covariance matrix of a TFD state corresponding to the diagonal Hamiltonian (7.76) is immediate to compute. In the basis of the Majorana modes ψ_j, ordered as in (7.82), it reads (a similar calculation was performed in Ref. [232])

$$\Omega(t,\beta)=\bigoplus_k\Omega_k(t,\beta)\,, \tag{7.86}$$

with

$$\Omega_k(t,\beta) = \tag{7.87}$$

$$\begin{pmatrix} 0 & \sin[2\varphi(k)]\sin[\varepsilon(k)t] & \cos[2\varphi(k)] & \sin[2\varphi(k)]\cos[\varepsilon(k)t] \\ -\sin[2\varphi(k)]\sin[\varepsilon(k)t] & 0 & -\sin[2\varphi(k)]\cos[\varepsilon(k)t] & \cos[2\varphi(k)] \\ -\cos[2\varphi(k)] & \sin[2\varphi(k)]\cos[\varepsilon(k)t] & 0 & -\sin[2\varphi(k)]\sin[\varepsilon(k)t] \\ -\sin[2\varphi(k)]\cos[\varepsilon(k)t] & -\cos[2\varphi(k)] & \sin[2\varphi(k)]\sin[\varepsilon(k)t] & 0 \end{pmatrix}, \tag{7.88}$$

and

$$\varphi(k) = \arctan(e^{-\beta\varepsilon(k)/2})\,. \tag{7.89}$$

Putting all together, we arrive at the following result for the covariance matrix of the TFD state corresponding to the Hamiltonian (7.25):

$$\Gamma(t,\beta) = A\Omega(t,\beta)A^T\,. \tag{7.90}$$

Chapter 8

Growth of Rényi Entropies in Interacting Integrable Models and the Breakdown of the Quasiparticle Picture

In this chapter we investigate the dynamics of Rényi entropies in one-dimensional quantum many-body systems using a radically different approach. Our main idea is to argue that, if the roles of space and time are exchanged, the slope of a given Rényi entropy is mapped to the density of the same entropy in an appropriate steady state. This essentially means that the exchange of space and time — which we dub "spacetime swap" — maps the calculation of a non-equilibrium quantity into that of an equilibrium one.

To demonstrate the validity of aforementioned correspondence under spacetime swap we begin considering locally interacting systems in discrete space time: the so called local quantum circuits. Indeed, as recently pointed out in Ref. [256], in these systems the correspondence can be established rigorously using the spacetime duality method introduced in Ref. [70] (see also [71, 64] for further developments). In particular, for dual-unitary circuits [257], where the dynamics from a class of compatible initial states [70, 71] are essentially invariant under the exchange of space and time, one has that the slope of a given Rényi entropy coincides with the entropy density of the infinite-temperature state — the stationary state of the space evolution.

Then we consider another class of systems where the dynamics are essentially invariant under an appropriate spacetime swap: relativistic quantum field theories. In this case we show that the correspondence holds in the free case. Assuming that it continues to hold for interacting integrable quantum field theories [258, 259, 197] when evolving from appropriate compatible initial states [260], we arrive at a formula for the slope of Rényi entropies in all such systems.

Finally we extend our result to *all* interacting integrable models treatable by thermodynamic Bethe ansatz (TBA) [261, 251, 262, 259, 263] and evolving from compatible

initial states [79]. A significant physical insight of our result is that, as for the special case of Ref. [64], the dynamics of Rényi entropies cannot be understood in terms of a consistent quasiparticle picture.

The rest of this manuscript is laid out as follows. In Sec. 8.1 we define more precisely the setting considered and the quantities relevant for our analysis. In Sec. 8.2 we demonstrate the correspondence of slopes and densities of Rényi entropies under space-time swap in local quantum circuits, where the discreteness of spacetime allows for a rigorous treatment. In Sec. 8.3 we discuss the case of relativistic quantum field theories. In particular, in Sec. 8.3.2 we present our exact formula for the slope of all Rényi entropies in interacting integrable quantum field theories. In Sec. 8.4 we derive a direct generalisation of this result to describe general TBA-integrable systems, and test it against exact analytical and numerical results. Finally, Sec. 8.5 contains a discussion of our results, in particular in relation with the quasiparticle picture, and our conclusions. A number of technical points are relegated to the appendices.

8.1 Setting

In this work we consider a quantum many-body system prepared in a non-equilibrium initial state, $|\Psi_0\rangle$, which is pure and has low entanglement. At time $t = 0$ we let the system evolve under its own unitary dynamics, so that the state at time $t > 0$ is given by

$$|\Psi_t\rangle = \mathbb{U}^t |\Psi_0\rangle , \tag{8.1}$$

where $\mathbb{U}$ is the time-evolution operator. As a result of the unitary evolution the state becomes increasingly more entangled as time advances [210]. The entanglement between a finite region A and the rest of the system can be quantified computing the *Rényi entropies*

$$S_A^{(\alpha)}(t) = \frac{1}{1-\alpha} \ln \left[\operatorname{tr} \rho_A^\alpha(t) \right] , \qquad \alpha \in \mathbb{R} , \tag{8.2}$$

where $\rho_A(t)$ is the density matrix of the system reduced to the subsystem A. In the limit $\alpha \to 1$ the above expression is reduced to the von Neumann entanglement entropy

$$S_A(t) = \lim_{\alpha \to 1} S_A^{(\alpha)}(t) = - \operatorname{tr} \left[\rho_A(t) \ln \rho_A(t) \right] . \tag{8.3}$$

At times that are short compared to the subsystem size $|A|$, Rényi entropies are expected to grow linearly (at least in the systems of interest here), while at sufficiently large times they saturate to their "thermodynamic values", i.e., they coincide with the Rényi entropies of the *stationary state* describing the subsystem A. These two regimes can be respectively characterised by the *entanglement slope* s_α, and the *stationary entanglement density* d_α.

The density d_α is defined as the density of Rényi-α entanglement entropy of a finite subsystem of a thermodynamically large system in the $t \to \infty$ limit, i.e.,

$$d_\alpha = \lim_{|A| \to \infty} \lim_{t \to \infty} \left(\lim_{L \to \infty} \frac{S_A^{(\alpha)}}{|A|} \right) , \tag{8.4}$$

where $|A|$ is the size of the subsystem A and L that of the total system. The final $|A| \to \infty$ limit is taken to remove the boundary effects and focus on the bulk physics of the subsystem A.

The asymptotic slope s_α, sometimes also referred to as "entanglement production rate", is defined as the ratio of the Rényi-α entanglement between a large subsystem and the rest, and time

$$s_\alpha = \lim_{t\to\infty} \lim_{|A|\to\infty} \left(\lim_{L\to\infty} \frac{S_A^{(\alpha)}}{2t} \right), \tag{8.5}$$

where the factor of 2 accounts for the fact that the subsystem A has two edges through which it develops correlations with its complement. In analogy with the density, we take the $t \to \infty$ limit to remove finite-time effects.

Our main goal is to establish a formal connection between the slope and the density based on a spacetime swap, i.e., an exchange of space and time.

8.2 Spacetime swap for local quantum circuits

A convenient setting for our analysis is that of *local quantum circuits*. These are models in discrete space where the time evolution occurs in discrete steps through local updates. The discreteness of time-evolution and the locality of interactions imply that these systems are *closed* under spacetime swap. Namely the "dual system" obtained exchanging the roles of space and time in a quantum circuit is still a quantum circuit, although the unitarity of the time evolution is generically not preserved [264]. This simple observation gives a tool to analyse several properties of quantum circuits by "evolution in space" [265, 257, 70, 264, 266, 267]. In particular, as we now discuss, it can be used to write explicit expressions for the entanglement slope that closely resemble those for the density [70, 64, 268].

For the sake of clarity we consider *brickwork* circuits — i.e., circuits consisting of two-site gates applied to first even and then odd pairs of neighbouring sites — but with minor modifications the argument can be repeated for any discrete-spacetime model with local unitary interactions.

More specifically we consider a chain of $2L$ sites, hosting qudits with d internal states, and where the time evolution operator $\mathbb{U}_L$ is written as the tensor product of L two-site unitary gates U multiplied by the same product shifted by one site, i.e.,

$$\mathbb{U}_L = \Pi_{2L}^\dagger U^{\otimes L} \Pi_{2L} \cdot U^{\otimes L}, \tag{8.6}$$

where Π_{2L} represents a periodic shift by one site on a chain of $2L$ sites. At time t the reduced density matrix of a subsystem A is given by

$$\rho_A = \mathrm{tr}_{\bar{A}}\, \Psi_t \Psi_t = \mathrm{tr}_{\bar{A}} \left(\mathbb{U}^t \Psi_0 \Psi_0\, \mathbb{U}^{\dagger\, t} \right), \tag{8.7}$$

where we repeatedly apply the time-evolution operator $\mathbb{U}$ to the initial state, and then trace over the rest of the system $\bar{A}$. This can be represented graphically as a $2L \times 4t$ tensor network, see Fig. 8.1.

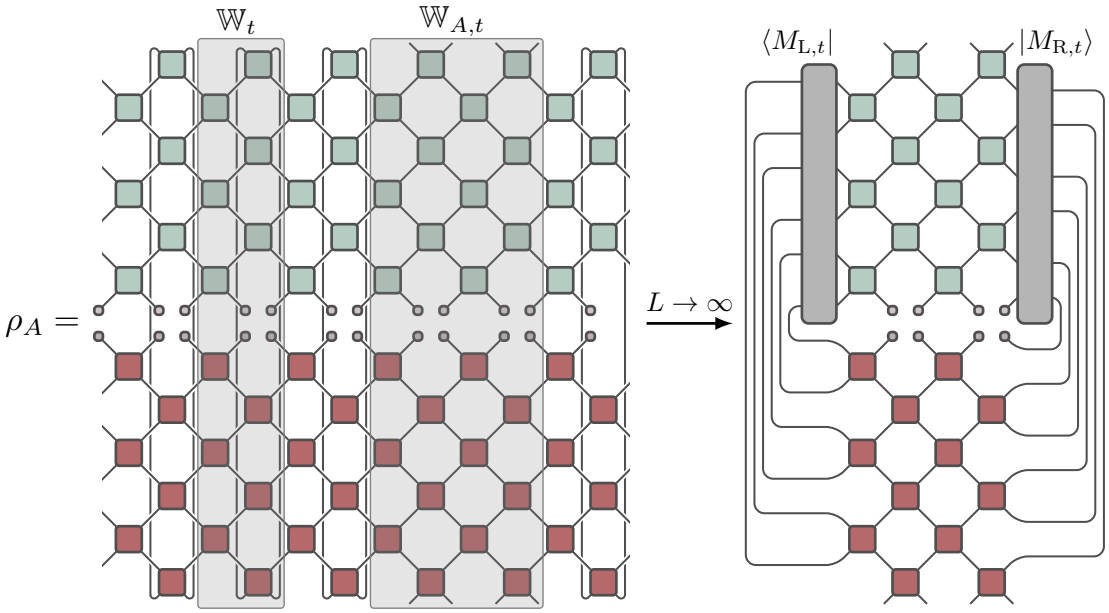

Figure 8.1: Diagrammatic representation of the reduced density matrix. The reduced density matrix ρ_A is obtained by evolving an initial state in time and tracing over the complement $\overline{A}$ of the subsystem A (graphically denoted by connecting the top and bottom legs). Alternatively, we can understand it as a trace of a product of powers of the space transfer matrix $\mathbb{W}_t$ and the transfer matrix $\mathbb{W}_{A,t}$ (both shaded in grey), as given by Eq. (8.8). In the limit $L \to \infty$, the section of the tensor network corresponding to the rest of the system can be replaced by fixed-points $\langle M_{\mathrm{L},t}|$ and $|M_{\mathrm{R},t}\rangle$ of the space transfer matrix $\mathbb{W}_t$ (cf. Eq. (8.10)).

The same tensor network can be equivalently thought of as resulting from an evolution in *space*. Indeed, rather than viewing gates as acting on the $2L$ sites arranged horizontally and propagating upwards/downwards, one can imagine them acting on the $4t$ sites arranged vertically and propagating rightwards/leftwards. To this end we introduce two different *space transfer matrices* playing the role of evolution operators in space (cf. Fig. 8.1): $\mathbb{W}_t$, that describes the space evolution in the complement of the subsystem $\overline{A}$, and $\mathbb{W}_{A,t}$, that acts both on $4t$ *temporal* sites and on the subsystem A. Using these definitions, we can express the reduced density matrix ρ_A as the trace of a large power of $\mathbb{W}_t$ multiplied by $\mathbb{W}_{A,t}$, i.e.,

$$\rho_A = \mathrm{tr}\left(\mathbb{W}_t^{L-|A|}\mathbb{W}_{A,t}\right). \tag{8.8}$$

Due to the unitarity of the time-evolution (see, e.g., [71, 63, 269, 270, 271]) the transfer matrix $\mathbb{W}_t$ has a single non-degenerate eigenvalue 1, while all the other eigenvalues are 0. The latter generically correspond to nontrivial Jordan blocks of size smaller or equal to t. Therefore, when L is sufficiently larger than t, the matrix power

$$\mathbb{W}_t^{L-|A|} \tag{8.9}$$

can be replaced with a projector on the *fixed points* $|M_{\mathrm{L},t}\rangle$ and $|M_{\mathrm{R},t}\rangle$, i.e., the left and right eigenvectors corresponding to eigenvalue 1 [269, 270, 271]. Namely

$$\lim_{L\to\infty}\rho_A = \langle M_{\mathrm{L},t}|\, W_{A,t}\, |M_{\mathrm{R},t}\rangle\,, \tag{8.10}$$

where we chose the normalisation such that

$$\langle M_{\mathrm{L},t}\,|M_{\mathrm{R},t}\rangle = 1\,. \tag{8.11}$$

Eq. (8.10) shows that the fixed points completely capture the effect of $\bar{A}$ on the finite subsystem A (cf. Fig. 8.1). For this reason, and to stress their connection with the Feynman-Vernon influence functional, Ref. [272] (see also [273, 274, 275, 276]) proposed to dub them *influence matrices*.

The fixed points $|M_{\mathrm{L},t}\rangle$ and $|M_{\mathrm{R},t}\rangle$ can be thought of both as vectors in the space of $4t$ temporal sites, or as matrices $M_{\mathrm{L},t}$, $M_{\mathrm{R},t}$ mapping from $2t$ temporal sites in the top half to $2t$ sites in the bottom half [2] (see r.h.s. of Fig. 8.1 for an illustration). The latter perspective makes fixed points convenient to access s_α.

To demonstrate this we begin by observing that, for n integer, $\mathrm{tr}\,\rho_A^n$ can be represented as n copies of conjugate pairs of the time-evolved initial state that are coupled in a staggered fashion. In the section corresponding to $\overline{A}$ the pairs are connected, while in A the conjugate copy of a pair is connected to the non-conjugate copy of the next pair — see the left panel of Fig. 8.2 for a pictorial representation. This means that $\mathrm{tr}\,[\rho_A^n(t)]$ can be expressed in terms of products of n copies of the space transfer matrix $\mathbb{W}_t$ as

$$\mathrm{tr}\,[\rho_A^n(t)] = \mathrm{tr}\left[\left(\mathbb{W}_t^{\otimes n}\right)^{|\overline{A}|/2}\eta_{2n}^\dagger\left(\mathbb{W}_t^{*\otimes n}\right)^{|A|/2}\eta_{2n}\right], \tag{8.12}$$

[2] By this definition, $\langle M_{\mathrm{L/R},t}|$ correspond to $M_{\mathrm{L/R},t}^*$, and $M_{\mathrm{L/R},t}^\dagger = M_{\mathrm{L/R},t}$.

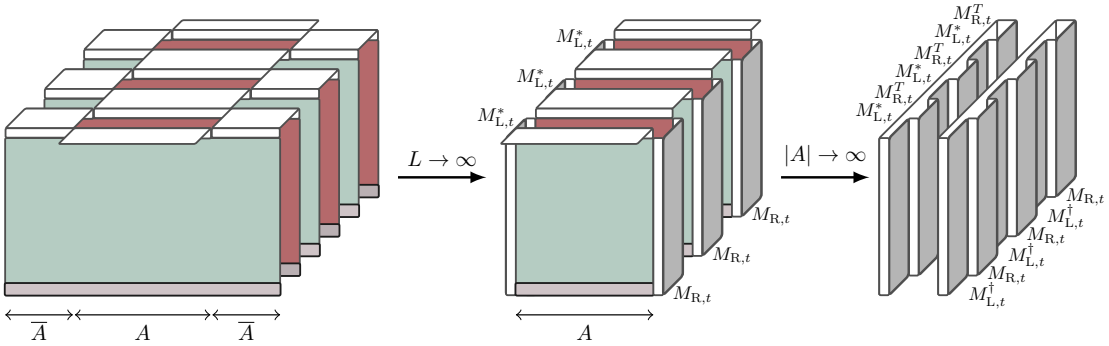

Figure 8.2: Schematic illustration of $\mathrm{tr}\left[\rho_A^3\right]$. Green and red rectangles are condensed representation of the green and red half of the time-evolution from Fig. 8.1. The white connections on the left represent trace over the rest of the system, while the connections on the right correspond to matrix products and then an overall trace. In the limit of large $L - |*|A$ the left and right parts of $\overline{A}$ can be substituted by fixed points $M^*_{\mathrm{L},t}$ and $M_{\mathrm{R},t}$ connecting pairs of time-sheets. Analogously, when the subsystem size becomes large, the section in the middle can be replaced with fixed points $M^\dagger_{\mathrm{L},t}$, and $M^T_{\mathrm{R},t}$. Note the additional transpose of fixed points, which is the consequence of connecting the opposite parity of pairs of neighbours. Thus we obtain the right-most diagram, which corresponds precisely to the r.h.s. of Eq. (8.13).

where η_{2n} represents a shift for one copy in the space of $2n$ replicas, and the complex conjugate of the transfer matrix comes from the exchange of conjugate and non-conjugate copies (cf. Fig. 8.2).

For $L - |A|$ and $|A|$ both much larger than t the powers of the transfer matrix can again be replaced by the fixed points. In this way we obtain

$$\lim_{|A|\to\infty} \lim_{L\to\infty} \mathrm{tr}\left[\rho_A^n(t)\right] = \mathrm{tr}\left[(M^\dagger_{\mathrm{L},t} M_{\mathrm{R},t})^n\right]^2, \tag{8.13}$$

which is schematically depicted on the r.h.s. of Fig. 8.2. Thus, we find the following succinct expression for the slope (8.5)

$$s_\alpha = \frac{1}{1-\alpha} \lim_{t\to\infty} \frac{1}{t} \ln \mathrm{tr}\left[(M^\dagger_{\mathrm{L},t} M_{\mathrm{R},t})^\alpha\right], \quad \alpha \in \mathbb{R}, \tag{8.14}$$

where we analytically continued the matrix power.

On the other hand, the stationary entropy density (8.4) is expected to coincide with the Rényi entropy of the reduced density matrix of the stationary state, i.e.,

$$d_\alpha = \frac{1}{1-\alpha} \lim_{|A|\to\infty} \frac{1}{|A|} \ln \mathrm{tr}\left[\rho^\alpha_{\mathrm{st},A}\right]. \tag{8.15}$$

A comparison between the expressions (8.14) and (8.15) shows that the slope can be written as a density of Rényi entropy as follows

$$s_\alpha = \frac{1}{1-\alpha} \lim_{t\to\infty} \frac{1}{t} \ln \mathrm{tr}\left[\tilde{\rho}^\alpha_{\mathrm{st},t}\right], \tag{8.16}$$

where we introduced the *pseudo density matrix*

$$\tilde{\rho}_{\mathrm{st},t} = M_{\mathrm{L},t}^{\dagger} M_{\mathrm{R},t}. \tag{8.17}$$

To gain physical intuition on the meaning of $\tilde{\rho}_{\mathrm{st},t}$ let us begin considering $M_{\mathrm{L},t}$ and $M_{\mathrm{R},t}$. These matrices are by definition the fixed points, or stationary states, of the space evolution (from left to right and right to left respectively). Moreover, as shown in Appendix 8.A, they fulfil

$$M_{\mathrm{R},t} = m_{\mathrm{R},t} m_{\mathrm{R},t}^{\dagger}\,, \qquad\qquad M_{\mathrm{L},t} = m_{\mathrm{L},t} m_{\mathrm{L},t}^{\dagger}, \tag{8.18}$$

implying that they are Hermitian and positive. This fact can be understood by recalling that, although not unitary, the evolution in space is a *hybrid quantum evolution* [264], i.e., it preserves positivity and Hermiticity.

Eq. (8.18) guarantees that $\tilde{\rho}_{\mathrm{st},t}$ has real, non-negative eigenvalues, and, moreover, the normalisation condition (8.11) gives

$$\operatorname{tr} \tilde{\rho}_{\mathrm{st},t} = 1\,. \tag{8.19}$$

Combining all the above facts together we see that, even though $\tilde{\rho}_{\mathrm{st},t}$ is not Hermitian and hence it cannot be interpreted as a proper quantum mechanical density matrix, it has many properties of reduced density matrices.

We note that a correspondence similar to (8.16) between entanglement slope in the original model and "steady-state entanglement" in the dual model has been recently discovered in Ref. [256]. Here, however, we provided two significant advances. First, we showed how to establish the correspondence for purely unitary evolution of the original model, without introducing the edge decoherence considered in Ref. [256]. Second, we provided a direct expression of $\tilde{\rho}_{\mathrm{st},t}$ in terms of the fixed points of the space transfer matrix (or influence matrices).

In the special case when right and left fixed points coincide, $\tilde{\rho}_{\mathrm{st},t}$ is Hermitian, positive definite, normalised to one, and invariant under the space evolution. Therefore, it is a stationary density matrix of the space evolution. This happens, for instance, for *dual-unitary quantum circuits* [257] evolving from compatible — or solvable — initial states [70, 71]. Indeed, these systems and states are designed in such a way that the evolution in space is again a unitary brickwork quantum circuit, and, therefore, is equivalent to the time evolution. In particular, we have [70, 71]

$$M_{\mathrm{R},t} = M_{\mathrm{L},t} = \frac{\mathbb{1}_{2t}}{d^t}, \tag{8.20}$$

where $\mathbb{1}_x$ is the identity matrix acting on x qudits. Therefore, in this case the pseudo density matrix coincides with the infinite temperature state, i.e.,

$$\tilde{\rho}_{\mathrm{st},t} = \frac{\mathbb{1}_{2t}}{d^{2t}}\,. \tag{8.21}$$

Note that this is indeed the stationary state reached by the subsystem $[0, t]$ of the time lattice under space evolution. Thus, for dual-unitary circuits (8.16) is rewritten as

$$s_\alpha = \tilde{d}_\alpha, \tag{8.22}$$

where $\tilde{d}_\alpha$ in (8.16) is the stationary density of entropy in the dual model. For dual-unitary circuits one can also repeat the above reasoning to compute the entanglement growth between a subsystem of the time lattice and the rest. This gives

$$\tilde{s}_\alpha = d_\alpha \,. \tag{8.23}$$

8.3 Spacetime swap in relativistic quantum field theories

Let us now change the setting and consider quantum field theories in 1+1 dimensions, i.e., generic quantum systems defined in a continuous spacetime. Since in these systems space and time are both continuous they are again closed under spacetime swap. Therefore, we expect that one can again establish a direct correspondence between slope and density of Rényi entropies.

In 1+1 dimensional quantum field theories, however, it is more convenient to perform a slight variation of the spacetime swap. Specifically, instead of directly exchanging space and time here we consider the following analytic continuation

$$(t, x) \mapsto (-ix, it), \tag{8.24}$$

which corresponds to an exchange of space and time in the Euclidean formulation of the theory [259]. In the string-theory literature the dual model obtained via the mapping (8.24) is often referred to as the *mirror model* [277, 278, 263].

Our key observation is that if one considers a 1+1 dimensional relativistic invariant quantum field theory, crossing symmetry implies that the mirror model coincides with the original one in the bulk. Therefore, in this setting 1+1 dimensional relativistic quantum field theories play a role similar to the dual-unitary circuits considered in the previous section. This means that, assuming appropriate compatible initial states, one should have

$$s_\alpha = i\tilde{d}_\alpha, \qquad d_\alpha = -i\tilde{s}_\alpha \,, \tag{8.25}$$

where the quantities with the tilde denote the slope and density of Rényi entropy in the mirror model. To be more concrete and gain some intuition we begin by proving (8.25) for non-interacting, fermionic 1+1 dimensional quantum field theories.

8.3.1 Proof of (8.25) for free theories

Let us focus on a non-interacting quantum field theory of fermions in 1+1 dimensions. We consider the quench problem with the system initially prepared in the Gaussian state

$$|\Psi_0\rangle = \exp\left(\int \frac{\mathrm{d}\theta}{2\pi} K(\mu)\psi^\dagger(-\mu)\psi^\dagger(\mu)\right)|0\rangle \,, \tag{8.26}$$

where $\psi^\dagger(\mu)$ is a creation operator for fermionic modes of rapidity μ, $|0\rangle$ is the vacuum state for fermions, and $K(\mu)$ is an odd function such that

$$\int \frac{\mathrm{d}\mu}{2\pi}|K(\mu)|^2 < \infty\,. \tag{8.27}$$

Since a state of the form (8.26) produces pairs of correlated quasiparticles, the asymptotic slope (8.5) can be computed using the quasiparticle picture [41]

$$s_\alpha = \frac{2m}{1-\alpha}\int_0^\infty \frac{\mathrm{d}\mu}{2\pi}\,\sinh\mu\,\ln\left[(1-\vartheta(\mu))^\alpha+\vartheta(\mu)^\alpha\right]. \tag{8.28}$$

Here

$$\vartheta(\mu) = \frac{1}{1+|K(\mu)|^2} = \vartheta(-\mu), \tag{8.29}$$

is the *occupation*, or *filling* function, of the free mode with rapidity μ and we used the explicit form of the relativistic dispersion relation

$$\varepsilon(\mu) = m\cosh\mu, \qquad p(\mu) = m\sinh\mu\,, \tag{8.30}$$

where m is the mass of the fermions and we set the speed of light to one. Next, we recall that for a stationary state described by a filling function $\vartheta(\mu)$ the density of Renyi entropy reads as

$$d_\alpha = \frac{2m}{1-\alpha}\int_0^\infty \frac{\mathrm{d}\mu}{2\pi}\,\cosh\mu\,\ln\left[(1-\vartheta(\mu))^\alpha+\vartheta(\mu)^\alpha\right]. \tag{8.31}$$

We then proceed by observing that at the level of rapidities the transformation (8.24) becomes [263]

$$\mu \mapsto i\frac{\pi}{2} - \mu, \tag{8.32}$$

therefore in the mirror model the occupation corresponding to $\vartheta(\mu)$ reads as

$$\tilde\vartheta(\mu) = \vartheta(i\tfrac{\pi}{2} - \mu). \tag{8.33}$$

Plugging this definition into the equation for the slope (8.28) we have

$$\begin{aligned} s_\alpha &= \frac{2m}{1-\alpha}\int_0^\infty \frac{\mathrm{d}\mu}{2\pi}\,\sinh\mu\,\ln\Big[(1-\tilde\vartheta(i\tfrac{\pi}{2}-\mu))^\alpha+\tilde\vartheta(i\tfrac{\pi}{2}-\mu)^\alpha\Big] \\ &= \frac{2im}{1-\alpha}\int_\Gamma \frac{\mathrm{d}\mu}{2\pi}\,\cosh\mu\,\ln\Big[(1-\tilde\vartheta(\mu))^\alpha+\tilde\vartheta(\mu)^\alpha\Big], \end{aligned} \tag{8.34}$$

where Γ is the positively oriented contour parametrised by $i\frac{\pi}{2} - x$ with $x \le 0$. Comparing (8.34) with (8.31) we see that the former can be interpreted as the density of entropy in the mirror model times i. We note that in the mirror model the integration is performed over Γ to keep $\tilde\vartheta(x)$ well defined and rapidly decaying.

Analogously, substituting the definition (8.33) into the expression for the density (8.31) we see that the density of entropy in the original model can be interpreted as $-i$ times the slope of the mirror model

$$d_\alpha = \frac{-2im}{1-\alpha}\int_\Gamma \frac{\mathrm{d}\mu}{2\pi}\,\sinh\mu\,\ln\Big[(1-\tilde\vartheta(\mu))^\alpha+\tilde\vartheta(\mu)^\alpha\Big]. \tag{8.35}$$

8.3.2 Slope of Rényi entropies in interacting integrable theories

Our next step is to use the correspondence (8.25) to find a prediction for the slope in the presence of interactions. To this end, a convenient setting to consider is that of massive integrable quantum field theories with a single species of excitations. We consider integrable quantum systems because for these systems the stationary density can be computed exactly using the *quench action* approach [212], while we focus on theories with a single species of particle excitations for simplicity. Note that for this family of integrable quantum field theories, a similar argument based on the mapping (8.24) has been employed in Ref. [279] to compute the expectation values of currents in stationary states.

In integrable quantum field theories the scattering is elastic and completely factorised. Therefore, it is fully determined by the two-particle scattering matrix $S(\mu)$. This is a meromorphic function of the rapidity in the *physical strip* $\mathcal{S} = \{0 \leq \mathrm{Im}\,\mu \leq \pi\}$, fulfilling *unitarity*, *crossing symmetry*, and *real analyticity*

$$S(\mu)S(-\mu) = 1, \qquad \mu \in \mathcal{S}, \tag{8.36}$$
$$S(\mu) = S(i\pi - \mu), \qquad \mu \in \mathcal{S}, \tag{8.37}$$
$$S(\mu)^* = S(-\mu), \qquad \mu \in \mathbb{R}, \tag{8.38}$$
$$S(i\mu)^* = S(i\mu), \qquad \mu \in [0, \pi]. \tag{8.39}$$

A powerful method to describe the thermodynamics of interacting integrable theories is provided by the *thermodynamic Bethe ansatz* (TBA) [259]. In essence, with this method one describes stationary macrostates specifying the density of particle excitations that they contain. This is possible because in these systems particle excitations are stable and hence their densities are conserved.

In particular, we can again describe macrostates using the filling function $\vartheta(\mu)$, which describes the fraction of available states that are occupied by the particles. Now, however, the density of available states, denoted by $\rho_t(\mu)$, is *not* a simple Jacobian as in the non-interacting case. Because of the interactions it depends on the filling function through the following integral equation [259]

$$\rho_t(\mu) = \frac{m}{2\pi}\cosh(\mu) + \int \frac{\mathrm{d}\mu'}{2\pi} T(\mu - \mu')\rho_t(\mu')\vartheta(\mu'). \tag{8.40}$$

Here we introduced the *scattering kernel* $T(\mu)$, which is given by the logarithmic derivative of the scattering matrix

$$T(\mu) = -i\frac{\mathrm{d}}{\mathrm{d}\mu}\ln S(\mu)\,. \tag{8.41}$$

Since we are considering theories evolving from non-equilibrium initial states, the mirror model will have a nontrivial boundary in space. Here we are interested in the case where this boundary does not break the integrability of the theory, so that we can use the result of Ref. [212] for the density of Rényi entropy, therefore, we have to consider

initial states generating integrable boundary conditions. These states are well known in the context of quantum integrability, and they are typically referred to as integrable boundary states [260]. Note that integrable boundary states need regularisation to be considered as initial states of quench problems [280, 281, 282, 284, 285]. This is essentially due to the fact that they give non-zero weight to configurations involving particles with infinite energy.

A regularised integrable boundary state can be thought of as the generalisation of (8.26). It is obtained by replacing $\psi^\dagger(\mu)$ with the operators creating the stable excitations [258] and requiring $K(\mu)$ to satisfy

$$K(\mu) = S(2\mu)K(-\mu), \tag{8.42}$$

instead of being odd. The filling function corresponding to such a state is then obtained as the solution to the following integral equation [280, 282]

$$\ln\frac{\vartheta(\mu)}{1-\vartheta(\mu)} = \ln|K(\mu)|^2 - \int\frac{\mathrm{d}\mu'}{2\pi}T(\mu'-\mu)\ln\big[1-\vartheta(\mu')\big]\,. \tag{8.43}$$

Note that (8.38) and (8.42) imply that $\vartheta(\mu)$ is even.

Having introduced the necessary formalism we are finally in a position to write an expression for s_α. Our starting point is the exact expression for d_α in interacting integrable models derived in Ref. [212]. Specialising it to the case at hand we can express it as

$$d_\alpha = \frac{2m}{1-\alpha}\int_0^\infty\frac{\mathrm{d}\mu}{2\pi}\,\cosh\mu\,\ln\left[(1-\vartheta(\mu))^\alpha + \frac{\vartheta(\mu)^\alpha}{x_\alpha(\mu)}\right], \tag{8.44}$$

where the auxiliary function $x_\alpha(\mu)$ is the solution to the following integral equation

$$\begin{aligned}\ln x_\alpha(\lambda) = \int_0^\infty \mathrm{d}\mu\;&(T(\mu-\lambda)+T(\mu+\lambda))\\ &\times\ln\left[(1-\vartheta(\mu))^\alpha + \frac{\vartheta(\mu)^\alpha}{x_\alpha(\mu)}\right].\end{aligned} \tag{8.45}$$

Proceeding as in the free case by substituting the definition (8.33) of $\tilde\vartheta(\mu)$ in (8.44) we find

$$d_\alpha = \frac{-2i}{1-\alpha}\int_\Gamma\frac{\mathrm{d}\mu}{2\pi}\,\sinh\mu\,\ln\left[(1-\tilde\vartheta(\mu))^\alpha + \frac{\tilde\vartheta(\mu)^\alpha}{\tilde y_\alpha(\mu)}\right], \tag{8.46}$$

where we defined

$$\tilde y_\alpha(\lambda) = x_\alpha(i\tfrac{\pi}{2}-\lambda). \tag{8.47}$$

The latter fulfils the following integral equation

$$\begin{aligned}\ln\tilde y_\alpha(\lambda) = \int_\Gamma \mathrm{d}\mu\;&(T(\mu-\lambda)-T(\mu+\lambda))\\ &\times\ln\left[(1-\tilde\vartheta(\mu))^\alpha + \frac{\tilde\vartheta(\mu)^\alpha}{\tilde y_\alpha(\mu)}\right].\end{aligned} \tag{8.48}$$

Where we used that, because of the crossing symmetry (8.37) of the scattering matrix, the kernel satisfies the following relation,

$$T(i\pi + \mu) = -T(\mu)\,. \tag{8.49}$$

Using then the correspondence (8.25) and rewriting everything for the original model we finally find

$$s_\alpha = \frac{2}{1-\alpha}\int_0^\infty \frac{\mathrm{d}\mu}{2\pi}\,\sinh\mu\,\ln\left[(1-\vartheta(\mu))^\alpha + \frac{\vartheta(\mu)^\alpha}{y_\alpha(\mu)}\right] \tag{8.50}$$

with

$$\begin{aligned}\ln y_\alpha(\lambda) = \int_0^\infty \mathrm{d}\mu\;(T(\mu-\lambda) - T(\mu+\lambda)) \\ \times \ln\left[(1-\vartheta(\mu))^\alpha + \frac{\vartheta(\mu)^\alpha}{y_\alpha(\mu)}\right].\end{aligned} \tag{8.51}$$

This concludes our derivation of s_α for interacting integrable quantum field theories with diagonal scattering.

8.4 Slope of Rényi entropies in generic TBA-integrable models

The argument leading to Eq. (8.50) can be applied to a much larger class of TBA-solvable models. An immediate generalisation is obtained by considering integrable quantum field theories with non-diagonal scattering as the sine-Gordon field theory. Indeed, since integrable boundary states also exist for these systems [260], one can directly repeat the treatment of the previous section.

In fact, the existence of integrable boundary states is not limited to field theories. Also in algebraic-Bethe-ansatz-integrable lattice systems there exist initial states for which the system obtained by exchanging space and time is integrable [286, 79, 287, 288, 80]. This applies most directly to integrable systems with a discrete time evolution [315]. In these systems the time evolution is generated by an integrable transfer matrix and, by taking appropriate initial states [286, 79, 287, 288, 80], one can ensure integrability of the (boundary) transfer matrix in space [289]. The case of lattice systems with continuous time evolution can then be recovered by taking the *Trotter limit* [252, 253],i.e., sending the discrete time-step Δt to zero, while keeping fixed the real time $t = N \cdot \Delta t$ with N being the number of steps.

In light of these facts here we argue that Eq. (8.50) can be extended to all TBA-integrable systems by a simple generalisation of the TBA description. In particular we have to account for the following modifications.

(i) Generic integrable models feature multiple species of quasiparticles [262, 259]. This means that in general quasiparticles are no longer specified only by their rapidity

$\lambda \in \mathbb{R}$ but one also needs to introduce a discrete species index $n \in \mathbb{N}$. Effectively, this means that we have to make the replacement

$$\lambda \mapsto (\lambda, n), \tag{8.52}$$

in the arguments of all functions. Naturally, this also means that when integrating over the rapidity, also the sum over all the possible particle species has to be performed

$$\int \mathrm{d}\mu\, f(\mu) \mapsto \sum_m \int \mathrm{d}\mu\, f_m(\mu), \tag{8.53}$$

where we followed the standard convention of reporting the species index in the subscript. Note also that the integration and summation boundaries depend on the specific model. Finally, to describe scattering among particles of different species, the scattering kernel needs to be generalised,

$$T(\lambda - \mu) \mapsto T_{nm}(\lambda, \mu). \tag{8.54}$$

To keep track of rapidity and species index we employ the following compact notation

$$\begin{gathered} (\lambda, n) \equiv \boldsymbol{\lambda}, \\ \sum_m \int \mathrm{d}\mu\, f_m(\mu) \equiv \int \mathrm{d}\boldsymbol{\mu}\, f(\boldsymbol{\mu}), \\ T_{nm}(\lambda, \mu) \equiv T(\boldsymbol{\lambda}, \boldsymbol{\mu}). \end{gathered} \tag{8.55}$$

(ii) In generic TBA integrable systems the dispersion relation does not necessarily coincide with the relativistic one, therefore we make the replacement

$$\cosh\lambda \mapsto \varepsilon(\boldsymbol{\lambda}), \qquad \sinh\lambda \mapsto p(\boldsymbol{\lambda})\,. \tag{8.56}$$

Here the parametrisation is chosen such that $\varepsilon'(\boldsymbol{\lambda}) = \varepsilon_n'(\lambda)$, is always positive for $\lambda > 0$.

Taking into account the modifications (i) and (ii), Eq. (8.50) is rewritten as

$$s_\alpha = \frac{2}{1-\alpha} \int_+ \mathrm{d}\boldsymbol{\mu}\, \frac{\varepsilon'(\boldsymbol{\mu})}{2\pi}\, \ln\left[(1-\vartheta(\boldsymbol{\mu}))^\alpha + \frac{\vartheta(\boldsymbol{\mu})^\alpha}{y_\alpha(\boldsymbol{\mu})}\right], \tag{8.57}$$

where we introduced the auxiliary function

$$\begin{aligned} \ln y_\alpha(\boldsymbol{\lambda}) = \int_+ \mathrm{d}\boldsymbol{\mu}\, &(T(\boldsymbol{\mu}, \boldsymbol{\lambda}) - T(\boldsymbol{\mu}, -\boldsymbol{\lambda})) \\ &\times \ln\left[(1-\vartheta(\boldsymbol{\mu}))^\alpha + \frac{\vartheta(\boldsymbol{\mu})^\alpha}{y_\alpha(\boldsymbol{\mu})}\right]. \end{aligned} \tag{8.58}$$

Here $(\cdot)'$ denotes a derivative with respect to the real rapidity μ and the subscript $+$ indicates that the integral range is restricted to positive rapidities. To express (8.57)

we implicitly used that, apart from fine tuned cases, integrable initial states produce reflection symmetric rapidity distributions [260, 79, 287, 288, 80].

Once again (8.57) closely parallels the expression for the density of Rényi entropy in the post quench stationary state described by the rapidity distribution $\vartheta(\boldsymbol{\mu})$. Indeed, for a reflection-symmetric $\vartheta(\boldsymbol{\mu})$ we have [212]

$$d_\alpha = \frac{2}{1-\alpha}\int_+ \mathrm{d}\boldsymbol{\mu}\, \frac{|p'(\boldsymbol{\mu})|}{2\pi}\, \ln\left[(1-\vartheta(\boldsymbol{\mu}))^\alpha + \frac{\vartheta(\boldsymbol{\mu})^\alpha}{x_\alpha(\boldsymbol{\mu})}\right], \tag{8.59}$$

with

$$\begin{aligned}\ln x_\alpha(\boldsymbol{\lambda}) = \int_+ \mathrm{d}\boldsymbol{\mu}\, &(T(\boldsymbol{\mu},\boldsymbol{\lambda}) + T(\boldsymbol{\mu},-\boldsymbol{\lambda})) \\ &\times \ln\left[(1-\vartheta(\boldsymbol{\mu}))^\alpha + \frac{\vartheta(\boldsymbol{\mu})^\alpha}{x_\alpha(\boldsymbol{\mu})}\right].\end{aligned} \tag{8.60}$$

In what follows we present strong evidence for the validity of (8.57) by providing four nontrivial consistency checks. In particular, in Sec. 8.4.1 we show that Eq. (8.57) reduces to the exact free-fermion result [212] when the interaction kernel vanishes. Next, in Sec. 8.4.2 we prove that in the limit $\alpha \to 1$ the expression recovers the quasiparticle prediction [44] for the slope of the von Neumann entanglement entropy. In Sec. 8.4.3 we show that (8.57) agrees with the exact result of Refs. [62, 64] for a specific interacting integrable model treatable by TBA, i.e., the cellular automaton *Rule 54* [290]. Finally, in Sec. 8.4.4 we compare Eq. (8.57) with exact numerical results for the XXZ spin-1/2 chain.

Before that, however, we rewrite the expression (8.57) in an equivalent form, which is more convenient for parts of the upcoming analysis. To this end, we introduce two quantities that are very convenient in the TBA analysis of integrable systems, namely *total density* $\rho_t(\boldsymbol{\lambda})$ and *dressed velocity* $v(\boldsymbol{\lambda})$. The former is the direct generalisation of the density of available states introduced in Sec. 8.3.2 and is defined as the solution to the following integral equation

$$\rho_t(\boldsymbol{\lambda}) = \frac{|p'(\boldsymbol{\lambda})|}{2\pi} - \int \mathrm{d}\boldsymbol{\mu}\, T(\boldsymbol{\lambda},\boldsymbol{\mu})\vartheta(\boldsymbol{\mu})\rho_t(\boldsymbol{\mu})\,. \tag{8.61}$$

The latter is the velocity of quasiparticle excitations in the state described by $\vartheta(\boldsymbol{\mu})$ and is determined by

$$v(\boldsymbol{\lambda})\rho_t(\boldsymbol{\lambda}) = \frac{\varepsilon'(\boldsymbol{\lambda})}{2\pi} - \int \mathrm{d}\boldsymbol{\mu}\, T(\boldsymbol{\lambda},\boldsymbol{\mu})\vartheta(\boldsymbol{\mu})v(\boldsymbol{\mu})\rho_t(\boldsymbol{\mu})\,. \tag{8.62}$$

This quantity plays a crucial role in the quench dynamics, which was first observed in Ref. [188].

Inserting Eqs. (8.61) and (8.62) into Eqs. (8.59), and (8.57), we obtain the following equivalent expressions for density

$$\begin{aligned}d_\alpha = &\frac{2}{1-\alpha}\int_+ \mathrm{d}\boldsymbol{\mu}\, \rho_t(\boldsymbol{\mu}) \ln\left[(1-\vartheta(\boldsymbol{\mu}))^\alpha + \frac{\vartheta(\boldsymbol{\mu})^\alpha}{x_\alpha(\boldsymbol{\mu})}\right] \\ &+ \frac{2}{1-\alpha}\int_+ \mathrm{d}\boldsymbol{\mu}\, \rho(\boldsymbol{\mu}) \ln x_\alpha(\boldsymbol{\mu}),\end{aligned} \tag{8.63}$$

and slope

$$s_\alpha = \frac{2}{1-\alpha}\int_+ \mathrm{d}\boldsymbol{\mu}\, \rho_t(\boldsymbol{\mu}) v(\boldsymbol{\mu}) \ln\left[(1-\vartheta(\boldsymbol{\mu}))^\alpha + \frac{\vartheta(\boldsymbol{\mu})^\alpha}{y_\alpha(\boldsymbol{\mu})}\right] + \frac{2}{1-\alpha}\int_+ \mathrm{d}\boldsymbol{\mu}\, \rho(\boldsymbol{\mu}) v(\boldsymbol{\mu}) \ln y_\alpha(\boldsymbol{\mu}). \tag{8.64}$$

8.4.1 Free fermions

Our first check concerns free-fermionic systems. In this case, the absence of interactions permits *ab initio* calculations [41, 35, 43, 308], which prove the validity of quasiparticle picture also for Rényi-α entropies. Therefore we expect to recover the quasiparticle result in the limit of the vanishing interaction kernel.

Indeed, for $T(\boldsymbol{\lambda}, \boldsymbol{\mu}) = 0$, Eq. (8.58) gives

$$y(\mu) = 1, \qquad \forall \mu\,, \tag{8.65}$$

and thus (8.57) becomes

$$s_\alpha = \frac{2}{1-\alpha}\int_+ \mathrm{d}\boldsymbol{\mu}\, \frac{\varepsilon'(\boldsymbol{\mu})}{2\pi}\, \ln\left[(1-\vartheta(\boldsymbol{\mu}))^\alpha + \vartheta(\boldsymbol{\mu})^\alpha\right], \tag{8.66}$$

which is precisely the quasiparticle-picture result [212].

8.4.2 Von Neumann

To recover the prediction for the von-Neumann entanglement entropy we consider the limit $\alpha \to 1$ of the expressions (8.64), and (8.58). We begin by noting that

$$y_1(\mu) = 1, \tag{8.67}$$

which follows from the observation that in the $\alpha \to 1$ limit the function $y_1(\mu) = 1$ solves Eq. (8.58), combined with the standard TBA assumption of uniqueness of solutions. Evaluating the limit $\alpha \to 1$ in Eq. (8.64) we then have

$$\lim_{\alpha\to 1} s_\alpha = 2\int_+ \mathrm{d}\boldsymbol{\mu}\, v(\boldsymbol{\mu}) s(\boldsymbol{\mu}). \tag{8.68}$$

Here we used that the terms containing $\partial_\alpha y_\alpha(\mu)$ cancel, and introduced $s(\boldsymbol{\mu})$ for the density of the Yang-Yang entropy,

$$s(\boldsymbol{\mu}) = -\rho_t(\boldsymbol{\mu})[(1-\vartheta(\boldsymbol{\mu}))\ln(1-\vartheta(\boldsymbol{\mu})) + \vartheta(\boldsymbol{\mu})\ln\vartheta(\boldsymbol{\mu})]. \tag{8.69}$$

As promised, (8.68) recovers the quasiparticle prediction [44] for the slope of the von Neumann entanglement entropy.

Figure 8.3: Schematic representation of time evolution of Rule 54. In each time-step the three-site gates U are applied either to even ($\mathbb{U}_L^{\mathrm{e}}$) or odd ($\mathbb{U}_L^{\mathrm{o}}$) triplets of sites. Note that gates that overlap on at most one site commute.

8.4.3 Rule 54

Our next consistency check involves what is so far the only known exact result for the slope of Rényi entropies in an interacting integrable system: the result of Refs. [62, 64] for the Rule 54 cellular automaton. The model was introduced in Ref. [290], and has recently been identified as one of the simplest examples of interacting integrable systems [291], allowing for the exact description of many non-equilibrium properties, both in the classical [292, 293, 294, 295, 296, 297, 298], and the quantum realm [299, 300, 301, 302, 303, 304, 62, 63, 64, 305].

Rule 54 can be understood as a quantum circuit consisting of 3-site local *deterministic* gates U with the following matrix elements,

$$U_{s_1 s_2 s_3}^{s_1' s_2' s_3'} = \delta_{s_1',s_1}\delta_{s_2',\chi(s_1,s_2,s_3)}\delta_{s_3',s_3}, \tag{8.70}$$

where we introduced the binary function $\chi : \mathbb{Z}_2^{\times 3} \to \mathbb{Z}_2$

$$\chi(s_1, s_2, s_3) \equiv s_1 + s_2 + s_3 + s_1 s_3 \pmod 2. \tag{8.71}$$

Time-evolution is given in two distinct time-steps

$$\mathbb{U}_L = \mathbb{U}_L^{\mathrm{o}}\mathbb{U}_L^{\mathrm{e}}, \tag{8.72}$$

which involve the gates U applied at odd or even triplets of sites (see Fig. 8.3 for an illustration)

$$\mathbb{U}_L^{\mathrm{e}} = \prod_{j=0}^{L} \Pi_{2L}^{-2j} U \Pi_{2L}^{2j}, \qquad \mathbb{U}_L^{\mathrm{o}} = \Pi_{2L}^{-1}\mathbb{U}^{\mathrm{e}}\Pi_{2L}. \tag{8.73}$$

We recall that Π_{2L} is a periodic shift for one site on the chain of $2L$ sites. The gate U deterministically changes only the middle site depending on the state of the sites on both edges. Therefore all the local operators applied at the same step commute, and the dynamics is indeed one of a local quantum circuit, albeit with a slightly nonstandard geometry (cf. Fig. 8.3). This allows us to use the ideas from Sec. 8.2 to formally express the slope s_α. Moreover, as demonstrated in Refs. [62, 64], the solvability of the model allows for an exact calculation of the fixed points (cf. Sec. 8.2), and hence of the entanglement slope, for a family of solvable initial states.

More concretely, for a quench from the state

$$|\Psi_0\rangle = \left(\begin{bmatrix} 1 \\ 0 \end{bmatrix} \otimes \begin{bmatrix} \sqrt{1-\vartheta} \\ \mathrm{e}^{i\varphi}\sqrt{\vartheta} \end{bmatrix} \right)^{\otimes L} \tag{8.74}$$

with $\varphi \in [0, 2\pi]$ and $\vartheta \in [0, 1]$, the asymptotic slope of the Rényi-α entropy reads as

$$s_\alpha = \frac{2}{1-\alpha} \ln \left[(1-\vartheta)^\alpha + \frac{\vartheta^\alpha}{y} \right], \tag{8.75}$$

where y is the only real and positive solution to the following equation

$$\ln y = 2 \ln \left[(1-\vartheta)^\alpha + \frac{\vartheta^\alpha}{y} \right]. \tag{8.76}$$

To compare the above exact expression with Eq. (8.57) we need to recall some facts about the TBA description of the model [302, 291], and a quench from the state (8.74) [64].

(i) The TBA description of states relevant for this quench problem involve only two species of particles, left and right movers, labelled by $n = \pm 1$.

(ii) The derivate of the dispersion relation $p_n'(\lambda)$, $\varepsilon_n'(\lambda)$, and the scattering kernel $T_{nm}(\lambda, \mu)$ are independent of the rapidities $\lambda, \mu \in [-\pi, \pi]$ and read as

$$\begin{gathered} p_n'(\lambda) = n, \qquad \varepsilon_n'(\lambda) = 1, \\ T_{nm}(\lambda, \mu) = \frac{nm}{2\pi}. \end{gathered} \tag{8.77}$$

(iii) The stationary state that the system approaches after the quench from (8.74) corresponds to filling functions equal to the parameter ϑ of the initial state

$$\vartheta_n(\lambda) = \vartheta. \tag{8.78}$$

Rewriting Eqs. (8.57) and (8.58) with these properties in mind, we find precisely Eqs. (8.75) and (8.76).

8.4.4 XXZ model

Finally, let us consider the anisotropic spin-1/2 Heisenberg chain given by the Hamiltonian

$$H = \frac{J}{4} \sum_{j=1}^{L} \Big[\sigma_j^x \sigma_{j+1}^x + \sigma_j^y \sigma_{j+1}^y + \Delta(\sigma_j^z \sigma_{j+1}^z - 1) \Big], \tag{8.79}$$

where $\sigma_j^{x,y,z}$ are Pauli matrices acting at site j and Δ is the anisotropy parameter, while the boundary conditions are assumed to be periodic. For the initial states of the quench protocol we consider the *Néel state* $|\Psi_{\rm N}\rangle$, and the *Majumdar-Ghosh state* $|\Psi_{\rm MG}\rangle$, defined as

$$|\Psi_{\rm N}\rangle = \frac{1}{\sqrt{2}} \Big(|\uparrow\downarrow\rangle^{\otimes L/2} + |\downarrow\uparrow\rangle^{\otimes L/2} \Big), \tag{8.80}$$

$$|\Psi_{\rm MG}\rangle = \frac{1}{\sqrt{2}} \Big(|\uparrow\downarrow\rangle - |\downarrow\uparrow\rangle \Big)^{\otimes L/2}. \tag{8.81}$$

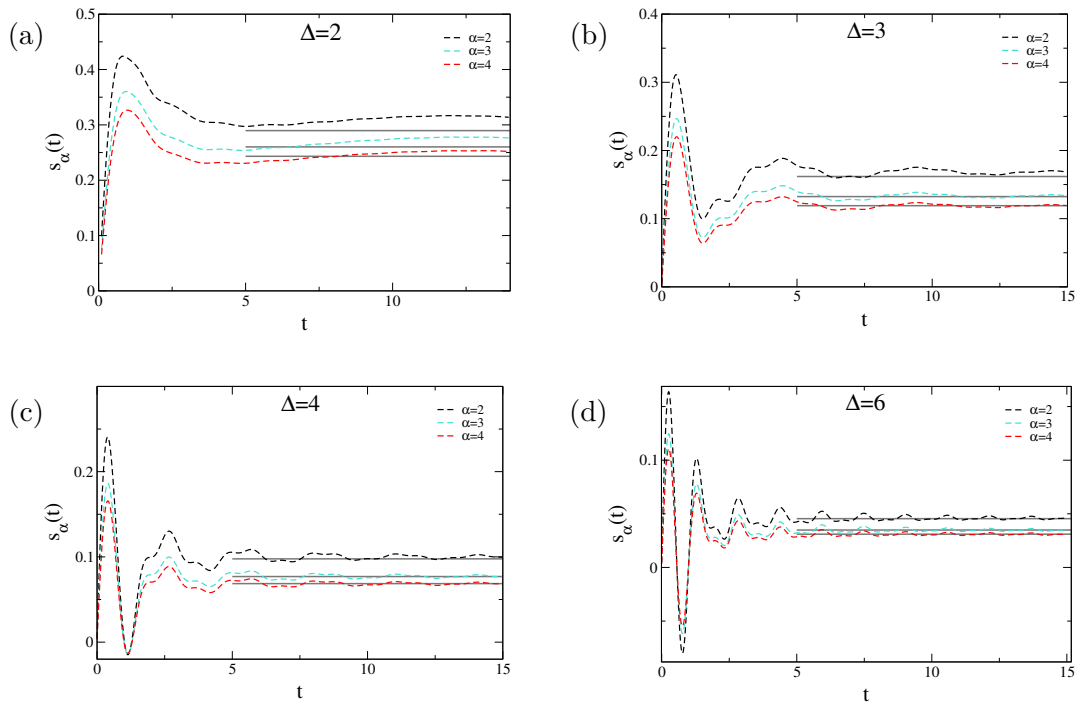

Figure 8.4: Numerical results for instantaneous Rényi slope $s_\alpha(t)$ after the quench from the Néel state (8.80). The dashed lines represent the numerical data, with different colors distinguishing between different values of α, while horizontal solid lines denote the analytical predictions for s_α. Each panel corresponds to a different value of the anisotropy parameter: (a) $\Delta = 2$, (b) $\Delta = 3$, (c) $\Delta = 4$, and (d) $\Delta = 6$.

Since these states are integrable [79], we expect our result to apply. Moreover, we can efficiently characterise the late-time stationary state using the quench-action approach [306, 307]. Therefore, we are able to explicitly evaluate the prediction given by Eqs. (8.64) and (8.58) (see Appendix 8.C for additional details), and compare it with numerical data obtained through the infinite time-evolving block decimation (iTEBD) [235] method. See Appendix 8.D for the details on the implementation.

In particular, we evaluate the Rényi entanglement entropies between the two halves of an infinite chain, and then express the *instantaneous Rényi slope* $s_\alpha(t)$, defined as the time-derivative of the Rényi entropy $S^{(\alpha)}_{\rm half}(t)$

$$s_\alpha(t) = \frac{\mathrm{d}S^{(\alpha)}_{\rm half}(t)}{\mathrm{d}t}. \tag{8.82}$$

Since the subsystem in question is half-infinite, we expect our prediction to coincide with the instantaneous slope in the $t \to \infty$ limit,

$$\lim_{t\to\infty} s_\alpha(t) = s_\alpha. \tag{8.83}$$

This limit, however, cannot be accessed numerically because the linear growth of entanglement after the quench implies exponential growth of computational complexity to simulate the dynamics. Therefore, we have to compare the prediction with finite-time data. We consider the regime $\Delta \geq 1$. In particular, since it is well known that for the initial states (8.80) and (8.81) the entanglement slope increases when approaching $\Delta = 1$ from above (see, e.g., Refs. [44, 45]), we restrict ourself to $\Delta > 1$.

The numerical results for the quench from the Néel state, and a range of different values of Δ, is shown in Fig. 8.4. We observe that the data exhibit complicated non-universal dynamics at short times, and then start approaching the asymptotic value. For all values of Δ and α, the agreement between the finite-time dynamics and the asymptotic prediction are extremely good, considering the fact that the accessible times are relatively short. Note that the seemingly larger deviations seen at $\Delta = 2$ are due to long-wavelength damped oscillations (observed generically in integrable systems, see, e.g., Refs. [43, 44]). Similarly, in Fig. 8.5 we test the prediction with the data for the quench from the Majumdar-Ghosh state. The numerics again matches the asymptotic slope very well.

8.5 Discussion

In this paper we investigated the growth of entanglement after quantum quenches in quantum many-body systems by characterising the evolution of the Rényi entropies of a compact subsystem. In the cases of interest here these quantities exhibit a linear growth in time followed by saturation to their "thermodynamic value", i.e., their value in the steady state. We showed that one can generically express the initial slope of a given Rényi entropy as the density of entropy in a particular state of the dual system, i.e., the system obtained swapping the roles of space and time, cf. Eq. (8.16). The latter state is

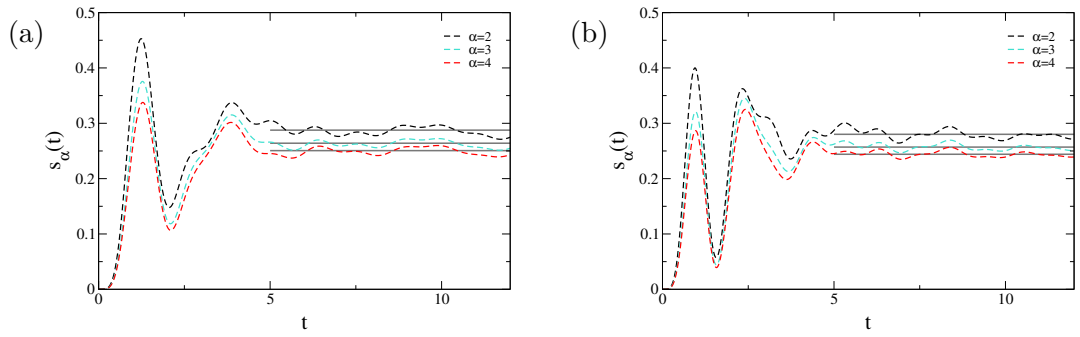

Figure 8.5: Dynamics of the instantaneous Rényi slope $s_\alpha(t)$ after the quench from the Majumdar-Ghosh state (8.81). The dashed lines represent the numerical data, and solid lines denote the analytical predictions for the asymptotic slope s_α. Different colours distinguish between different α, while the value of the anisotropy parameter is $\Delta = 3$ in the panel (a), and $\Delta = 4$ in (b).

directly expressed in terms of the fixed points of the space transfer matrix [269, 270, 271] — also known as influence matrices [272] —, which characterise the evolution of local observables in the thermodynamic limit.

In cases where the dual system can be interpreted as an isolated quantum many-body system — for example for *dual-unitary quantum circuits* [257] — the slope of a Rényi entropy is given by the *density of entropy in the stationary state of the dual system*. Crucially, because of crossing symmetry, this is the case also for relativistic quantum field theories, provided that the direct swap of space and time is replaced by an appropriate analytic continuation.

We used this observation to find a closed-form expression for the slope of Rényi entropies in integrable relativistic quantum field theories, going beyond what is currently achievable by known approaches such as form factor expansions [308, 155, 316, 317]. Moreover, we argued that this expression can be directly extended to all TBA integrable models. The most general form of our formula is reported in Eq. (8.57). To support the validity of Eq. (8.57) we showed that it reproduces the only known results for the slopes of Rényi entropies in an interacting integrable system [64], the quasiparticle picture prediction in the von Neumann limit [44], and it reduces to the correct non-interacting limit [43, 35]. We also provided stringent numerical checks for several quenches in the XXZ spin-1/2 chain.

Our results have two significant merits. First, with Eq. (8.16) we provided a direct relation between growth of entanglement in a given isolated quantum many-body system and the spatial scaling of stationary entanglement in its dual. This complements an analogous relation discovered in Ref. [256], for systems with edge decoherence. Second, with Eq. (8.57) we solved the long standing open problem of computing the growth of Rényi entropies in interacting integrable models. In the following two subsections we discuss two further aspects of the latter result. Specifically, in Sec. 8.5.1 we show that it cannot be interpreted in terms of a physically meaningful quasiparticle picture,

while in Sec. 8.5.2 we discuss its extension to describe the full time-evolution of the entanglement of a *finite* subsystem, i.e., beyond the initial growth regime. Finally in Sec. 8.5.3 we discuss some future directions stemming from our work.

8.5.1 Eq. (8.57) and the Quasiparticle Picture

Here we generalise an argument presented in Ref. [64] for the case of Rule 54, to argue that the expressions (8.63) and (8.64) *cannot* be interpreted in terms of a physically meaningful quasiparticle picture. To explain our reasoning, let us begin by briefly recalling the essential ingredients of the latter.

The quasiparticle picture is based on two basic postulates [41]: (i) the initial state $|\Psi_0\rangle$ produces pairs of *correlated* (or *entangled*) quasiparticles — objects propagating as free classical particles — at every point in space; (ii) at any time $t \geq 0$, the entanglement between a given subsystem A and its complement $\bar{A}$ is proportional to the number of correlated pairs shared between the two.

Admitting that, in general, quasiparticles can come in multiple species — labelled by a positive integer n — and have a nontrivial dispersion relation — parametrised by a rapidity μ — the two postulates above lead to the following evolution equation for a given Rényi entropy

$$S^{(\alpha)}_{A,\mathrm{qp}}(t) = \int_{+} \mathrm{d}\boldsymbol{\mu}\, \min(2v_{\mathrm{qp}}(\boldsymbol{\mu})t, |A|)s_\alpha(\boldsymbol{\mu})\,. \tag{8.84}$$

Here we adopted the shorthand notation of Eqs. (8.55) and (8.58), and used that, for solvable initial states, the correlated pairs are formed by quasiparticles of the same species and opposite rapidity [44]. Moreover, we denoted by

$$v_{\mathrm{qp}}(\boldsymbol{\mu}) = v_{n,\mathrm{qp}}(\mu), \tag{8.85}$$

the velocity of the quasiparticles of species n and rapidity μ, and by

$$s_\alpha(\boldsymbol{\mu}) = s_{n,\alpha}(\mu), \tag{8.86}$$

the contribution to the Rényi entropy of a pair of quasiparticles of species n and rapidities $\pm\mu$.

To make Eq. (8.84) truly predictive one needs to specify $v_{\mathrm{qp}}(\boldsymbol{\mu})$ and $s_\alpha(\boldsymbol{\mu})$. In particular, Ref. [44] showed that one can describe the dynamics of von-Neumann entropy by making the two following assumptions: (i) $s_1(\boldsymbol{\mu})$ is the density of entanglement entropy (cf. (8.69)); (ii) $v_{\mathrm{qp}}(\boldsymbol{\mu})$ is given by velocity of excitations on the thermodynamic macrostate describing the stationary value of local observables after the quench. The latter is fixed by Eqs. (8.61) and (8.62), where $\vartheta(\boldsymbol{\mu})$ is the filling function of the relevant stationary state.

Here we do not use these assumptions and, for the moment, we compare (8.84) to (8.63) and (8.64) leaving $v_{\mathrm{qp}}(\boldsymbol{\mu})$ and $s_\alpha(\boldsymbol{\mu})$ unspecified. In particular, we consider an initial state producing a filling function of the form

$$\vartheta_n(\mu) = \delta_{n,\bar{n}} \begin{cases} \vartheta & \mu \in [\bar{\mu} - \delta, \bar{\mu} + \delta], \\ 0 & \text{otherwise}, \end{cases} \tag{8.87}$$

with $\vartheta \leq 1$ and $\delta \ll 1$. In this case, we see that the three equations are compatible for all $\bar{n}$ and $\bar{\mu}$ only if

$$v_{\rm qp}(\boldsymbol{\mu}) = \frac{\varepsilon'(\boldsymbol{\mu})}{|p'(\boldsymbol{\mu})|} \frac{\ln\left[(1-\vartheta(\boldsymbol{\mu}))^\alpha + \dfrac{\vartheta(\boldsymbol{\mu})^\alpha}{y_\alpha(\boldsymbol{\mu})}\right]}{\ln\left[(1-\vartheta(\boldsymbol{\mu}))^\alpha + \dfrac{\vartheta(\boldsymbol{\mu})^\alpha}{x_\alpha(\boldsymbol{\mu})}\right]}. \tag{8.88}$$

The crucial observation at this point is that the right hand side of (8.88) depends non-trivially on α. Therefore, one needs to allow for an α-dependent quasiparticle velocity $v_{\rm qp}(\boldsymbol{\mu})$. At first sight this might seem enough to exclude the applicability of any quasiparticle picture. Indeed it is natural to require that the properties of quasiparticles have to be fixed by initial state and dynamics and cannot depend on the specific observable (e.g. on α). Here, however, we allow for more flexibility: since Rényi entropies have a non-linear dependence on the state of the system, their stationary values are described by an α-dependent macrostate with filling function [212]

$$\vartheta_\alpha(\boldsymbol{\mu}) = \frac{\vartheta(\boldsymbol{\mu})^\alpha}{x_\alpha(\boldsymbol{\mu})(1-\vartheta(\boldsymbol{\mu}))^\alpha + \vartheta(\boldsymbol{\mu})^\alpha}, \tag{8.89}$$

where $\vartheta(\boldsymbol{\mu})$ is the filling function (8.87). One can then wonder whether the velocity of excitations on the α-dependent macrostate — obtained by solving Eqs. (8.61) and (8.62) with $\vartheta(\boldsymbol{\mu})$ — coincides with (8.88). However, this is the case only in the limit $\alpha \to 1$.

Since the velocity on the r.h.s. of (8.88) cannot be interpreted as the velocity of the excitations on a physically meaningful macrostate, we conclude that the quasiparticle picture does not describe the dynamics of Rényi entropies, at least at the quantitative level.

8.5.2 Finite Subsystems

One of the benefits of the quasiparticle picture is that, just using the few assumptions recalled in the previous subsection, one can quantitatively determine the evolution of entanglement in a wealth of different settings. Essentially, the dynamics of entanglement becomes a problem of one-dimensional kinematics: knowledge of velocities and entanglement contributions of each species of quasiparticles is enough to immediately determine the whole dynamics of the entanglement of a finite subsystem (cf. (8.84)). The breakdown of the quasiparticle picture for $\alpha \neq 1$ completely changes the game. Determining the full curve $S_A^{(\alpha)}(t)$ becomes a highly non-trivial task for interacting integrable systems and our results for slope and density do not seem sufficient to achieve it. Here we present some evidence suggesting that, in fact, they might be enough.

To this end we make two minimal assumptions: (i) Each "mode" with quantum number $\boldsymbol{\mu}$ evolves independently; (ii) For each mode the entanglement grows with fixed slope $2s_\alpha(\boldsymbol{\mu})$ until it abruptly saturates to $d_\alpha(\boldsymbol{\mu})|A|$ (the factor of 2 comes from the fact that the subsystem has two edges). A way to justify the assumption of abrupt

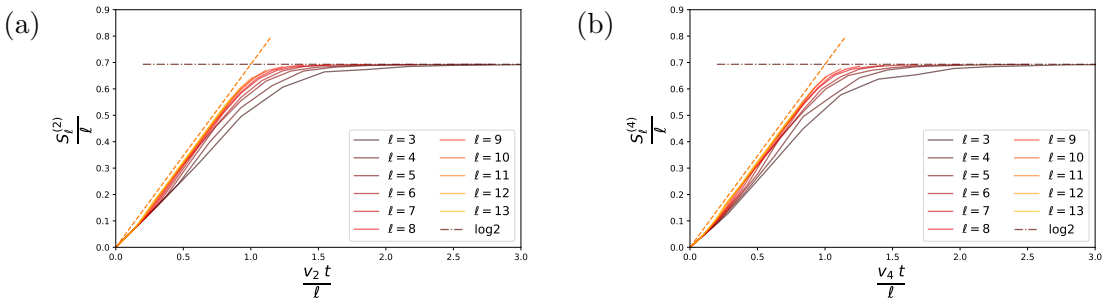

Figure 8.6: Tensor network simulations of the entanglement dynamics for Rule 54. We consider an open system of $L = 50$ sites and we focus on the subsystem A made of the first ℓ sites, with $\ell = 3, \dots 10$. We fix the bond dimension equal to 4096. The dashed line is the exact prediction for $s_\alpha t$ (note the absence of the factor of 2 w.r.t. Eq. (8.90) due to the choice of different boundary conditions), while the dotted-dashed one the asymptotic thermodynamic entropy $d_\alpha \ell$. Our conjecture (8.90) corresponds to the joining of the two straight lines. The *entanglement velocity* that rescales the time is $v_\alpha = s_\alpha/d_\alpha$.

saturation is to argue that modes behave as a chaotic systems following the membrane picture [73, 74].

The two assumptions above lead to the following evolution equation for a given Rényi entropy

$$S^{(\alpha)}_{A,\mathrm{conj}}(t) = \int_+ \mathrm{d}\boldsymbol{\mu}\, \min(2s_\alpha(\boldsymbol{\mu})t, d_\alpha(\boldsymbol{\mu})|A|)\,, \tag{8.90}$$

which we conjecture apply at the leading order for large t and $|A|$.

Testing (8.90) numerically in a standard interacting integrable model, such as the XXZ spin chain, is very hard (see the simulations for $\alpha = 1$ in Ref. [44]): one cannot typically access its regime of validity in a sufficiently controlled manner to wash off all sub-leading corrections. However, it is instructive to test it for Rule 54. Indeed, since in that model there is a single mode for all α's, we can directly verify Assumption (ii), without worrying about the subtle effects of the integration over $\boldsymbol{\mu}$. Our numerical results based on tensor network simulations are reported in Fig. 8.6. We can clearly see that as ℓ increases the data approach our conjecture quite neatly, although we cannot exclude a different crossover close to the saturation point.

8.5.3 Future Perspectives

The results presented in this paper generate many significant questions for future research. Here we discuss a number of them.

A direct question concerns the possibility of devising generalisations of our approach to treat other relevant quantities or describe more general settings. For instance, a recent point of interest in the research on quantum many-body dynamics is to understand how the entanglement is split among different symmetry sectors, with symmetry resolved

entropies directly measured in experiments [40]. While the quasiparticle picture has been shown to hold for free systems [50, 51], no result is available in the interacting case. An immediate question is then whether one can use the the recently obtained explicit results for equilibrium states [318] to generalise our approach and access the the full dynamics of symmetry resolved Rényi entropies. At the same time, it is also interesting to wonder whether our approach can be extended to inhomogeneous settings. Indeed, in this case the late-time quasi-stationary regime is still characterised using integrability via the framework of generalised hydrodynamics (GHD) [279, 283], and an appropriate modification of the quasiparticle picture correctly characterises the time evolution of the von-Neumann entanglement entropy [83, 54].

A second set of questions, instead, stems from our findings on the inapplicability of the quasiparticle picture to describe Rényi entropies in interacting integrable models. Indeed, as touched upon in the introduction, the fact that the entanglement is propagated by quasiparticles — rather than behaving as a membrane in the spacetime — has direct consequences on its phenomenology. These are revealed, for instance, in the qualitative behaviour of the bipartite entanglement between a disjoint region and the rest of the system [66, 73, 83, 46], or in a system of finite size [73, 83, 48]. Recent studies, however, suggest that this might be the case also concerning multipartite entanglement, which is conveniently characterised by the *entanglement negativity* and the higher moments of the partial transpose of the reduced density matrix [319, 320, 321, 322, 323]. Using on the quasiparticle picture, Ref. [46] argued that, after a quantum quench, the logarithmic negativity coincides with half of the Rényi mutual information with $\alpha = 1/2$ — a similar statement holds for the higher moments [49]. On the other hand, Ref. [268] has recently shown that in general this relation holds only in the early time regime. Therefore, it is interesting to wonder what happens for interacting integrable systems beyond this regime.

Finally, we mention that our formula (8.57) for the slope of Rényi entropies in all TBA-integrable models has not been rigorously proven here, even though the arguments we provided leave little doubts on its validity. Nevertheless, the correspondence that we established between slope in the original model and steady state entropy in the dual model provides an ideal starting point for such a rigorous proof. A direct question for future research is then to devise such a rigorous proof — for instance using the framework of algebraic Bethe ansatz. Besides the major interest that such a proof would have *per se*, it would also lead to a rigorous validation of the quasiparticle conjecture in the replica limit $\alpha \to 1$ — a problem that has been open since 2005 [41].

8.A Fixed points as stationary density matrices

The fact that the matrices $M_{\mathrm{L/R},t}$ exhibit the Cholesky decomposition (8.18) follows directly from the explicit form of the fixed points. In particular, the fixed points of the

circuit shown in Fig. 8.1 take the following form (see, e.g., [270, 63])

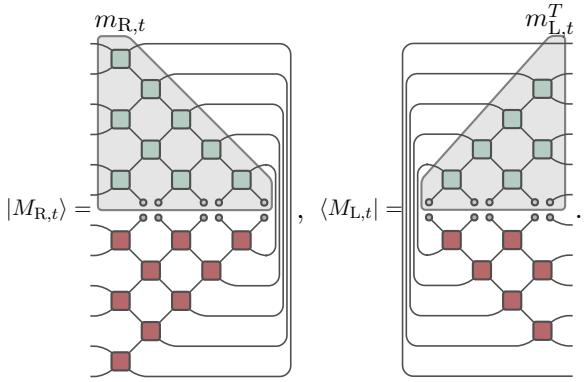

(8.91)

Here we introduced the operators $m_{\mathrm{R},t}$ and $m^T_{\mathrm{L},t}$ (in grey), which map from left to right. Recalling now that the corresponding matrices $M_{\mathrm{R/L},t}$ act on the $2t$ horizontal legs at the top, and map them to the $2t$ legs at the bottom, we can immediately express them in terms of $m_{\mathrm{R},t}$, $m^T_{\mathrm{L},t}$ as

$$M_{\mathrm{R},t} = m_{\mathrm{R},t} m^\dagger_{\mathrm{R},t}, \qquad M_{\mathrm{L},t} = m_{\mathrm{L},t} m^\dagger_{\mathrm{L},t}. \tag{8.92}$$

Note that we only considered the case with the initial state in the product form. With minor modifications, however, the argument can be repeated also for the initial state in the form of a MPS, as long as the MPS transfer matrix has a unique dominant eigenvector.

8.B Partially decoupled form of (8.58) and (8.60)

In systems with multiple types of particle species, Eqs. (8.58) and (8.60) involve both an integral over rapidities, and an infinite sum over the particle species. However, using standard TBA manipulations [262] the equations can be put in an equivalent form, referred to as the *decoupled form*, so that each particle species n is only coupled to $n+1$, and $n-1$, which makes the set of equations simpler to solve.

For simplicity we restrict the discussion to the systems with the *even* kernel that is in the difference form,

$$T_{nm}(\lambda,\mu) = T_{nm}(\lambda-\mu) = T_{nm}(\mu-\lambda), \tag{8.93}$$

but a similar manipulation could be done more generally. In this case, the integral equations (8.60) and (8.58) can be succinctly expressed as

$$\begin{aligned} \ln x_n(\lambda) &= \sum_m \Big(T_{nm} * \ln\big[(1-\vartheta_m)^\alpha + \frac{\vartheta_m^\alpha}{x_m}\big] \Big)(\lambda), \\ \ln y_n(\lambda) &= \sum_m \Big(T_{nm} * \mathrm{sgn}(\cdot) \ln\big[(1-\vartheta_m)^\alpha + \frac{\vartheta_m^\alpha}{y_m^{\mathrm{sgn}(\cdot)}}\big] \Big)(\lambda), \end{aligned} \tag{8.94}$$

where we introduced the shorthand notation $*$ for the convolution,

$$(f*g)(\lambda)=\int \mathrm{d}\mu f(\lambda-\mu)g(\mu), \tag{8.95}$$

and $\mathrm{sgn}(\cdot)$ is the sign function,

$$\mathrm{sgn}(x)=\begin{cases}1, & x>0,\\ 0, & x=0,\\ -1, & x<0.\end{cases} \tag{8.96}$$

Note that we dropped the explicit dependence on α from $x_{\alpha,n}$ and $y_{\alpha,n}$ to ease the notation.

A necessary ingredient for the decoupled form is the existence of the function $s(\lambda)$ that satisfies the following set of equations,

$$\begin{aligned}T_{1m}(\lambda)&=s*T_{2,m}(\lambda)+\delta_{2,m}s(\lambda)\\ T_{nm}(\lambda)&=s*(T_{n-1,m}+T_{n+1,m})(\lambda)\\ &\quad+(\delta_{n-1,m}+\delta_{n+1,m})s(\lambda), \qquad n\geq 2\,.\end{aligned} \tag{8.97}$$

Combining this with (8.94), we finally obtain the following equivalent form of (8.60), and (8.58),

$$\begin{aligned}\ln x_1(\lambda)&=s*\ln\left[(1-\vartheta_2)^\alpha x_2+\vartheta_2^\alpha\right](\lambda),\\ \ln x_n(\lambda)&=s*\ln\left[(1-\vartheta_{n-1})^\alpha x_{n-1}+\vartheta_{n-1}^\alpha\right](\lambda)\\ &\quad+s*\ln\left[(1-\vartheta_{n+1})^\alpha x_{n+1}+\vartheta_{n+1}^\alpha\right](\lambda),\\ \ln y_1(\lambda)&=s*\mathrm{sgn}(\cdot)\ln\left[(1-\vartheta_2)^\alpha y_2^{\mathrm{sgn}(\cdot)}+\vartheta_2^\alpha\right](\lambda),\\ \ln y_n(\lambda)&=s*\mathrm{sgn}(\cdot)\ln\left[(1-\vartheta_{n-1})^\alpha y_{n-1}^{\mathrm{sgn}(\cdot)}+\vartheta_{n-1}^\alpha\right](\lambda)\\ &\quad+s*\mathrm{sgn}(\cdot)\ln\left[(1-\vartheta_{n+1})^\alpha y_{n+1}^{\mathrm{sgn}(\cdot)}+\vartheta_{n+1}^\alpha\right](\lambda).\end{aligned} \tag{8.98}$$

8.C TBA equations for XXZ

Here we summarise the relevant details of the TBA description of the XXZ model in the $\Delta>1$ regime [262]. It is convenient to parametrise Δ as

$$\Delta=\cosh(\eta), \qquad \eta>0, \tag{8.99}$$

and express physically relevant quantities (such as energy and momentum) in terms of η rather than Δ.

The elementary excitations (magnons) can form infinitely many different bound states, while their rapidity is constrained to $|\lambda|\leq\pi/2$, therefore the integral over $\boldsymbol{\lambda}=(\lambda,n)$ should be understood as

$$\int d\boldsymbol{\lambda}=\sum_{n=1}^{\infty}\int_{-\frac{\pi}{2}}^{\frac{\pi}{2}}d\lambda, \tag{8.100}$$

and in particular integrals over *positive* rapidities are meant as

$$\int_{+} d\boldsymbol{\lambda} = \sum_{n=1}^{\infty} \int_{0}^{\frac{\pi}{2}} d\lambda. \tag{8.101}$$

Derivatives of bare energy $\varepsilon_n'(\lambda)$ and momentum $p_n'(\lambda)$ read as

$$\begin{aligned} \frac{1}{2\pi}\varepsilon_n'(\lambda) &= \frac{1}{\pi}\frac{\sin(2\lambda)\sinh(\eta)\sinh(n\eta)}{\big(\cosh(n\eta)-\cos(2\lambda)\big)^2}, \\ \frac{1}{2\pi}p_n'(\lambda) &= \frac{1}{\pi}\frac{\sinh(n\eta)}{\cosh(n\eta)-\cos(2\lambda)}, \end{aligned} \tag{8.102}$$

while the kernel takes a difference form, $T(\boldsymbol{\lambda},\boldsymbol{\mu}) = T_{nm}(\lambda-\mu)$, and is given by

$$\begin{aligned} T_{nn}(\lambda) &= \frac{1}{2\pi}\sum_{k=1}^{n} p_{2k}'(\lambda), \\ T_{nm}(\lambda) &= \frac{1}{2\pi}\sum_{k=0}^{\frac{n+m-|n-m|}{2}} p_{|n-m|+2k}'(\lambda), \quad m\neq n. \end{aligned} \tag{8.103}$$

The last ingredient needed for the evaluation of the predictions is the filling function $\vartheta_n(\lambda)$. This is obtained as [314, 307]

$$\vartheta_n(\lambda) = \frac{1}{1+\eta_n(\lambda)}, \tag{8.104}$$

where $\eta_n(\lambda)$ is the solution to the following integral equation

$$\begin{aligned} \ln\eta_n(\lambda) &= g_n(\lambda) \\ &\quad + \sum_{m=1}^{\infty}\int_{-\frac{\pi}{2}}^{\frac{\pi}{2}} \mathrm{d}\mu\, T_{nm}(\mu-\lambda)\ln(1+\frac{1}{\eta_m(\mu)}). \end{aligned} \tag{8.105}$$

Here, $g_n(\lambda)$ encodes the information about the initial state. For all integrable initial states the values of $g_n(\lambda)$ for $n>1$ are expressed in terms of $g_1(\lambda)$ as

$$g_n(\lambda) = \sum_{k=1}^{n} g_1\!\left(\lambda + i\eta\frac{n+1-2k}{2}\right), \tag{8.106}$$

while $g_1(\lambda)$ for the two cases considered here reads as

$$\begin{aligned} g_1^{(\mathrm{MG})}(\lambda) &= -\ln\left(\frac{\sinh^4(\lambda)\cot^2(\lambda)}{\sin(2\lambda+i\eta)\sin(2\lambda-i\eta)}\right), \\ g_1^{(\mathrm{N\acute{e}el})}(\lambda) &= \frac{\tan\left(\lambda+\frac{i\eta}{2}\right)\tan\left(\lambda-\frac{i\eta}{2}\right)}{4\sin^2(2\lambda)}. \end{aligned} \tag{8.107}$$

8.D Details on the iTEBD simulations

To perform the simulations we first build the Matrix Product State (MPS) representation for the initial state. Both the Néel state and the Majumdar-Ghosh state (cf. (8.80) and (8.81)) admit a MPS representation with small bond dimension. Then we perform the dynamics by applying a second order Trotter decomposition of the time-evolution operator. We verified that a Trotter step $\delta t = 0.05$ is sufficient to ensure time-converged results. Due to the linear growth of entanglement the bond dimension of the MPS representing the time-evolved state increases exponentially with time. For this reason, at each step of the evolution we perform a truncation of the MPS using singular value decomposition keeping the largest $\chi_{\max}$ singular values. To monitor the loss of precision, we perform iTEBD simulations with increasing bond dimension $\chi_{\max}$ up to $\chi_{\max} = 8192$ for $\Delta = 2$, and $\chi_{\max} = 4096$ for other values of Δ. We then compare the data with two consecutive values of $\chi_{\max}$ and only keep the data for which the two simulations agree. This allows us to reach times of the order $t \lesssim 15$.

Bibliography

[1] G. Lagnese, F. M. Surace, M. Kormos and P. Calabrese, *Confinement in the spectrum of a Heisenberg-Ising spin ladder*, J. Stat. Mech. (2020) 093106.

[2] G. Lagnese, F. M. Surace, M. Kormos, and P. Calabrese, *False vacuum decay in quantum spin chains*, Phys. Rev. B **104**, L201106 (2021).

[3] G. Lagnese, F. M. Surace, M. Kormos, and P. Calabrese, *False vacuum decay in quantum spin chains*, J. Phys. A: Math. Theor. **55** 124003 (2022).

[4] G. Lagnese, P. Calabrese and L. Piroli, *Entanglement dynamics of thermofield double states in integrable models*, J. Phys. A: Math. Theor *in progress* (2022) .

[5] B. Bertini, K. Klobas, V. Alba, G. Lagnese, P. Calabrese, *Growth of Rényi Entropies in Interacting Integrable Models and the Breakdown of the Quasiparticle Picture*, arXiv:2203.17264.

[6] Immanuel Bloch, Jean Dalibard, and Wilhelm Zwerger,*Many-body physics with ultracold gases* , Rev. Mod. Phys. **80**, 885 (2008)

[7] Polkovnikov, A., K. Sengupta, A. Silva, and M. Vengalattore,*Colloquium: Nonequilibrium dynamics of closed interacting quantum systems*, Rev. Mod. Phys. 83, 863 (2011).

[8] J. Eisert, M. Friesdorf C. Gogolin , *Quantum many-body systems out of equilibrium*, Nature Phys **11**, 124–130 (2015)

[9] Marcos Rigol, Vanja Dunjko and Maxim Olshanii,*Thermalization and its mechanism for generic isolated quantum systems*, Nature vol. **452**, 854–858 (2008)

[10] P. Calabrese, F. H. L. Essler, and G. Mussardo, *Introduction to 'Quantum Integrability in Out of Equilibrium Systems,'* J. Stat. Mech. (2016) 064001.

[11] Luca D'Alessio and Yariv Kafri and Anatoli Polkovnikov and Marcos Rigol, *From quantum chaos and eigenstate thermalization to statistical mechanics and thermodynamics*, Advances in Physics Vol. 65 **3** 239-362 (2016)

[12] J. Dziarmaga, *Dynamics of a quantum phase transition and relaxation to a steady state*, Adv. Phys. **59** 1063 (2010).

[13] C. De Grandi ,V. Gritsev and A. Polkovnikov, *Quench dynamics near a quantum critical point: application to the sine-Gordon model*, Phys. Rev. B **81** 224301 (2010)

[14] A. Dutta, G. Aeppli, B. K. Chakrabarti, U.Divakaran, T. F. Rosenbaum and D. Sen D, Quantum Phase Transitions in Transverse Field Spin Models: from Statistical Physics to Quantum Information (Cambridge: Cambridge University Press)

[15] S. B. Rutkevich, *Partial thermalization in the quantum chain of harmonic oscillators*, arXiv:1201.0578.

[16] P. Calabrese and J. Cardy, *Time Dependence of Correlation Functions Following a Quantum Quench*, Phys. Rev. Lett. **96**, 136801 (2006).

[17] P. Calabrese and J. Cardy, *Quantum quenches in extended systems*, J. Stat. Mech. P06008 (2007).

[18] D.A. Abanin, E. Altman, I. Bloch and M. Serbyn, *Colloquium: Many-body localization, thermalization, and entanglement*, Rev. Mod. Phys. 91 (2019) 021001.

[19] M. Serbyn, D.A. Abanin and , Z. Papić, *Quantum many-body scars and weak breaking of ergodicity*, Nat. Phys. **17**, 675–685 (2021).

[20] S. Scopa, P. Calabrese, and A. Bastianello, *Entanglement dynamics in confining spin chains*,Phys. Rev. B 105, 125413 (2022)

[21] S. Birnkammer, A. Bastianello, Mi. Knap, *Prethermalization in confined spin chains*, arXiv.2202.12908.

[22] M. Kormos, M. Collura, G. Takács, and P. Calabrese, *Real-time confinement following a quantum quench to a non-integrable model*, Nature Phys. **13**, 246 (2017).

[23] F. H. L. Essler and M. Fagotti, *Quench Dynamics and Relaxation in Isolated Integrable Quantum Spin Chains*, J. Stat. Mech. (2016) 064002.

[24] J. M. Deutsch, Haibin Li, and Auditya Sharma, *Microscopic origin of thermodynamic entropy in isolated systems*, Phys. Rev. E **87**, 042135 (2013).

[25] G. Vidal, *Entanglement monotones*, J. Mod. Opt. **47** (2000) 355.

[26] M. B. Plenio and S. Virmani, *An Introduction to Entanglement Measures*, Quantum Info. Comput. **7** (2007) 1.

[27] R. Horodecki, P. Horodecki, M. Horodecki and K. Horodecki, *Quantum entanglement*, Rev. Mod. Phys. **81** (2009) 865.

[28] LESNE, A., *Shannon entropy: A rigorous notion at the crossroads between probability, information theory, dynamical systems and statistical physics*, Mathematical Structures in Computer Science, 24(3), E240311 (2014).

[29] N. Laflorencie, *Quantum entanglement in condensed matter systems*, Phys. Rep. 646, **1** (2016)

[30] H. Li and F. D. M. Haldane, *Entanglement spectrum as a generalization of entanglement entropy: Identification of topological order in non-abelian fractional quantum Hall effect states*, Phys. Rev. Lett. **101**, 010504 (2008).

[31] R. Islam, R. Ma, P. M. Preiss, M. E. Tai, A. Lukin, M. Rispoli, and M. Greiner, *Measuring entanglement entropy in a quantum many-body system*, Nature **528**, 77 (2015).

[32] A. M. Kaufman, M. E. Tai, A. Lukin, M. Rispoli, R. Schittko, P. M. Preiss and M. Greiner, *Quantum thermalization through entanglement in an isolated many-body system*, Science **353**, 794 (2016).

[33] N. M. Linke, S. Johri, C. Figgatt, K. A. Landsman, A. Y. Matsuura, and C. Monroe, *Measuring the R´enyi entropy of a two-site Fermi-Hubbard model on a trapped ion quantum computer*, Phys. Rev. A **98**, 052334 (2018)

[34] A. Lukin, M. Rispoli, R. Schittko, M. E. Tai, A. M. Kaufman, S. Choi, V. Khemani, J. Leonard, and M. Greiner, *Probing entanglement in a many-body-localized system*, Science **364**, 256 (2019).

[35] M. Fagotti, *Dinamica di non-equilibrio dell'entanglement e delle correlazioni in una catena di spin, Master's thesis*, University of Pisa (2008), https://etd.adm.unipi.it/t/etd-09022008-110340.

[36] A. Elben, R. Kueng, H. Y. R. Huang, R. van Bijnen, C. Kokail, M. Dalmonte, P. Calabrese, B. Kraus, J. Preskill, P. Zoller, and B. Vermersch,*Mixed-state entanglement from local randomized measurements*, Phys. Rev. Lett. **125**, 200501 (2020).

[37] Y. Zhou, P. Zeng, and Z. Liu, *Single-copies estimation of entanglement negativity*, Phys. Rev. Lett. **125**, 200502 (2020).

[38] A. Neven, J. Carrasco, V. Vitale, C. Kokail, A. Elben, M. Dalmonte, P. Calabrese, P. Zoller, B. Vermersch, R. Kueng, and B. Kraus, *Symmetry-resolved entanglement detection using partial transpose moments*, npj Quantum Inf. **7**, 1 (2021).

[39] T. Brydges, A. Elben, P. Jurcevic, B. Vermersch, C. Maier, B. P. Lanyon, P. Zoller, R. Blatt, and C. F. Roos, *Probing entanglement entropy via randomized measurements*, Science **364**, 260 (2019).

[40] V. Vitale, A. Elben, R. Kueng, A. Neven, J. Carrasco, B. Kraus, P. Zoller, P. Calabrese, B. Vermersch, and M. Dalmonte, *Symmetry-resolved dynamical purification in synthetic quantum matter*, arXiv:2101.07814.

[41] P. Calabrese and J. Cardy, *Evolution of Entanglement Entropy in One-Dimensional Systems*, J. Stat. Mech. (2005) P04010.

[42] P. Calabrese, *Entanglement spreading in non-equilibrium integrable systems*, SciPost Phys. Lect. Notes 20 (2020).

[43] M. Fagotti and P. Calabrese, *Evolution of Entanglement Entropy Following a Quantum Quench: Analytic Results for the XY Chain in a Transverse Magnetic Field*, Phys. Rev. A **78**, 010306 (2008).

[44] V. Alba and P. Calabrese, *Entanglement and thermodynamics after a quantum quench in integrable systems*, PNAS **114**, 2021 (2017).

[45] V. Alba and P. Calabrese, *Entanglement Dynamics after Quantum Quenches in Generic Integrable Systems*, SciPost Phys. **4**, 017 (2018).

[46] V. Alba and P. Calabrese, *Quantum information dynamics in multipartite integrable systems*, EPL **126**, 60001 (2019).

[47] V. Alba and P. Calabrese, *Quantum Information Scrambling after a Quantum Quench*, Phys. Rev. B **100**, 115150 (2019).

[48] R. Modak, V. Alba, and P. Calabrese, *Entanglement Revivals as a Probe of Scrambling in Finite Quantum Systems*, J. Stat. Mech. (2020) 083110.

[49] S. Murciano, V. Alba, and P. Calabrese, *Quench Dynamics of Renyi Negativities and the Quasiparticle Picture*, arXiv:2110.14589 (2021).

[50] G. Parez, R. Bonsignori, and P. Calabrese, *Quasiparticle dynamics of symmetry-resolved entanglement after a quench: Examples of conformal field theories and free fermions*, Phys. Rev. B **103**, L041104 (2021).

[51] G. Parez, R. Bonsignori, and P. Calabrese, *Exact quench dynamics of symmetry resolved entanglement in a free fermion chain*, J. Stat. Mech.: Theory Exp. **2021** (9), 093102.

[52] B. Bertini and P. Calabrese, *Prethermalisation and Thermalisation in the Entanglement Dynamics*, Phys. Rev. B **102**, 094303 (2020)

[53] B. Bertini, M. Fagotti, L. Piroli, and P. Calabrese, *Entanglement Evolution and Generalised Hydrodynamics: Noninteracting Systems*, J. Phys. A: Math. Theor. **51**, 39LT01 (2018).

[54] V. Alba, B. Bertini, and M. Fagotti, *Entanglement Evolution and Generalised Hydrodynamics: Interacting Integrable Systems*, SciPost Phys. **7**, 005 (2019).

[55] V. Alba, B. Bertini, M. Fagotti, L. Piroli, and P. Ruggiero, *Generalized-Hydrodynamic Approach to Inhomogeneous Quenches: Correlations, Entanglement and Quantum Effects*, J. Stat. Mech. 2021, 114004 (2021).

[56] M. Mestyán and V. Alba, *Molecular dynamics simulation of entanglement spreading in generalized hydrodynamics*, SciPost Phys. **8**, 055 (2020).

[57] V. Alba, *Unbounded entanglement production via a dissipative impurity*, arXiv:2104.10921.

[58] V. Alba and F. Carollo, *Spreading of correlations in Markovian open quantum systems*, Phys. Rev. B **103**, 020302 (2021).

[59] F. Carollo and V. Alba, *Emergent dissipative quasiparticle picture in noninteracting Markovian open quantum systems*, arXiv:2106.11997.

[60] V. Alba and F. Carollo, *Hydrodynamics of quantum entropies in Ising chains with linear dissipation*, arXiv:2109.01836.

[61] R. Modak, L. Piroli, and P. Calabrese, *Correlation and Entanglement Spreading in Nested Spin Chains*, J. Stat. Mech. (2019) 093106.

[62] K. Klobas, B. Bertini, and L. Piroli, *Exact thermalization dynamics in the "Rule 54" quantum cellular automaton*, Phys. Rev. Lett. **126**, 160602 (2021).

[63] K. Klobas and B. Bertini, *Exact relaxation to Gibbs and non-equilibrium steady states in the quantum cellular automaton Rule 54*, SciPost Phys. **11**, 106 (2021).

[64] K. Klobas and B. Bertini, *Entanglement dynamics in Rule 54: Exact results and quasiparticle picture*, SciPost Phys. 11, **107** (2021).

[65] H. Liu and S. J. Suh, *Entanglement tsunami: Universal scaling in holographic thermalization*, Phys. Rev. Lett. **112**, 011601 (2014)

[66] C. T. Asplund, A. Bernamonti, F. Galli, and T. Hartman,*Entanglement scrambling in 2d conformal field theory*, J. High Energy Phys. **2015** (9), 110 (2015)

[67] A. M. L¨auchli and C. Kollath, *Spreading of correlations and entanglement after a quench in the one-dimensional bose–hubbard model*, J. Stat. Mech. **(2008) P05018**.

[68] H. Kim and D. A. Huse, *Ballistic spreading of entanglement in a diffusive nonintegrable system*, Phys. Rev. Lett. **(111), 127205 (2013)**.

[69] R. Pal and A. Lakshminarayan, *Entangling power of time-evolution operators in integrable and nonintegrable many-body systems*, Phys. Rev. B **(98), 174304 (2018)**

[70] B. Bertini, P. Kos, and T. Prosen,*Entanglement spreading in a minimal model of maximal many-body quantum chaos* , Phys. Rev. X **(9), 021033 (2019)**.

[71] , L. Piroli, B. Bertini, J. I. Cirac, and T. Prosen,*Exact dynamics in dual-unitary quantum circuits*, Phys. Rev. B *(101), 094304 (2020)*.

[72] S. Gopalakrishnan and A. Lamacraft, *Unitary circuits of finite depth and infinite width from quantum channels*, Phys. Rev. B **(100), 064309 (2019)**.

[73] A. Nahum, J. Ruhman, S. Vijay, and J. Haah, *Quantum entanglement growth under random unitary dynamics*, Phys. Rev. X **(7), 031016 (2017)**.

[74] T. Zhou and A. Nahum, *Entanglement membrane in chaotic many-body systems*, Phys. Rev. X **(10), 031066 (2020)**.

[75] P. Calabrese and J. Cardy, *Entanglement Entropy and Conformal Field Theory*, J. Phys. A: Math. Theor. **42**, 504005 (2009).

[76] P. Calabrese and J. Cardy, *Quantum Quenches in 1 + 1 Dimensional Conformal Field Theories*, J. Stat. Mech. (2016) 064003.

[77] L. Vidmar and M. Rigol, *Generalized Gibbs Ensemble in Integrable Lattice Models*, J. Stat. Mech. (2016) 064007.

[78] M. Takahashi, *Thermodynamics of one-dimensional solvable models* (2005).

[79] L. Piroli, B. Pozsgay, and E. Vernier, *What Is an Integrable Quench?*, Nucl. Phys. B **925**, 362 (2017).

[80] B. Pozsgay, L. Piroli, and E. Vernier, *Integrable Matrix Product States from Boundary Integrability*, SciPost Physics **6**, 062 (2019).

[81] G. Delfino, *Quantum Quenches with Integrable Pre-Quench Dynamics*, J. Phys. A: Math. Theor. **47**, 402001 (2014).

[82] G. Delfino and J. Viti, *On the Theory of Quantum Quenches in Near-Critical Systems*, J. Phys. A: Math. Theor. **50**, 084004 (2017).

[83] B. Bertini, E. Tartaglia, and P. Calabrese, *Entanglement and Diagonal Entropies after a Quench with No Pair Structure*, J. Stat. Mech. (2018) 063104.

[84] A. Bastianello and P. Calabrese, *Spreading of Entanglement and Correlations after a Quench with Intertwined Quasiparticles*, SciPost Phys. **5**, 033 (2018).

[85] A. Bastianello and M. Collura, *Entanglement spreading and quasiparticle picture beyond the pair structure*, SciPost Phys. **8**, 045 (2020).

[86] K. G. Wilson, *Confinement of quarks*, Phys. Rev. D **10**, 2445 (1974).

[87] J. Greensite, *An introduction to the confinement problem*, Springer (2011),vol. 821.

[88] U.-J. Wiese, *Ultracold quantum gases and lattice systems: quantum simulation of lattice gauge theories*, Annalen der Physik **525**, 777-796 (2013).

[89] M. Dalmonte and S. Montangero, *Lattice gauge theory simulations in the quantum information era* Contemp. Phys. **57**, 388-412 (2016).

[90] J. Preskill, *Simulating quantum field theory with a quantum computer*, PoS LATTICE2018, 024 (2019).

[91] M. C. Bañuls, R. Blatt, J. Catani, A. Celi, J. I. Cirac, M. Dalmonte, L. Fallani, K. Jansen, M. Lewenstein, S. Montangero, C. A. Muschik, B. Reznik, E. Rico, L. Tagliacozzo, K. Van Acoleyen, F. Verstraete, U.-J. Wiese, M. Wingate, J. Zakrzewski, and P. Zoller, *Simulating lattice gauge theories within quantum technologies*, Eur. Phys. J. D **74**, 165 (2020).

[92] T. M. R. Byrnes, P. Sriganesh, R. J. Bursill, and C. J. Hamer, *Density matrix renormalization group approach to the massive Schwinger model*, Phys. Rev. D **66**, 013002 (2002).

[93] M. C. Bañuls, K. Cichy, J. I. Cirac, K. Jansen, and H. Saito, *Matrix product states for lattice field theories*, PoS LATTICE 2013, 332 (2013).

[94] M. C. Bañuls, K. Cichy, J. I. Cirac, and K. Jansen, *The mass spectrum of the Schwinger model with matrix product states*, J. High Energy Phys. 11 (2013) 158.

[95] P. Silvi, E. Rico, T. Calarco, and S. Montangero, *Lattice gauge tensor networks*, New J. Phys. **16**, 103015, (2014).

[96] L. Tagliacozzo, A. Celi, and M. Lewenstein, *Tensor Networks for Lattice Gauge Theories with Continuous Groups*, Phys. Rev. X **4**, 041024 (2014).

[97] B. Buyens, J. Haegeman, K. Van Acoleyen, H. Verschelde, and F. Verstraete *Matrix Product States for Gauge Field Theories*, Phys. Rev. Lett. **113**, 091601 (2014).

[98] E. Rico, T. Pichler, M. Dalmonte, P. Zoller, and S. Montangero, *Tensor Networks for Lattice Gauge Theories and Atomic Quantum Simulation*, Phys. Rev. Lett. **112**, 201601 (2014).

[99] M. C. Bañuls and K. Cichy, *Review on novel methods for lattice gauge theories*, Rep. Prog. Phys. 83 024401 (2020).

[100] E. Zohar, J. I. Cirac, and B. Reznik, *Simulating Compact Quantum Electrodynamics with Ultracold Atoms: Probing Confinement and Nonperturbative Effects*, Phys. Rev. Lett. **109**, 125302 (2012).

[101] D. Banerjee, M. Bögli, M. Dalmonte, E. Rico, P. Stebler, U.-J. Wiese, and P. Zoller *Atomic Quantum Simulation of U(N) and SU(N) Non-Abelian Lattice Gauge Theories*, Phys. Rev. Lett. **110**, 125303 (2013).

[102] A. Mezzacapo, E. Rico, C. Sabín, I. L. Egusquiza, L. Lamata, and E. Solano, *Non-Abelian SU(2) Lattice Gauge Theories in Superconducting Circuits*, Phys. Rev. Lett. **115**, 240502 (2015).

[103] E. A. Martinez, C. A. Muschik, P. Schindler, D. Nigg, A. Erhard, M. Heyl, P. Hauke, M. Dalmonte, T. Monz, P. Zoller, and R. Blatt, *Real-time dynamics of lattice gauge theories with a few-qubit quantum computer*, Nature **534**, 516 (2016).

[104] F. M. Surace, P. P. Mazza, G. Giudici, A. Lerose, A. Gambassi, and M. Dalmonte, *Lattice Gauge Theories and String Dynamics in Rydberg Atom Quantum Simulators*, Phys. Rev. X **10**, 021041 (2020).

[105] Y. Atas, J. Zhang, R. Lewis, A. Jahanpour, J. F. Haase, and C. A. Muschik, *SU(2) hadrons on a quantum computer*, arxiv:2102.08920.

[106] Z. Davoudi, N. M. Linke, and G. Pagano, *Toward simulating quantum field theories with controlled phonon-ion dynamics: A hybrid analog-digital approach*, arxiv:2104.09346.

[107] B. M. McCoy and T. T. Wu, *Two-dimensional Ising field theory in a magnetic field: Breakup of the cut in the two-point function*, Phys. Rev. D **18**, 1259 (1978).

[108] N. Ishimura and H. Shiba, *Dynamical Correlation Functions of One-Dimensional Anisotropic Heisenberg Model with Spin 1/2. I: Ising-Like Antiferromagnets*, Progr. Theor. Phys. **63**, 743 (1980).

[109] F. Liu, R. Lundgren, P. Titum, G. Pagano, J. Zhang, C. Monroe, and A. V. Gorshkov, *Confined Quasiparticle Dynamics in Long-Range Interacting Quantum Spin Chains*, Phys. Rev. Lett. **122**, 150601 (2019).

[110] W. L. Tan, P. Becker, F. Liu, G. Pagano, K. S. Collins, A. De, L. Feng, H. B. Kaplan, A. Kyprianidis, R. Lundgren, W. Morong, S. Whitsitt, A. V. Gorshkov, and C. Monroe, *Observation of Domain Wall Confinement and Dynamics in a Quantum Simulator*, Nature Phys. **17**, 742 (2021)

[111] F. M. Surace and A. Lerose, *Scattering of mesons in quantum simulators*, New J. Phys. **23** (2021) 062001.

[112] P. I. Karpov, G. Y. Zhu, M. P. Heller, and M. Heyl, *Spatiotemporal dynamics of particle collisions in quantum spin chains*, arxiv:2011.11624.

[113] A. Milsted, J. Liu, J. Preskill, and G. Vidal, *Collisions of false-vacuum bubble walls in a quantum spin chain*, arxiv:2012.07243.

[114] A. Sinha, T. Chanda, and J. Dziarmaga, *Nonadiabatic dynamics across a first-order quantum phase transition: Quantized bubble nucleation*, Phys. Rev. B 103, L220302 (2021).

[115] R. J. Valencia Tortora, P. Calabrese, and M. Collura, *Relaxation of the order-parameter statistics and dynamical confinement*, arXiv:2005.01679 (2020).

[116] M. Rigobello, S. Notarnicola, G. Magnifico, and S. Montangero, *Entanglement generation in QED scattering processes*, arxiv:2105.03445.

[117] B. Lake, A. M. Tsvelik, S. Notbohm, D. A. Tennant, T. G. Perring, M. Reehuis, C. Sekar, G. Krabbes, and B. Büchner, *Confinement of fractional quantum number particles in a condensed-matter system*, Nature Phys. **6**, 50 (2010).

[118] C. M. Morris, R. Valdés Aguilar, A. Ghosh, S. M. Koohpayeh, J. Krizan, R. J. Cava, O. Tchernyshyov, T. M. McQueen, and N. P. Armitage, *Hierarchy of bound states in the one-dimensional ferromagnetic Ising chain $CoNb_2O_6$ investigated by high-resolution time-domain terahertz spectroscopy*, Phys. Rev. Lett. **112**, 137403 (2014).

[119] B. Grenier, S. Petit, V. Simonet, E. Canévet, L.-P. Regnault, S. Raymond, B. Canals, C. Berthier, and P. Lejay, *Longitudinal and transverse Zeeman ladders in the Ising-like chain antiferromagnet $BaCo_2V_2O_8$*, Phys. Rev. Lett. **114**, 017201 (2015).

[120] Z. Wang, M. Schmidt, A. K. Bera, A. T. M. N. Islam, B. Lake, A. Loidl, and J. Deisenhofer, *Spinon confinement in the one-dimensional Ising-like antiferromagnet $SrCo_2V_2O_8$*, Phys. Rev. B **91**, 140404 (2015).

[121] Z. Wang *et al.*, *From confined spinons to emergent fermions: Observation of elementary magnetic excitations in a transverse-field Ising chain*, Phys. Rev. B **94**, 125130 (2016).

[122] Z. Wang, J. Wu, W. Yang, A. K. Bera, D. Kamenskyi, A. T. M. N. Islam, S. Xu, J. M. Law, B. Lake, C. Wu, and A. Loidl, *Experimental observation of Bethe strings*, Nature **554**, 219 (2018).

[123] Z. Wang *et al.*, *Quantum Critical Dynamics of a Heisenberg-Ising Chain in a Longitudinal Field: Many-Body Strings versus Fractional Excitations*, Phys. Rev. Lett. **123**, 067202 (2019).

[124] G. Delfino, G. Mussardo, and P. Simonetti, *Non-integrable quantum field theories as perturbations of certain integrable models*, Nucl. Phys. B, **473**, 469 (1996).

[125] G. Delfino and G. Mussardo, *Non-integrable aspects of the multi-frequency Sine-Gordon model*, Nucl. Phys. B **516**, 675 (1998).

[126] S. B. Rutkevich, *Decay of the metastable phase in $d = 1$ and $d = 2$ Ising models*, Phys. Rev. B **60**, 14525 (1999).

[127] P. Fonseca and A. Zamolodchikov, *Ising field theory in a magnetic field: analytic properties of the free energy*, J. Stat. Phys. **110**, 527 (2003);
P. Fonseca and A. Zamolodchikov, *Ising spectroscopy I: Mesons at $T < T_c$*, arXiv:hep-th/0612304 (2006).

[128] M. J. Bhaseen and A. M. Tsvelik, *Aspects of Confinement in Low Dimensions*, in Ian Kogan memorial Volume, *From Fields to Strings: Circumnavigating Theoretical Physics*, 661 (2005).

[129] S. B. Rutkevich, *Large-n excitations in the ferromagnetic Ising field theory in a weak magnetic field: Mass spectrum and decay widths*, Phys. Rev. Lett. **95**, 250601 (2005).

[130] S. B. Rutkevich, *Energy Spectrum of Bound-Spinons in the Quantum Ising Spin-Chain Ferromagnet*, J. Stat. Phys. **131**, 917 (2008).

[131] S. B. Rutkevich, On the weak confinement of kinks in the one-dimensional quantum ferromagnet $CoNb_2O_6$, J. Stat. Mech. P07015 (2010).

[132] S. B. Rutkevich, *Radiative corrections to the quark masses in the ferromagnetic Ising and Potts field theories*, Nucl. Phys. B **923**, 608 (2017).

[133] F. B. Ramos, M. Lencses, J. C. Xavier, and R. G. Pereira, *Confinement and bound states of bound states in a transverse-field two-leg Ising ladder*, Phys. Rev. B **102**, 014426 (2020).

[134] L. Vanderstraeten, E. Wybo, N. Chepiga, F. Verstraete, and F. Mila, *Spinon confinement and deconfinement in spin-1 chains*, Phys. Rev. B **101**, 115138 (2020)

[135] K. Hida, *Haldane Gap in the Spin-1/2 Double Chain Heisenberg Antiferromagnet -Numerical Diagonalization and Projector Monte Carlo Study*, J. Phys. Soc. Jpn. **60**, 1347 (1991).

[136] D. G. Shelton, A. A. Nersesyan, and A. M. Tsvelik, *Antiferromagnetic spin ladders: Crossover between spin s=1/2 and s=1 chains*, Phys. Rev. B **53**, 8521 (1996).

[137] H. J. Schulz, *Dynamics of Coupled Quantum Spin Chains*, Phys. Rev. Lett. **77**, 2790 (1996).

[138] F. H. L. Essler, A.M. Tsvelik, and G. Delfino, *Quasi-one-dimensional spin-1/2 Heisenberg magnets in their ordered phase: Correlation functions*, Phys. Rev. B **56**, 11001 (1997).

[139] A. W. Sandvik, *Multichain Mean-Field Theory of Quasi-One-Dimensional Quantum Spin Systems*, Phys. Rev. Lett. **83**, 3069 (1999).

[140] A. A. Nersesyan and A. M. Tsvelik, *One-Dimensional Spin-Liquid without Magnon Excitations*, Phys. Rev. Lett. **78**, 3939 (1997).

[141] I. Affleck, *Soliton confinement and the excitation spectrum of spin-Peierls antiferromagnets*, In *Dynamical Properties of Unconventional Magnetic Systems*, 123 Springer (1998).

[142] D. Augier, E. So, J. Riera, and D. Poilblanc, *Soliton bound states in the Raman spectrum of pure and doped spin-Peierls chains*, Phys. Rev. B **60**, 1075 (1999).

[143] M. Greiter, *Two-leg t-J ladder: A spin liquid generated by Gutzwiller projection of magnetic bands*, Phys. Rev. B **65**, 134443 (2002).

[144] M. Greiter, *Fictitious flux confinement: Magnetic pairing in coupled spin chains or planes*, Phys. Rev. B **66**, 054505 (2002).

[145] Z. Zhang, K. Amelin, X. Wang, H. Zou, J. Yang, U. Nagel, T. Rõõm, T. Dey, A. A. Nugroho, T. Lorenz, J. Wu, Z. Wang, *Observation of E8 Particles in an Ising Chain Antiferromagnet*, Phys. Rev. B **101**, 220411(R) (2020)

[146] K. Amelin, J. Engelmayer, J. Viirok, U. Nagel, T. Rõõm, T. Lorenz, Z. Wang, *Experimental Observation of High-Energy E_8 Particles in the Ising Chain Ferromagnet $CoNb_2O_6$*, Phys. Rev. B **102**, 104431 (2020).

[147] A. B. Zamolodchikov, *Integrals of motion and S-matrix of the (scaled) $T = T_c$ Ising model with magnetic field*, Int. J. Mod. Phys. A 4, 4235 (1989).

[148] Z. Cai, C. Wu, and U. Schollwöck, *Confinement: A real-time visualization*, Phys. Rev. B **85**, 075102 (2012).

[149] A. J. A. James, R. M. Konik, and N. J. Robinson, *Nonthermal States Arising from Confinement in One and Two Dimensions*, Phys. Rev. Lett. **122**, 130603 (2019).

[150] N. J. Robinson, A. J. A. James, and R. M. Konik, *Signatures of rare states and thermalization in a theory with confinement*, Phys. Rev. B **99**, 195108 (2019).

[151] R. Verdel, F. Liu, S. Whitsitt, A. V. Gorshkov, and M. Heyl, *Real-time dynamics of string breaking in quantum spin chains*, Phys. Rev. B **102**, 014308 (2020).

[152] T. Chanda, J. Zakrzewski, M. Lewenstein, and L. Tagliacozzo, *Confinement and Lack of Thermalization After Quenches in the Bosonic Schwinger Model*, Phys. Rev. Lett. **124**, 180602 (2020).

[153] P. P. Mazza, G. Perfetto, A. Lerose, M. Collura, and A. Gambassi, *Suppression of transport in nondisordered quantum spin chains due to confined excitations*, Phys. Rev. B **99**, 180302(R) (2019).

[154] A. Lerose, F. M. Surace, P. P. Mazza, G. Perfetto, M. Collura, and A. Gambassi, *Quasilocalized dynamics from confinement of quantum excitations*, Phys. Rev. B **102**, 041118(R) (2020).

[155] O. A Castro-Alvaredo, M. Lencsés, I. M. Szécsényi, and J. Viti, *Entanglement oscillations near a quantum critical point*, arXiv:2001.10007 (2020).

[156] R. C. Myers, M. Rozali, and B. Way, *Holographic quenches in a confined phase*, J. Phys. A **50**, 494002 (2017).

[157] A. Cortes Cubero and N. J. Robinson, *Lack of thermalization in $(1+1)$-d quantum chromodynamics at large N_c*, J. Stat. Mech. (2019) 123101.

[158] O. Pomponio, M.A. Werner, G. Zarand, and G. Takacs, *Bloch oscillations and the lack of the decay of the false vacuum in a one-dimensional quantum spin chain*, arviv:2105.00014.

[159] A. Bastianello, U. Borla, and S. Moroz, *Fragmentation and emergent integrable transport in the weakly tilted Ising chain*, arviv:2108.04845.

[160] S. Pai and M. Pretko, *Fractons from confinement in one dimension*, Phys. Rev. Res. **2**, 013094 (2020).

[161] G. Magnifico, M. Dalmonte, P. Facchi, S. Pascazio, F. V. Pepe, and E. Ercolessi, *Real time dynamics and confinement in the $\mathbb{Z}_n$ Schwinger-Weyl lattice model for $1+1$ QED*, Quantum **4**, 281 (2020).

[162] F. Hebenstreit, J. Berges, and D. Gelfand, *Real-Time Dynamics of String Breaking*, Phys. Rev. Lett. **111**, 201601 (2013).

[163] T. Pichler, M. Dalmonte, E. Rico, P. Zoller, and S. Montangero, *Real-Time Dynamics in $U(1)$ Lattice Gauge Theories with Tensor Networks*, Phys. Rev. X **6**, 011023 (2016).

[164] J. Vovrosh and J. Knolle, *Confinement and entanglement dynamics on a digital quantum computer*, Sci. Rep. **11**, 11577 (2021).

[165] P.Calabrese, F.H.L. Essler, and M.Fagotti, *Quantum Quench in the Transverse-Field Ising Chain*, Phys. Rev. Lett. **106**, 227203 (2011)

[166] D. A. Tennant, T. G. Perring, R. A. Cowley, and S. E. Nagler, *Unbound spinons in the S=1/2 antiferromagnetic chain $KCuF_3$*, Phys. Rev. Lett. **70**, 4003(1993).

[167] D. A. Tennant, R. A. Cowley, S. E. Nagler, and A. M. Tsvelik, *Measurement of the spin-excitation continuum in one-dimensional $KCuF_3$ using neutron scattering*, D. A. Tennant, R. A. Cowley, S. E. Nagler, and A. M. Tsvelik, *Measurement of the spin-excitation continuum in one-dimensional $KCuF_3$ using neutron scattering*, Phys. Rev. B **52**, 13368 (1995).

[168] S. K. Satija, J. D. Axe, G. Shirane, H. Yoshizawa, and K. Hirakawa, *Neutron scattering study of spin waves in one-dimensional antiferromagnet $KCuF_3$*, Phys. Rev. B **21**, 2001 (1980).

[169] T. Ami, M. K. Crawford, R. L. Harlow, Z. R. Wang, D. C. Johnston, Q. Huang, and R. W. Erwin, *Magnetic susceptibility and low-temperature structure of the linear chain cuprate Sr_2CuO_3*, Phys. Rev. B **51**, 5994 (1995).

[170] B. Schmidt, P. Thalmeier, and P. Fulde, *Excitations in spin chains and specific-heat anomalies in Yb_4As_3*, EPL **35**, 109 (1996).

[171] F.D.M. Haldane, *Continuum dynamics of the 1-D Heisenberg antiferromagnet: Identification with the O(3) nonlinear sigma model*, Phys. Lett. A **93**, 464-468 (1983);
F.D.M. Haldane, *Nonlinear Field Theory of Large-Spin Heisenberg Antiferromagnets: Semiclassically Quantized Solitons of the One-Dimensional Easy-Axis Néel State* Phys. Rev. Lett. **50**, 1153(1983).

[172] H. Shiba, *Quantization of Magnetic Excitation Continuum due to inter-chain Coupling in Nearly One-Dimensional Ising-like Antiferromagnets*, Progress Theor. Phys. **64**, 743 (1980).

[173] W. B. Yelon, D. E. Cox, and M. Eibschütz, *Magnetic ordering in $CsCoBr_3$*, Phys. Rev. B **12**, 5007 (1975).

[174] N. Achiwa, *Linear Antiferromagnetic Chains in Hexagonal ABCl3-Type Compounds (A; Cs, or Rb, B; Cu, Ni, Co, or Fe)*, J. Phys. Soc. Jpn. **27**, 561 (1969).

[175] P. Jung, R. W. Helmes, and A. Rosch, *Transport in Almost Integrable Models: Perturbed Heisenberg Chains*, Phys. Rev. Lett. **96**, 067202 (2006).

[176] R. Steinigeweg, J. Herbrych, X. Zotos, and W. Brenig, *Heat conductivity of the Heisenberg spin-1/2 ladder: From weak to strong breaking of integrability*, Phys. Rev. Lett. **116**, 017202 (2015).

[177] A. K. Bera, B. Lake, F. H. L. Essler, L. Vanderstraeten, C. Hubig, U. Schollwock, A. T. M. N. Islam, A. Schneidewind, and D. L. Quintero-Castro, *Spinon confinement in a quasi one dimensional anisotropic Heisenberg magnet*, Phys. Rev. B **96**, 054423 (2017).

[178] T. Tonegawa, T. Hikihara, K. Okamoto, S. C. Furuya, and T. Sakai, *Ground-State Phase Diagram of an Anisotropic S = 1/2 Ladder with Different Leg Interactions*, J. Phys. Soc. Jpn. **87**, 104002 (2018).

[179] S. B. Rutkevich, *Kink confinement in the antiferromagnetic XXZ spin-(1/2) chain in a weak staggered magnetic field*, EPL **121**, 37001 (2018).

[180] T. Suzuki and S. I. Suga, *Quantized excitation spectra by magnon confinement in quasi-one-dimensional S = 1 spin systems*, Phys. Rev. B **98**, 180406 (2018).

[181] Y. Fan, J. Yang, W. Yu, J. Wu, and R. Yu, *Phase diagram and quantum criticality of Heisenberg spin chains with Ising anisotropic interchain couplings*, Phys. Rev. Res. **2**, 013345 (2020).

[182] H. Zou, Y. Cui, X. Wang, Z. Zhang, J. Yang, G. Xu, A. Okutani, M. Hagiwara, M. Matsuda, G. Wang, G. Mussardo, K. Hódsági, M. Kormos, Z. Z. He, S. Kimura, R. Yu, W. Yu, J. Ma, J. Wu, *E_8 Spectra of Quasi-One-Dimensional Antiferromagnet* $BaCo_2V_2O_8$ *under Transverse Field*, Phys. Rev. Lett. **127**, 077201 (2021)

[183] J. Simon, W. S. Bakr, R. Ma, M. E. Tai, P. M. Preiss, and M. Greiner, *Quantum simulation of antiferromagnetic spin chains in an optical lattice*, Nature **472**, 307 (2011).

[184] G. Pagano, M. Mancini, G. Cappellini, P. Lombardi, F. Schafer, H. Hu, X.-J. Liu, J. Catani, C. Sias, M. Inguscio, and L. Fallani, *A one-dimensional liquid of fermions with tunable spin*, Nature Phys. **10**, 198 (2014).

[185] A. Zabrodin, *Integrable Models of Field Theory and Scattering on Quantum Hyperboloids*, Mod. Phys. Lett. A **7**, 441 (1992).

[186] G. Vidal, *Classical Simulation of Infinite-Size Quantum Lattice Systems in One Spatial Dimension*, Phys. Rev. Lett. **98**, 070201 (2007).

[187] E. H. Lieb and D. W. Robinson, *The finite group velocity of quantum spin system*, Commun. Math. Phys. **28**, 251 (1972).

[188] L. Bonnes, F. H. L. Essler, and A. M. Läuchli, "Light-Cone" Dynamics After Quantum Quenches in Spin Chains, Phys. Rev. Lett. **113**, 187203 (2014).

[189] P. Barmettler, M. Punk, V. Gritsev, E. Demler, and E. Altman, *Quantum quenches in the anisotropic spin-1/2 Heisenberg chain: different approaches to many-body dynamics far from equilibrium*, New J. Phys. **12** 055017 (2010)

[190] S. Choi, C. J. Turner, H. Pichler, W. W. Ho, A. A. Michailidis, Z. Papic, M. Serbyn, M. D. Lukin, and D. A. Abanin, *Emergent SU(2) dynamics and perfect quantum many-body scars*,Phys. Rev. Lett. **122**, 220603 (2019)

[191] J. D. Johnson, S. Krinsky, and B. M. McCoy, *Vertical-Arrow Correlation Length in the Eight-Vertex Model and the Low-Lying Excitations of the XYZ Hamiltonian*, Phys. Rev. A **8**, 2526 (1973).

[192] S. Coleman, *Fate of the false vacuum: Semiclassical theory*, Phys. Rev. D **15**, 2929 (1977), Erratum Phys. Rev. D **16**, 1248 (1977).

[193] C. G. Callan and S. Coleman, *Fate of the false vacuum. II. First quantum corrections*, Phys. Rev. D **16**, 1762 (1977).

[194] S. Coleman and F. De Luccia, *Gravitational effects on and of vacuum decay*, Phys. Rev. D **21**, 3305 (1980)

[195] M. S. Turner and F. Wilczek, *Is our vacuum metastable?*, Nature **298**, 633 (1982).

[196] S. Sachdev, *Quantum Phase Transitions*, Cambridge University Press (2001).

[197] G. Mussardo, Statistical Field Theory: An Introduction to Exactly Solved Models in Statistical Physics, Oxford Graduate Texts (Oxford University Press, 2010).

[198] D. Banerjee, M. Dalmonte, M. Müller, E. Rico, P. Stebler, U.-J. Wiese, and P. Zoller, *Atomic Quantum Simulation of Dynamical Gauge Fields Coupled to Fermionic Matter: From String Breaking to Evolution After a Quench*, Phys. Rev. Lett. **109**, 175302 (2012).

[199] S. Kühn, E. Zohar, J. I. Cirac, and M. C. Banuls, *Non-abelian string breaking phenomena with matrix product states*, J. High Energy Phys. 07 (2015) 130.

[200] V. Kasper, F. Hebenstreit, M. K. Oberthaler, and J. Berges, *Schwinger pair production with ultracold atoms*, Phys. Lett. B **760**, 742 (2016).

[201] B. Buyens, J. Haegeman, F. Hebenstreit, F. Verstraete, and K. Van Acoleyen, *Real-time simulation of the Schwinger effect with matrix product states*, Phys. Rev. D **96**, 114501 (2017).

[202] Y. Kuno, S. Sakane, K. Kasamatsu, I. Ichinose, and T. Matsui, *Quantum simulation of* $(1+1)$*-dimensional* $U(1)$ *gauge-Higgs model on a lattice by cold bose gases*, Phys. Rev. D **95**, 094507 (2017).

[203] P. Sala, T. Shi, S. Kühn, M. C. Bañuls, E. Demler, and J. I. Cirac, *Variational study of U(1) and SU(2) lattice gauge theories with gaussian states in* $1+1$ *dimensions*, Phys. Rev. D **98**, 034505 (2018).

[204] D. Spitz and J. Berges, *Schwinger pair production and string breaking in non-abelian gauge theory from real-time lattice improved Hamiltonians*, Phys. Rev. D **99**, 036020 (2019).

[205] J. Park, Y. Kuno, and I. Ichinose, *Glassy dynamics from quark confinement: Atomic quantum simulation of the gauge-Higgs model on a lattice*, Phys. Rev. A **100**, 013629 (2019).

[206] G. Münster and S.B. Rutkevich, *The classical nucleation rate in two dimensions*, Eur. Phys. J. C **27**, 297-303 (2003).

[207] M. B. Voloshin, *Decay of false vacuum in (1+1) dimensions*, ITEP–8(1985) USSR.

[208] S. Notarnicola, M. Collura, and S. Montangero, *Real time dynamics quantum simulation of* $(1+1)$*-d lattice QED with Rydberg atoms*, Phys. Rev. Res. **2**, 013288 (2020).

[209] C. Monroe, W. C. Campbell, L.-M. Duan, Z.-X. Gong, A. V. Gorshkov, P. W. Hess, R. Islam, K. Kim, N. M. Linke, G. Pagano, P. Richerme, C. Senko, and N. Y. Yao, *Programmable quantum simulations of spin systems with trapped ions*, Rev. Mod. Phys. **93**, 025001 (2021).

[210] L. Amico, R. Fazio, A. Osterloh, and V. Vedral,*Entanglement in many-body systems*, Rev. Mod. Phys. **80**, 517 (2008) .

[211] P. Calabrese, J. Cardy, and B. Doyon, *Entanglement entropy in extended quantum systems*, J. Phys. A: Math. Theor. **42**, 500301 (2009).

[212] V. Alba and P. Calabrese, *Quench action and Rényi entropies in integrable systems*, Phys. Rev. B **96**, 115421 (2017).

[213] V. Alba and P. Calabrese, *Rényi entropies after releasing the Néel state in the XXZ spin-chain*, J. Stat. Mech. (2017) 113105.

[214] M. Mestyán, V. Alba, and P. Calabrese, *Rényi entropies of generic thermodynamic macrostates in integrable systems*, J. Stat. Mech. (2018) 083104.

[215] T. Rakovszky, F. Pollmann, and C. W. von Keyserlingk, *Sub-ballistic growth of R´enyi entropies due to diffusion*, Phys. Rev. Lett. 122, 250602 (2019).

[216] Y. Huang, *Dynamics of Rényi entanglement entropy in diffusive qudit systems*, IOP SciNotes **1**, 035205 (2020).

[217] M. Žnidarič, *Entanglement growth in diffusive systems*, Commun. Phys. **3**, 1 (2020).

[218] J. Maldacena, *The Large-N Limit of Superconformal Field Theories and Supergravity*, Int. J. Theor. Phys. **38**, 1113 (1999).

[219] W. Israel, *Thermo-Field Dynamics of Black Holes*, Phys. Lett. A **57**, 107 (1976).

[220] J. Maldacena, *Eternal Black Holes in Anti-de Sitter*, JHEP (2003) 021.

[221] S. H. Shenker and D. Stanford, *Black Holes and the Butterfly Effect*, JHEP (2014) 67.

[222] S. H. Shenker and D. Stanford, *Multiple Shocks*, JHEP (2014) 46.

[223] D. A. Roberts, D. Stanford, and L. Susskind, *Localized Shocks*, JHEP (2015) 51.

[224] D. Stanford and L. Susskind, *Complexity and Shock Wave Geometries*, Phys. Rev. D **90**, 126007 (2014).

[225] L. Susskind, *Entanglement Is Not Enough*, Fortschritte Der Physik **64**, 49 (2016).

[226] L. Susskind, *Addendum to Computational Complexity and Black Hole Horizons*, Fortschritte Der Physik **64**, 44 (2016).

[227] A. R. Brown, D. A. Roberts, L. Susskind, B. Swingle, and Y. Zhao, *Complexity, Action, and Black Holes*, Phys. Rev. D **93**, 086006 (2016).

[228] A. R. Brown, D. A. Roberts, L. Susskind, B. Swingle, and Y. Zhao, *Holographic Complexity Equals Bulk Action?*, Phys. Rev. Lett. **116**, 191301 (2016).

[229] R.-Q. Yang, *Complexity for Quantum Field Theory States and Applications to Thermofield Double States*, Phys. Rev. D **97**, 066004 (2018).

[230] R. Q. Yang, C. Niu, C. Y. Zhang, and K. Y. Kim, *Comparison of Holographic and Field Theoretic Complexities for Time Dependent Thermofield Double States*, JHEP (2018) 82.

[231] S. Chapman, J. Eisert, L. Hackl, M. P. Heller, R. Jefferson, H. Marrochio, and R. C. Myers, *Complexity and Entanglement for Thermofield Double States*, SciPost Phys. **6**, 034 (2019).

[232] J. Jiang and X. Liu, *Circuit Complexity for Fermionic Thermofield Double States*, Phys. Rev. D **99**, 026011 (2019).

[233] M. Doroudiani, A. Naseh, and R. Pirmoradian, *Complexity for Charged Thermofield Double States*, JHEP (2020) 120.

[234] S. Chapman and H. Z. (Vincent) Chen, *Charged Complexity and the Thermofield Double State*, JHEP (2021) 187.

[235] U. Schollwöck, *The Density-Matrix Renormalization Group in the Age of Matrix Product States*, Ann. Phys. **326**, 96 (2011).

[236] T. Hartman and J. Maldacena, *Time Evolution of Entanglement Entropy from Black Hole Interiors*, JHEP (2013) 14.

[237] Y. Gu, A. Lucas, and X.-L. Qi, *Spread of Entanglement in a Sachdev-Ye-Kitaev Chain*, JHEP (2017) 120.

[238] M. Mezei, *On Entanglement Spreading from Holography*, JHEP (2017) 64.

[239] M. Mezei, *Membrane Theory of Entanglement Dynamics from Holography*, Phys. Rev. D **98**, 106025 (2018).

[240] M. Ghasemi, A. Naseh, and R. Pirmoradian, *Odd Entanglement Entropy and Logarithmic Negativity for Thermofield Double States*, JHEP (2021) 128.

[241] P. Zanardi, *Entanglement of Quantum Evolutions*, Phys. Rev. A **63**, 040304 (2001).

[242] P. Hosur, X.-L. Qi, D. A. Roberts, and B. Yoshida, *Chaos in Quantum Channels*, JHEP (2016) 4.

[243] T. Zhou and D. J. Luitz, *Operator Entanglement Entropy of the Time Evolution Operator in Chaotic Systems*, Phys. Rev. B **95**, 094206 (2017).

[244] C. Sünderhauf, L. Piroli, X. L. Qi, N. Schuch, and J. I. Cirac, *Quantum Chaos in the Brownian SYK Model with Large Finite N: OTOCs and Tripartite Information*, JHEP (2019) 038.

[245] O. Schnaack, N. Bölter, S. Paeckel, S. R. Manmana, S. Kehrein, and M. Schmitt, *Tripartite Information, Scrambling, and the Role of Hilbert Space Partitioning in Quantum Lattice Models*, Phys. Rev. B **100**, 224302 (2019).

[246] B. Bertini and L. Piroli, *Scrambling in Random Unitary Circuits: Exact Results*, Phys. Rev. B **102**, 064305 (2020).

[247] Z. Gong, L. Piroli, and J. I. Cirac, *Topological Lower Bound on Quantum Chaos by Entanglement Growth*, Phys. Rev. Lett. **126**, 160601 (2021).

[248] G. Styliaris, N. Anand, and P. Zanardi, *Information Scrambling over Bipartitions: Equilibration, Entropy Production, and Typicality*, Phys. Rev. Lett. **126**, 030601 (2021).

[249] G. Vidal, J. I. Latorre, E. Rico, and A. Kitaev, *Entanglement in Quantum Critical Phenomena*, Phys. Rev. Lett. **90**, 227902 (2003).

[250] F. Franchini, *An introduction to integrable techniques for one-dimensional quantum systems* (Springer, 2017).

[251] V. E. Korepin, N. M. Bogoliubov, and A. G. Izergin, *Quantum inverse scattering method and correlation functions* (Cambridge university press, 1997).

[252] L. Piroli, B. Pozsgay, and E. Vernier, *From the quantum transfer matrix to the quench action: The Loschmidt echo in XXZ Heisenberg spin chains*, J. Stat. Mech.: Theory Exp. **2017** (2), 023106.

[253] L. Piroli, B. Pozsgay, and E. Vernier, *Non-Analytic Behavior of the Loschmidt Echo in XXZ Spin Chains: Exact Results*, Nucl. Phys. B **933**, 454 (2018).

[254] D. Perez-Garcia, F. Verstraete, M. M. Wolf, and J. I. Cirac, *Matrix Product State Representations*, arXiv:Quant-Ph/0608197 (2006).

[255] J. Dubail, *Entanglement scaling of operators: a conformal field theory approach, with a glimpse of simulability of long-time dynamics in 1+1d*, J. Phys. A **50**, 234001 (2017).

[256] M. Ippoliti, T. Rakovszky, and V. Khemani, *Fractal, logarithmic, and volume-law entangled nonthermal steady states via spacetime duality*, Phys. Rev. X 12, 011045 (2022).

[257] B. Bertini, P. Kos, and T. Prosen, *Exact correlation functions for dual-unitary lattice models in 1 + 1 dimensions*, Phys. Rev. Lett. **123**, 210601 (2019).

[258] A. B. Zamolodchikov and A. B. Zamolodchikov, *Factorized S-matrices in two dimensions as the exact solutions of certain relativistic quantum field theory models*, Ann. Phys. **120**, 253 (1979).

[259] A. Zamolodchikov, *Thermodynamic Bethe ansatz in relativistic models: Scaling 3-state Potts and Lee-Yang models*, Nucl. Phys. B 342, 695 (1990).

[260] S. Ghoshal and A. Zamolodchikov, *Boundary S-matrix and boundary state in two-dimensional integrable quantum field theory*, Int. J. Mod. Phys. A **09**, 3841 (1994).

[261] C. N. Yang and C. P. Yang, *Thermodynamics of a one-dimensional system of bosons with repulsive deltafunction interaction*, J. Math. Phys. **10**, 1115 (1969).

[262] M. Takahashi, Thermodynamics of one-dimensional solvable models (Cambridge University Press, 1999).

[263] S. J. van Tongeren, *Introduction to the thermodynamic Bethe ansatz*, J. Phys. A: Math. Theor. **49**, 323005 (2016).

[264] M. Ippoliti and V. Khemani, *Postselection-free entanglement dynamics via space-time duality*, Phys. Rev. Lett. **126**, 060501 (2021)

[265] B. Bertini, P. Kos, and T. Prosen, *Exact spectral formfactor in a minimal model of many-body quantum chaos* , Phys. Rev. Lett. **121**, 264101 (2018).

[266] T.-C. Lu and T. Grover, *Spacetime duality between localization transitions and measurement-induced transitions*, PRX Quantum 2, 040319 (2021).

[267] S. J. Garratt and J. T. Chalker, *Many-body delocalization as symmetry breaking*, Phys. Rev. Lett. **127** ,026802 (2021).

[268] B. Bertini, K. Klobas, and T.-C. Lu,*Dynamics of entanglement negativity in quantum circuits: Exact results from space-time duality*, in preparation (2022).

[269] M. Bañuls, M. B. Hastings, F. Verstraete, and J. I. Cirac, *Matrix product states for dynamical simulation of infinite chains*, Phys. Rev. Lett. **102**, 240603 (2009).

[270] A. Müller-Hermes, J. I. Cirac, and M. C. Bañuls, *Tensor network techniques for the computation of dynamical observables in one-dimensional quantum spin systems*, New J. Phys. **14**, 075003 (2012).

[271] M. B. Hastings and R. Mahajan, *Connecting entanglement in time and space: Improving the folding algorithm*, Phys. Rev. A 91, 032306 (2015).

[272] A. Lerose, M. Sonner, and D. A. Abanin, *Influence matrix approach to many-body Floquet dynamics*, Phys. Rev. X 11, 021040 (2021).

[273] A. Lerose, M. Sonner, and D. A. Abanin, *Scaling of temporal entanglement in proximity to integrability*, Phys.Rev. B **104**, 035137 (2021)

[274] M. Sonner, A. Lerose, and D. A. Abanin, *Influence functional of many-body systems: Temporal entanglement and matrix-product state representation*, Ann. Physics **435**, 168677 (2021).

[275] M. Sonner, A. Lerose, and D. A. Abanin, *Characterizing many-body localization via exact disorder-averaged quantum noise*, Phys. Rev. B **105**, L020203 (2022).

[276] G. Giudice, G. Giudici, M. Sonner, J. Thoenniss, A. Lerose, D. A. Abanin, and L. Piroli, *Temporal entanglement, quasiparticles and the role of interactions*, 2112.14264 (2021), arXiv:2112.14264

[277] G. Arutyunov and S. Frolov, *On string S-matrix, bound states and TBA*, J. High Energy Phys. **2007** (12), 024

[278] G. Arutyunov and S. Frolov, *Thermodynamic Bethe ansatz for the AdS5×S5 mirror model*, J. High Energy Phys. **2009** (05), 068.

[279] O. A. Castro-Alvaredo, B. Doyon, and T. Yoshimura, *Emergent hydrodynamics in integrable quantum systems out of equilibrium*, Phys. Rev. X 6, 041065 (2016).

[280] D. Fioretto and G. Mussardo, *Quantum quenches in integrable field theories*, New J. Phys. 12, 055015 (2010).

[281] B. Bertini, D. Schuricht, and F. H. L. Essler, *Quantum quench in the sine-Gordon model*, J. Stat. Mech.: Theory Exp. 2014 (10), P10035.

[282] B. Bertini, L. Piroli, and P. Calabrese, *Quantum quenches in the sinh-Gordon model: Steady state and one-point correlation functions*, J. Stat. Mech.: Theory Exp. 2016 (6), 063102.

[283] B. Bertini, M. Collura, J. De Nardis, and M. Fagotti, *Transport in out-of-equilibrium XXZ chains: Exact profiles of charges and currents*, Phys. Rev. Lett. **117**, 207201 (2016).

[284] S. Sotiriadis, G. Takács, and G. Mussardo, *Boundary state in an integrable quantum field theory out of equilibrium*, Phys. Lett. B **734**, 52 (2014).

[285] D. Horváth, S. Sotiriadis, and G. Takács, *Initial states in integrable quantum field theory quenches from an integral equation hierarchy*, Nucl. Phys. B **902**, 508 (2016).

[286] B. Pozsgay, *The dynamical free energy and the f Heisenberg spin chain*, J. Stat. Mech.: Theory Exp. **2013** (10), P10028.

[287] L. Piroli, E. Vernier, P. Calabrese, and B. Pozsgay, *Integrable quenches in nested spin chains I: The exact steady states*, J. Stat. Mech.: Theory Exp. 2019 (6), 063103.

[288] L. Piroli, E. Vernier, P. Calabrese, and B. Pozsgay, *Integrable quenches in nested spin chains II: Fusion of boundary transfer matrices*, J. Stat. Mech.: Theory Exp. 2019 (6), 063104.

[289] E. K. Sklyanin, *Boundary conditions for integrable quantum systems*, J. Phys. A: Math. Theor. **21**, 2375 (1988)

[290] A. Bobenko, M. Bordemann, C. Gunn, and U. Pinkall, *On two integrable cellular automata*, Commun. Math. Phys. **158**, 127 (1993).

[291] B. Buča, K. Klobas, and T. Prosen, *Rule 54: Exactly solvable model of nonequilibrium statistical mechanics*, J. Stat. Mech.: Theory Exp. **2021** (7), 074001.

[292] T. Prosen and C. Mejía-Monasterio, *Integrability of a deterministic cellular automaton driven by stochastic boundaries*, J. Phys. A: Math. Theor. **49**, 185003 (2016).

[293] T. Prosen and B. Buča, *Exact matrix product decay modes of a boundary driven cellular automaton*, J. Phys. A: Math. Theor. **50**, 395002 (2017).

[294] A. Inoue and S. Takesue, *Two extensions of exact nonequilibrium steady states of a boundary-driven cellular automaton*, J. Phys. A: Math. Theor. 51, 425001 (2018).

[295] B. Buča, J. P. Garrahan, T. Prosen, and M. Vanicat,*Exact large deviation statistics and trajectory phase transition of a deterministic boundary driven cellular automaton*, Phys. Rev. E **100**, 020103(R) (2019).

[296] K. Klobas, M. Medenjak, T. Prosen, and M. Vanicat, *Time-dependent matrix product ansatz for interacting reversible dynamics*, Commun. Math. Phys. **371**, 651 (2019).

[297] K. Klobas, M. Vanicat, J. P. Garrahan, and T. Prosen, *Matrix product state of multi-time correlations*, J. Phys. A: Math. Theor. 53, 335001 (2020).

[298] K. Klobas and T. Prosen, *Space-like dynamics in a reversible cellular automaton*, SciPost Phys. Core **2**, 10 (2020).

[299] S. Gopalakrishnan and B. Zakirov, *Facilitated quantum cellular automata as simple models with non-thermal eigenstates and dynamics* ,Quantum Science Tech. **3**, 044004 (2018).

[300] S. Gopalakrishnan, *Operator growth and eigenstate entanglement in an interacting integrable Floquet system* ,Phys. Rev. B **98**, 060302(R) (2018).

[301] S. Gopalakrishnan, D. A. Huse, V. Khemani, and R. Vasseur, *Hydrodynamics of operator spreading and quasiparticle diffusion in interacting integrable systems*,Phys. Rev. B **98**, 220303(R) (2018).

[302] A. J. Friedman, S. Gopalakrishnan, and R. Vasseur, *Integrable many-body quantum Floquet-Thouless pumps*, Phys. Rev. Lett. **123**, 170603 (2019).

[303] V. Alba, J. Dubail, and M. Medenjak, *Operator entanglement in interacting integrable quantum systems: The case of the Rule 54 chain*, Phys. Rev. Lett. **122**, 250603 (2019).

[304] V. Alba, *Diffusion and operator entanglement spreading*, Phys. Rev. B **104**, 094410 (2021).

[305] J. Lopez-Piqueres, S. Gopalakrishnan, and R. Vasseur, *Integrability breaking in the Rule 54 cellular automaton*, 2203.05426 (2022), arXiv:2203.05426

[306] J. S. Caux, *The quench action*, https://doi.org/10.1088/1742-5468/2016/06/064006J. Stat. Mech.: Theory Exp. **2016** (6), 064006.

[307] B. Pozsgay, *Overlaps with arbitrary two-site states in the XXZ spin chain*, J. Stat. Mech.: Theory Exp. **2018** (5), 053103.

[308] O. A. Castro-Alvaredo, M. Lencsés, I. M. Szécsényi, and J. Viti, *Entanglement dynamics after a quench in Ising field theory: a branch point twist field approach*, J. High Energy Phys. **2019** (12), 1.

[309] M. Brenes, M. Dalmonte, M. Heyl, and A. Scardicchio, *Many-Body Localization Dynamics from Gauge Invariance*, Phys. Rev. Lett. **120**, 030601 (2018)

[310] J. Vovrosh and J. Knolle, *Confinement Dynamics on a Digital Quantum Computer*, arXiv:2001.03044.

[311] A. LeClair, A. W. W. Ludwig, and G. Mussardo, *Integrability of coupled conformal field theories*, Nucl. Phys. B **512**, 523 (1998).

[312] A. J. Daley, H. Pichler, J. Schachenmayer and P. Zoller, *Measuring Entanglement Growth in Quench Dynamics of Bosons in an Optical Lattice*, Phys. Rev. Lett. **109**, 020505 (2012).

[313] A. Elben, B. Vermersch, M. Dalmonte, J.I. Cirac and P. Zoller, *Rényi Entropies from Random Quenches in Atomic Hubbard and Spin Models*, Phys. Rev. Lett. **120**, 050406 (2018).

[314] M. Brockmann, B. Wouters, D. Fioretto, J. D. Nardis, R. Vlijm, and J.-S. Caux, *Quench action approach for releasing the Néel state into the spin-1/2 XXZ chain*, J. Stat. Mech.: Theory Exp. **2014** (12), P12009.

[315] M. Vanicat, L. Zadnik, and T. Prosen, *Integrable Trotterization: Local conservation laws and boundary driving*, Phys. Rev. Lett. 121, 030606 (2018).

[316] M. Lencses, O. Pomponio, and G. Takacs, *Relaxation and entropy generation after quenching quantum spin chains*, SciPost Phys. 9, 11 (2020).

[317] S. Murciano, P. Calabrese, and R. M. Konik, *Postquantum quench growth of renyi entropies in perturbed luttinger liquids* ,arXiv:2112.04412 (2021).

[318] L. Piroli, E. Vernier, M. Collura, and P. Calabrese, *Thermodynamic symmetry resolved entanglement entropies in integrable systems*, arXiv:2203.09158.

[319] A. Peres, *Separability criterion for density matrices*,Phys. Rev. Lett. **77**, 1413 (1996).

[320] J. Eisert and M. B. Plenio, *A comparison of entanglement measures*, J. Mod. Opt. **46**, 145 (1999).

[321] M. Horodecki, P. Horodecki, and R. Horodecki, *Separability of n-particle mixed states: Necessary and sufficient conditions in terms of linear maps*, Phys. Lett. A **283**, 1 (2001).

[322] G. Vidal and R. F. Werner, *Computable measure of entanglement*, Phys. Rev. A **65**, 032314 (2002).

[323] M. B. Plenio, *Logarithmic negativity: A full entanglement monotone that is not convex*, Phys. Rev. Lett. **95**, 090503 (2005).